Spatio-temporal Variability of Black Carbon Emission from Wildfire by Change of Climate and Terrestrial Ecosystem in Africa

博士論文

Spatio-temporal Variability of Black Carbon Emission from Wildfire by Change of Climate and Terrestrial Ecosystem in Africa

（アフリカにおける気候・陸域生態系の変化による火災起源ブラックカーボン放出の時空間変動性）

石井　翔太

平成 25 年

Thesis Adviser
Dr. Takeshi Yamazaki

Author
Shota Ishii

Spatio-temporal Variability of Black Carbon Emission from Wildfire by Change of Climate and Terrestrial Ecosystem in Africa

Abstract

Frequent wildfires emit large amounts of black carbon (BC) into the atmosphere in the semiarid regions of the African continent. This atmospheric BC efficiently absorbs shortwave radiation and thus modifies the climate system on a regional scale. Therefore, it is essential to understand how geographical distribution patterns of BC emissions are controlled by climate and vegetation in these regions. In addition, carbonaceous aerosol emissions from wildfires are controlled by climatic cycles such as the El Niño–Southern Oscillation (ENSO) and the Indian Ocean Dipole, both of which regulate vegetation productivity related to the fuel load available for wildfires. However, the relationship between carbonaceous aerosol emissions and climatic cycles has not been evaluated quantitatively. On the other hand, in the future, Global Climate Model (GCM) simulation studies predicted the increment of air temperature and change of precipitation over the African continent. Other previous studies showed that a vegetation biomass increased with climate change in future. Therefore, amount of BC emission may increase with changes in fuel load and fire frequency due to those changes of climate and biomass. However, future BC emission from wildfire has not been evaluated quantitatively because there are high uncertainty of climate, ecosystem, and fire frequency in the future.

First, we studied factors contributing to the variance of geographical distribution patterns of BC emissions. We applied a principal component analysis (PCA) to the correlations between dry season BC emissions observed by satellite and climate variables during the vegetation growing and dry seasons, and to correlations between BC and the leaf area index during the growing season, as independent values. We analyzed the burned fraction (BF) in the same way, but its factor loadings did not differ significantly from those of BC in sign or magnitude. During the growing season, the response pattern of vegetation productivity (an index of wildfire fuel loading) to climate variables explained 57.5% of the regional variability in BC emissions. This vegetation productivity was more closely correlated with the geographical distribution patterns of BC emission than climate variables such as temperature during the

dry season. The response pattern of vegetation productivity to climate during the vegetation growing season was roughly determined by vegetation parameters such as biome type and tree cover, which are heterogeneously distributed in Africa. Therefore, regional BC emission patterns would differ even if climate change occurred uniformly throughout semi-arid Africa.

Second, we studied carbon emission sensitivity to changes in climate temporal variation. We conducted two sets of experiments using a spatially explicit individual-based dynamic global vegetation model (SEIB-DGVM), which contained a wildfire sub-model. The first set of experiments, referred to as precipitation or temperature no-cycle experiments, was forced by 20 years of climate data with negligible inter-annual variation in annual precipitation or annual mean air temperature. The second set, referred to as precipitation or temperature cycle experiments, was forced by 20 years of climate data showing cyclic inter-annual variability at a frequency of 20, 10, and 6 years for precipitation or air temperature. The control experiment, which used observation-based climatic data from 1982 to 2009, reconstructed a reasonable spatial distribution of the observed carbon emissions from wildfires in Africa. In the no-cycle experiment for precipitation and temperature, carbon emissions in the northern hemisphere decreased by 15.4% and 15.1%, respectively, compared with emissions in the control experiment, whereas there was little difference in the southern hemisphere. In the cycle experiment for precipitation, carbon emissions increased in the northern hemisphere when the cycle of precipitation fluctuation was shorter: the increase ratios are 2.3 %, 3.0 %, and 5.2 % for the frequency of 20, 10, and 6 years, respectively. However, in the cycle experiment for temperature, carbon emissions did not significantly vary with fluctuations in the cycle. The pattern of cyclic changes in precipitation controls vegetation productivity, which relates fuel load for wildfire, and fraction of tree coverage, which relates fire possibility. Therefore, our simulation revealed the importance of the pattern of inter-annual variability in precipitation to regulating carbonaceous aerosol emissions in the African continent.

Finally, we studied a future BC emissions from wildfire following previous chapters. We estimated future BC emission from wildfire using a dynamic global vegetation model with a climate projection provided by the MIROC 3.2 general circulation model, and analyzed the cause of changes in amount and spatial distribution of BC emission. In the African continent (37°S–34°N, 17°W–59°E), the average of annual BC emission increased by 30.5% during the 21st century. Range of the increment of BC emission was higher for northern hemisphere (0°S–15°N, 17°W–41°E) than for southern hemisphere (30°S–0°N, 5°W–41°E) of the African continent: They were, 40.4% and 16.7 %, respectively. In accord with this trend, increment of biomass under future climate is higher for northern hemisphere than for southern

hemisphere: They were 39.8 % and 26.0%, respectively. These corresponding changes in the BC emission and biomass suggest that simulated increment of BC emission is caused by the increment of biomass, which is a result of higher atmospheric CO_2 concentration under future environment. It is also shown that the changes in annual precipitation have intensive impacts on the geographical distribution of the BC emission.

Contents

Abstract i
List of Figure vii
List of Table xi
Acknowledgments xii

1. Introduction 1

1.1 Study Background ---- 1
1.2 Purpose of This Study ---- 4

2. Geographical Variability of Relations among Black Carbon from Wildfires, Climate, and Vegetation in Africa 5

2.1 Introduction ---- 5
2.2 Data and Methods ---- 7
2.2.1 Description of Black Carbon and Burned Fraction ---- 7
2.2.2 Analysis Domain and Period ---- 7
2.2.3 Analysis Variable and Data Processing ---- 9
2.2.4 Principal Component Analysis ---- 12
2.3 Results ---- 15
2.3.1 Contribution Ratios ---- 15
2.3.2 Factor Loadings ---- 15
2.3.3 Principal Component Scores ---- 17
2.4 Discussion ---- 19
2.4.1 Comparison with Black Carbon and Burned Fraction ---- 19
2.4.2 1st Principal Component ---- 19
2.4.3 2nd Principal Component ---- 22

2.5 Summary ---- 25

3. The Relationship between Wildfire Carbon Emissions and Cyclic Variations in Precipitation and Temperature over Africa 6

3.1 Introduction ---- 26
3.2 Methods ---- 28
3.2.1 Overview of the Modified Model ---- 28
3.2.2 Climate Data for Simulation ---- 29
3.2.3 Simulation Procedure ---- 30
3.3 Results ---- 31
3.3.1 Control Experiment ---- 31
3.3.2 Precipitation and Temperature No-cycle Experiments ---- 33
3.3.3 Precipitation and Temperature Cycle Experiments ---- 35
3.4 Discussions ---- 41
3.4.1 Control Experiment ---- 41
3.4.2 Precipitation and Temperature No-cycle Experiments ---- 42
3.4.3 Precipitation and Temperature Cycle Experiments ---- 43
3.5 Summary ---- 46

4. Projection of Future Black Carbon Emission from Wildfire in Africa 48

4.1 Introduction ---- 48
4.2 Methods ---- 51
4.2.1 Overview of the Modified Model ---- 51
4.2.2 Fire Sub-model ---- 51
4.2.3 Soil Moisture Content ---- 51
4.2.4 Stomatal Conductance ---- 52
4.2.5 Climate Data for Simulation ---- 52
4.2.6 Simulation Procedure ---- 54
4.2.7 Conversion from Carbon emission to Black Carbon emission ---- 55
4.3 Results ---- 56
4.3.1 Control Experiment ---- 57
4.3.2 Future Experiment ---- 60
4.3.3 Suppressed CO_2 increment Experiment ---- 64
4.4 Discussions ---- 64

4.4.1 Control Experiment ---- 64
4.4.2 NPP and Biomass of the Future Experiments ---- 65
4.4.3 BC emission of the Future Experiments ---- 67
4.5 Summary ---- 68

5. Conclusions **68**

6. Appendixes **70**

A. Satellite Observation of BC Emission ---- 70
B. Fire Sub-model ---- 71
C. Climate Data for Simulation ---- 74
D. Climate Data for the Cycle Experiments ---- 75
E. Skill Score ---- 78
F. Stomatal Conductance ----79

Bibliography **82**

List of Figures

1.1 Sectoral contributions to emissions of black and organic carbon emissions. The gray bars behind the colored bars represent the fraction of emissions from "contained" combustion (that undertaken for energy use, excluding open burning) in each region. The green bars to the left indicate the relative contribution of each region to the total. The contributions are based on our central values and carry all the caveats outlined in the text. From Bond et al. (2004). ---------- 2

1.2 Emissions of BC and organic carbon aerosol. "Contained" combustion, based on 1996 activity data of BC (a) and organic carbon (c). Open burning, annual average of BC (b) and organic carbon (d). The color coding is an approximately logarithmic scale. Units are ng m^{-2} s^{-1}. From Bond et al. (2004). ---------- 2

1.3 Global distribution of BC sources and radiative forcing (W m^{-2}). Atmospheric solar heating due to BC (left) and surface dimming (right) due to atmospheric brown clouds (right) for the 2001 to 2003 period. This shows the reduction in absorbed solar radiation at the surface by all anthropogenic aerosols (BC and non-BC) in atmospheric brown clouds. This study integrates satellite aerosol data, surface network of aerosol remote sensing instruments and field observations with an aerosol-transport-chemical model and a radiative transfer model to obtain the forcing. From Ramanathan and Carmichael (2008). ---------- 3

1.4 Average continental precipitation recycling ratio (1999–2008). From van der Ent et al. (2010). ---------- 3

2.1 Black carbon (BC) emissions during the dry season in the northern and southern hemispheres averaged over 1997–2008: (a) December to February and (b) July to September. Data are from the Global Fire Emissions Database v. 3 (see Table 1.1). Red squares: large grid cells (3.0° × 3.0°) in the 3 analysis regions. ---------- 9

2.2 Precipitation integrated over the 7 month vegetation growing season in the northern and southern hemispheres, averaged over 1997–2008: (a) April to October and (b) November to May. ---------- 11

2.3 Correlation coefficient (r) between black carbon (BC) and (a) dry season temperature, (b) dry season cloud cover, (c) growing season precipitation, (d) growing season temperature, (e) growing season cloud cover, (f) growing season leaf area index during 1997–2008. DJF: December to February; JAS: July to September. ---------- 13
2.4 Factor loadings on principal components (PCs) 1–3: (a) burned fraction (BF) and (b) black carbon (BC) emission. A large absolute value means that the factor strongly affects BF or BC. The sign of the factor loading corresponds to the sign of the correlation coefficient between BF (or BC) and the respective variable. LAI: leaf area index. ---------- 16
2.5 Principal component (PC) scores in each large grid cell during the dry season obtained in the black carbon (BC) analysis: (a) PC1 and (b) PC2. Positive scores (warm colors) indicate the same tendency as the factor loadings on that PC, and negative scores (cool colors) indicate the opposite tendency to the factor loadings. DJF: December to February; JAS: July to September. ---------- 18
2.6 Correlation coefficients between precipitation and temperature during the growing season during 1997–2008. AO: August to October; NM: November to May. -------- 20
2.7 Correlation coefficients for temperature between the growing and dry seasons during 1997–2008. AO: August to October; DJF: December to February; NM: November to May; JAS: July to September. ---------- 20
2.8 Biome distributions in central Africa. ---------- 21
2.9 Principal component 1 (PC1) scores averaged by biome type. Circles: PC1 score in each grid cell classified into a biome type; bottom and top of each box: lower and upper quartiles, respectively; bold horizontal line in the middle of the box: median value. ---------- 22
2.10 Relationships among the principal component 2 (PC2) scores (color scale), tree cover and leaf area index (LAI). The average for grid cells with scores smaller than −0.2 is shown by a blue X, and the average for grid cells with scores larger than +0.2 is shown by a red X. The standard deviations of tree cover and LAI are respectively shown by the vertical and horizontal gray lines passing through each average. ---------- 24

3.1 Distribution of precipitation and air temperature over the African continent from CRU data during the period of 1982–2009. (a) average and (b) standard deviation of annual precipitation, and (c) average and (d) standard deviation of annual mean temperature. ---------- 29
3.2 Time-averaged annual carbon emissions from fires during the period of 1997–2009

over the African continent: average of 10 simulations for SEIB-DGVM (right) and GFED (left). ---------- 31
3.3 Annual mean tree cover over the African continent: (right) average of 10 simulations using SEIB-DGVM during 1997–2009 and (left) AVHRR Continuous Fields Tree Cover Product (DeFries et al., 2000). ---------- 32
3.4 The percentage of the total number of grid cells of each tree cover segment (0–10, 10–25, 25–40, 40–65, and 65–100%) in the northern hemisphere and the southern hemisphere. Green: SEIB-DGVM, orange: VHRR Continuous Fields Tree Cover Product. ---------- 33
3.5 The spatial distribution pattern of the difference in annual carbon emission between no-cycle experiments and control experiments (no-cycle − control): (a) precipitation no-cycle experiments and (b) temperature no-cycle experiments. This annual carbon emission is the average value of 10 simulations over 20 years. ---------- 34
3.6 The dependence of the differences in the percentage tree cover on the TC segment and the change in carbon emissions on the TC segment. Bars indicate changes in tree cover (no cycle − control) on the left ordinate. Cross marks indicate changes in carbon emission on the right ordinate (no cycle − control). Blue: precipitation experiment, red: temperature experiment. The abscissa is the TC segment (0–10, 10–25, 25–40, 40–65, and 65–100%). For carbon emissions, the TC segment was defined by the control experiment. ---------- 35
3.7 The rate of change in carbon emissions in each cycle experiment compared with the no-cycle experiment. Blue: precipitation experiment, red: temperature experiment. The abscissa is the cycle of annual precipitation fluctuation or annual mean temperature fluctuation. The triangle / inverted triangle indicates the carbon emission of the phase (+) / (−) cycle experiment. In phase (+) / (−), annual precipitation and annual mean temperature increase / decrease in the first half of the cycle, and those variables then decrease / increase in the second half of the cycle. The black bar is the standard deviation across 10 simulations. The cross (X) is the average value of phase (+) and phase (−). ---------- 36
3.8 The differences in percentage tree cover in grid cells in each hemisphere between no-cycle experiments and control experiments (cycle – no-control). (a) 20-year cycle experiment, (b) 10-year cycle experiment, and (c) 6-year cycle experiment. The value is the average of phase (+) and phase (−) cycle experiments. Blue: precipitation cycle experiment, red: temperature cycle experiment. The abscissa is the segment of TC (0–10, 10–25, 25–40, 40–65, and 65–100%). ---------- 38
3.9 The phase-averaged difference in tree cover between the 6-year cycle experiment

and the no-cycle experiment (6-year cycle – no-cycle). (a) precipitation experiment and (b) temperature experiment. ---------- 39
3.10 The differences in carbon emissions between cycle experiments and no-cycle experiments in each TC segment defined by no-cycle experiments. (a) 20-year cycle experiment, (b) 10-year cycle experiment, and (c) 6-year cycle experiment. The abscissa is the segment of TC (0–10, 10–25, 25–40, 40–65, and 65–100%). Blue: precipitation cycle-experiment, red: temperature cycle-experiment. ------- 40
3.11 The phase-averaged difference in biomass between the 6-year precipitation cycle experiment and precipitation no-cycle experiment (6-year cycle – no-cycle). ---- 44

4.1 (a) Annual precipitation and (c) annual mean surface temparature during 2001-2010, and the changes of (b) annual precipitation and (d) annual mean surface temperature during 2001-2010 to 2081-2100. ---------- 54
4.2 Time averaged of annual BC emission from wildfire during 2001-2010: (right) 10 simulations average of SEIB-DGVM and (left) GFED. ---------- 56
4.3 Time averaged of fire intervals for each virtual forest during 2001-2010. ------- 57
4.4 Change of annual BC emission of wildfire during 2001-2010 to 2081-2100. The region where there was a characteristic change of BC emission is surrounded with a dotted line. ---------- 58
4.5 The difference of (a) biomass, (b) NPP, and (c) tree cover between 2081-2100 and 2001-2010 years. The change ratio of (d) fire frequency during 2081-2100 to 2001-2010. ---------- 59
4.6 Change of annual BC emission during 2001-2010 to 2081-2100 in the suppressed CO_2 increment experiment. The region where there was a characteristic change of BC emission is surrounded with a dotted line. ---------- 61
4.7 Same as Fig. 4.5 but by the suppressed CO_2 increment experiment. ---------- 62
4.8 Annual BC emission from wildfire. Gray: present (2001-2010), vermilion: future (2081-2100) and blue: future by suppressed CO_2 increment experiment. All indicate the African continent. ---------- 63

List of Table

2.1 Datasets used for analysis. LAI: leaf area index; BC: black carbon; BF: burned fraction ---------- 7

4.1 Table 1. Changes in BC, biomass, NPP, tree cover, and fire frequency of each region in the future experiment during the 21st century. Numbers for regions refer to the Fig. 4.4. ---------- 63

4.2 Table 2. Changes in BC, biomass, NPP, tree cover, and fire frequency of each region in the future experiment during the 21st century under suppressed CO_2 increment. Numbers for regions refer to the Fig. 4.6. ---------- 63

Acknowledgments

I would like to express my sincere thanks to Dr. Takeshi Yamazaki for his thoughtful guidance and encouragements. I learned from him how to tackle research issues through daily stimulating discussion.

The spatially explicit individual-based dynamic global vegetation model (SEIB-DGVM) used in this thesis has been developed by Dr. Hisashi Sato. His advice and encouragements were critical to the improvement of our paper. Without him, I could not get Ph. D.

Of course, encouragements from other members in the Atmospheric Science Laboratory were essential to my Ph.D. thesis. Prof. Toshiki Iwasaki, Dr. Weiming Sha, Dr. Masahiro Sawada, Dr. Ryuhei Yoshida, Dr. Guixing Chen, and many students advised me in seminar, lectures, rindoku (reading by turns), etc.

Dr. Shinjiro Fujii, Dr. Hiroshi Hayasaka, Dr. Kazuhito Ichii, Dr. Ayumi Kotani, Dr. Takahiro Sasai, Dr. Kengo Sudo, and Mr. Masayuki Kondo provided me many pieces of valuable advice on may research and let me know information on some conferences.

My Ph.D. work was financially supported by the Tohoku University Global Center of Excellence program 'Global Education and Research Center for Earth and Planetary Dynamics' (research assistant, travel grant, etc.), Tohoku Kaihatsu Memorial Foundation (travel grant). Part of this research was carried out using supercomputing resources at Cyberscience Center, Tohoku University.

Chapter 1

Introduction

1.1 Study Background

In semi-arid regions of Africa, wildfires occur frequently during the dry season and have a large effect on the structure, dynamics, and distribution of vegetation (Higgins et al. 2000, 2007; Sankaran et al. 2004, 2005; Bond et al. 2005a). Wildfires also emit large amounts of carbon aerosols (e.g., black carbon (BC) and organic carbon (OC)) (Bond et al., 2004). The percentage of BC emissions from wildfire to total BC emissions in the African continent was 75% (Fig. 1.1) and savanna burning in Africa contributes the greatest amount to BC for biomass burning (Fig 1.2). Atmospheric BC and OC have ability to change climatic system by absorbing or scattering shortwave radiation and thereby decreasing downward shortwave radiation on the land surface (Ramanathan and Carmichael 2008; Bond et al. 2011) (Fig. 1.3). Kawase et al. (2011) reported that the reduction in net radiation and evapotranspiration at the land surface due to atmospheric BC caused a decreasing trend of precipitation in tropical Africa during the 20th century. Any decrease or increase in atmospheric BC is likely to have a significant impact on precipitation over Africa because the African continent is characterized by a high recycling ratio, i.e., the ratio of regional precipitation supplied by evapotranspiration from the land surface that falls as local precipitation to the total precipitation. Van der Ent et al. (2010) estimated this ratio to be 0.49 for a rectangular region (37°S–34°N, 17°W–59°E) surrounding the African continent (Fig. 1.4).

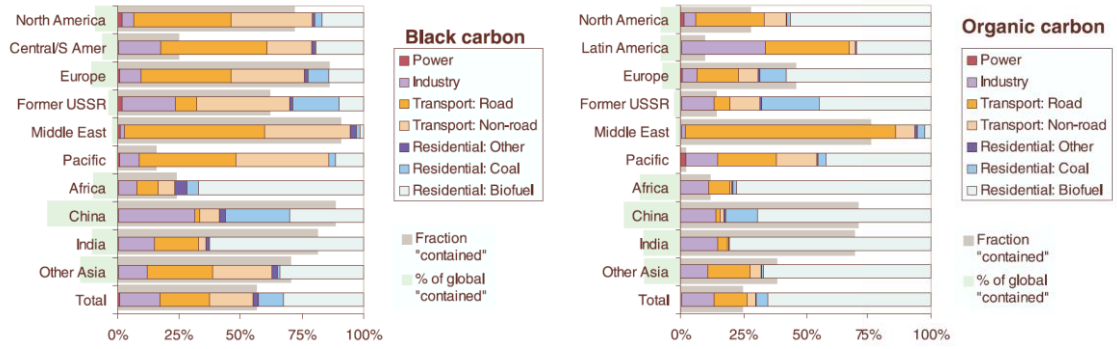

Fig. 1.1. Sectoral contributions to emissions of black and organic carbon emissions. The gray bars behind the colored bars represent the fraction of emissions from "contained" combustion (that undertaken for energy use, excluding open burning) in each region. The green bars to the left indicate the relative contribution of each region to the total. From Bond et al. (2004).

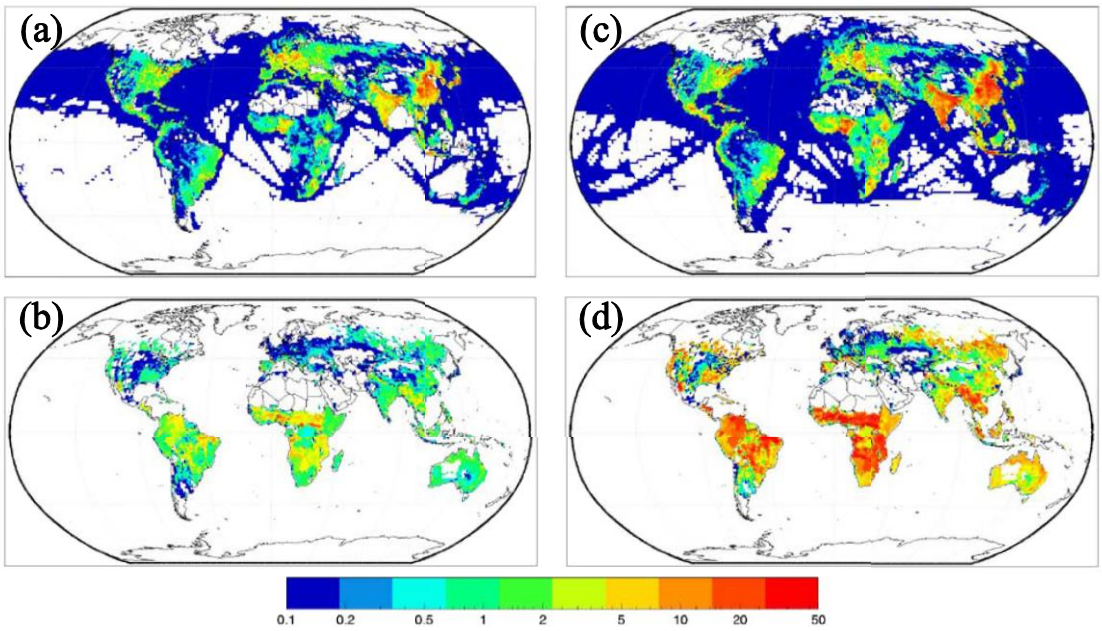

Fig. 1.2. Emissions of BC and organic carbon aerosol. "Contained" combustion, based on 1996 activity data of (a) BC and (c) organic carbon. Open burning, annual average of (b) BC and (d) organic carbon. The color coding is an approximately logarithmic scale. Units are ng m^{-2} s^{-1}. From Bond et al. (2004).

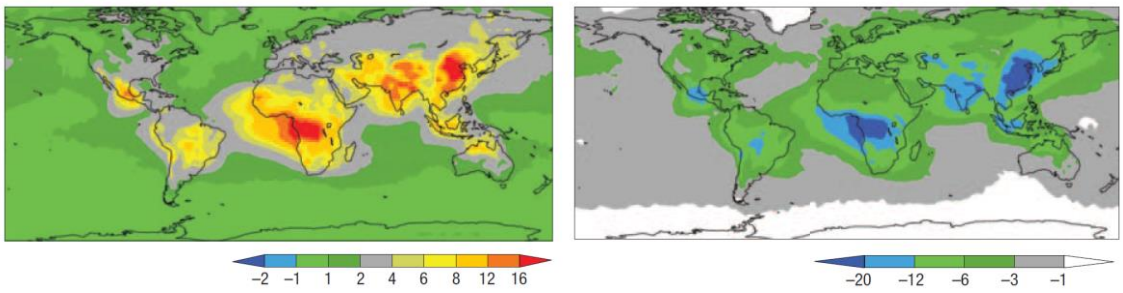

Fig. 1.3. Global distribution of BC sources and radiative forcing (W m^{-2}). Atmospheric solar heating due to BC (left) and surface dimming (right) due to atmospheric brown clouds (right) for the 2001 to 2003 period. This shows the reduction in absorbed solar radiation at the surface by all anthropogenic aerosols (BC and non-BC) in atmospheric brown clouds. This study integrates satellite aerosol data, surface network of aerosol remote sensing instruments and field observations with an aerosol-transport-chemical model and a radiative transfer model to obtain the forcing. From Ramanathan and Carmichael (2008).

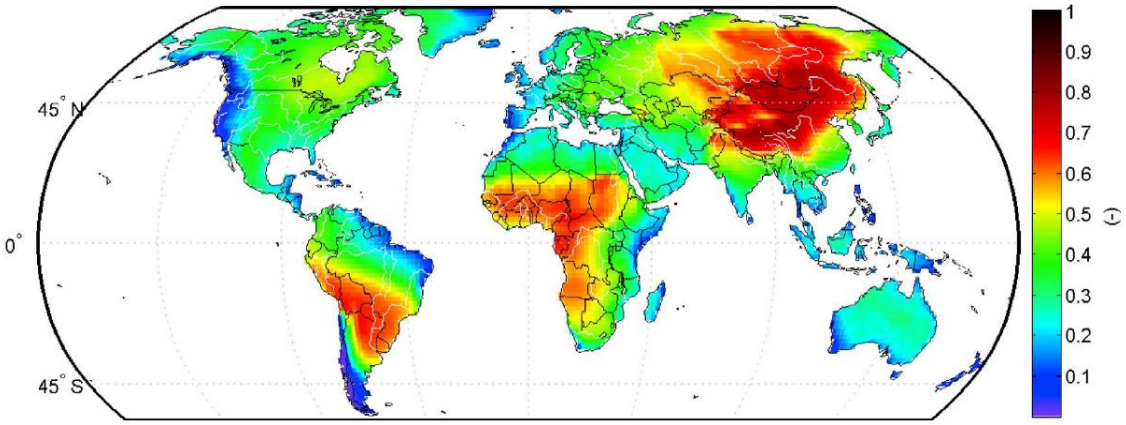

Fig. 1.4. Average continental precipitation recycling ratio (1999–2008). From van der Ent et al. (2010).

1.2 Purpose of This Study

The purpose of this study is to understand the characteristic of spatiotemporal variability of BC emission from wildfire in the African continent. First, we estimated the factors that influence the occurrence of wildfires and the BC emission geographical distribution pattern by comparing the geographical distribution of the factors estimated from previous work and the analyzed principal component scores. Second, we quantitatively evaluated the effect of the periodic inter-annual variability in annual precipitation and annual mean temperature on carbon emissions from wildfires over the African continent by use of the spatially explicit individual-based dynamic global vegetation model (SEIB-DGVM). Finally, we estimated BC emission from wildfire in the future with SEIB-DGVM and future climate data, and then analyzed the cause of changes in spatial distribution of BC emission in the African continent.

Chapter 2

Geographical Variability of Relations among Black Carbon from Wildfires, Climate, and Vegetation in Africa

2.1 Introduction

Any decrease or increase in atmospheric BC is likely to have a significant impact on precipitation over the African continent. Because vegetation productivity determines the fuel production rate (Lehsten et al. 2009), an investigation of the relationships among fire, climate and vegetation abundance is necessary to understand climate system dynamics in Africa.

The geographical pattern of wildfire frequency and intensity is primarily determined by climate, fuel loading and the moisture content of the fuel (Cooke et al. 1996, Bowman et al. 2009). The pattern is also affected by the vegetation type (Dwyer et al. 2000), lightning frequency, human population density (Keeley et al. 1999), land use (Russell-Smith et al. 2007) and tree cover (Archibald et al. 2009). However, the integration of these factors to generate the observed geographical pattern of wildfires has yet to be adequately evaluated quantitatively.

Remote sensing studies of the Sahel have suggested that inter-annual perturbations in indices of vegetation greenness such as the normalized difference vegetation index

(NDVI) and the leaf area index (LAI) are primarily controlled by precipitation (Anyamba and Tucker 2005, Hickler et al. 2005). On the African continent generally, field studies suggest that precipitation is the primary determinant of plant species composition and plant production (Gonzalez 2001, MacGregor and O'Connor 2002, Lwanga 2003). Besides precipitation, air temperature and solar radiation intensity also affect vegetation productivity (Allen et al. 2010).

The aim of this study was to estimate the factors that influence the occurrence of wildfires and the geographical distribution pattern of BC emissions (e.g. vegetation type, lightning frequency, human population density, land use and tree cover) in semiarid Africa. However, we were unable to directly analyze the correlations between the BC emission and these factors because there are no long-term time series data for, e.g. vegetation type and tree cover. Thus, the significant differences in the geographical distribution pattern of the 6 correlation coefficients, namely BC−precipitation (growing season), BC−temperature (growing, dry season), BC−cloud cover (growing, dry season) and BC−LAI (growing season) (i.e. variations in the 6 correlation coefficients across semi-arid Africa), were estimated by performing a principal component analysis (PCA). Meaningful comparisons of the geographical distribution patterns were analyzed using the variations in these 6 correlation coefficients across semi-arid Africa (i.e. the principal component scores). Finally, the factors that influence the occurrence of wildfires and the BC emission geographical distribution pattern were estimated by comparing the geographical distribution of the factors estimated from previous work and the analyzed principal component (PC) scores in this study.

In Section 2.2, the study area and spatial resolution are defined, and the procedures for calculating the BC–climate and BC–vegetation parameter correlation coefficients and the PCA are described. In Section 2.3, each PC contribution ratio and the significant differences in the geographical distribution pattern of the BC–climate and BC–vegetation parameter correlations are comprehensively estimated. Then, the geographical distribution patterns are analysed using a variation of those correlation coefficients across semi-arid Africa using the PC scores. In Section 2.4, the factors that influence the BC emission geographical distribution pattern are estimated.

2.2 Data and Outline of the Method

2.2.1 Description of Black Carbon and Burned Fraction

We used existing data sets for our analysis (Table 2.1). We converted the spatial resolution of the LAI and tree cover data to a 0.5° × 0.5° grid resolution to match the resolution of the other datasets by simple averaging over each grid cell domain.

Table 2.1. Datasets used for analysis.

LAI: leaf area index; BC: black carbon; BF: burned fraction

Variable	Data product	Data period	Product resolution	Time interval	Reference
Temperature, precipitation, cloud cover	Climatic Research Unit (CRU) TS3.1	1997–2008	0.5° × 0.5°	Month	Mitchell & Jones (2005)
LAI	MODIS	2001–2008	0.25° × 0.25°	Month	MOD15A2 (Land Processes Distributed Active Archive Center, http://lpdaac.usgs.gov)
BC, BF	Global Fire Emissions Database version 3	1997–2008	0.5° × 0.5°	Month	Giglio et al. (2010)
Biome	The International Satellite Land Surface Climatology Project (ISLSCP) Initiative II Data Collection	–	0.5° × 0.5°	–	Turner et al. (2006)
Tree cover	AVHRR Continuous Fields Tree Cover Product	–	1/60° (= 1 min)	–	DeFries et al. (2000)

The BC is related to the burned fraction (BF) which was calculated by dividing the yearly burned area in a grid cell by the total area of that grid cell and to incomplete fuel combustion (Schmidt et al. 2001). The fire fuel comprises the hot volatile vapor-phase products of the thermal decomposition of vegetation. These vapors and their cracking products undergo flaming combustion. However, in competition with this, they can also undergo condensation and charring to powdery soot particles. These soot particles may combust or be swept into the air away from the fire to become aerosol BC. Thus, the distribution of hot volatiles between flaming combustion and thermo-condensation, and between aromatization and soot formation, determines the incomplete combustion ratio, which is a different quantity from the BF. Therefore, the determinants of BC are more complicated than those of BF.

2.2.2 Analysis Domain and Period

As the study area, we selected part of sub-Saharan Africa (3°N–12°N, 12°W–34°E and

15°S–5°S, 24°W–39°E) where a large amount of BC is emitted every year. In this study, we define the dry season, which corresponds to the fire season in Africa (Dwyer et al. 2000), as the months of December to February (DJF) in the northern hemisphere and July to September (JAS) in the southern hemisphere. We define the growing season as the months of April to October in the northern hemisphere and the months of November to May in the southern hemisphere. We excluded from our analysis data for March and November (northern hemisphere) and those for June and October (southern hemisphere), because in those months the distinction between the growing and dry seasons is unclear. The growing season was defined so as to have no overlap with the dry season, and to include the month in which the LAI reached its maximum value in that hemisphere.

We divided our study area into 40 large (3.0° × 3.0°) grid cells (Fig. 2.1). Each large grid cell was composed of 36 small (0.5° × 0.5°) grid cells. A large grid cell was included in the analysis if more than half of the contained small grid cells had mean BC emissions (averaged over the years 1997–2008; Fig. 2.1) 0.05 g C m^{-2} during the dry season in the region in which the large grid cell was located. The selected grid cells clustered in 3 regions, which are referred to as Regions 1–3 hereafter (Fig. 2.1).

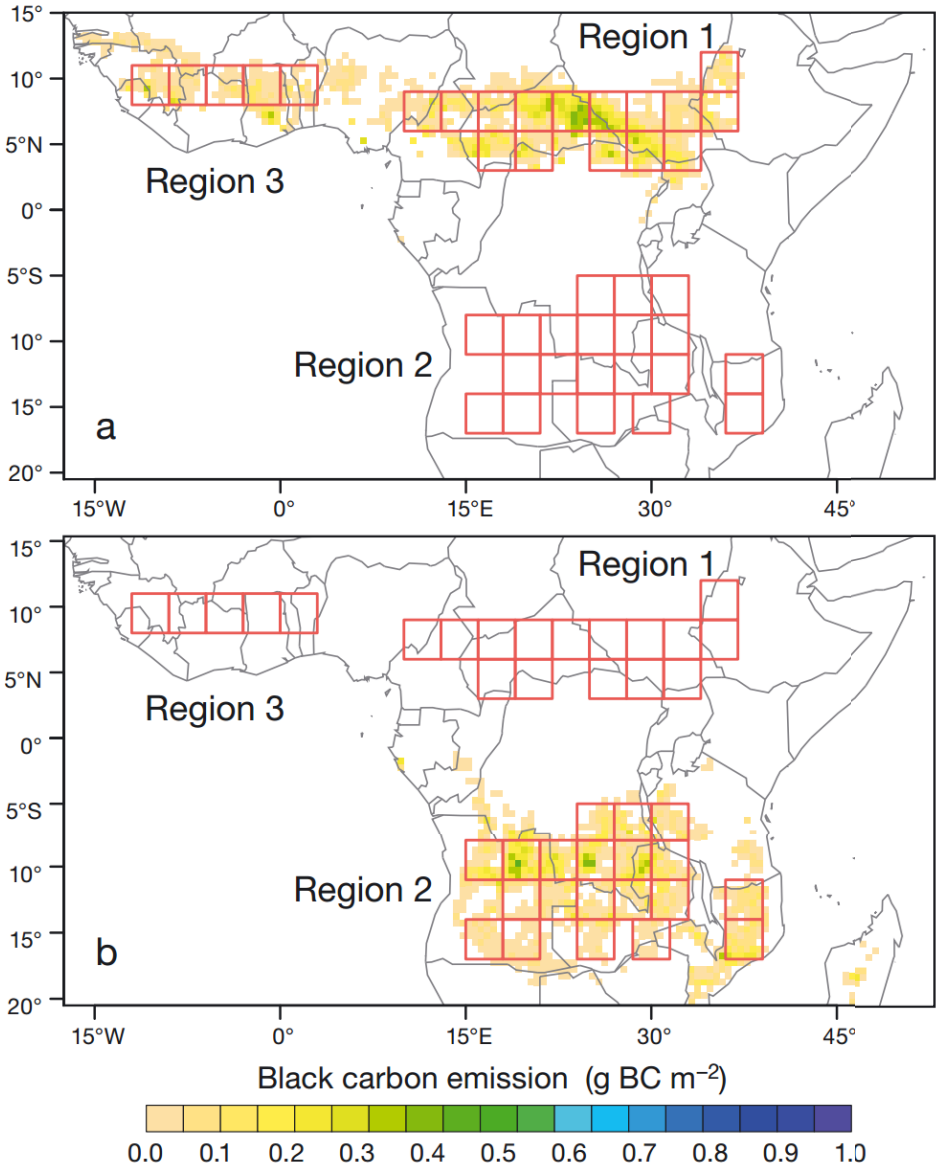

Fig. 2.1. Black carbon (BC) emissions during the dry season in the northern and southern hemispheres averaged over 1997–2008: (a) December to February and (b) July to September. Data are from the Global Fire Emissions Database v. 3 (see Table 2.1). Red squares: large grid cells (3.0° × 3.0°) in the 3 analysis regions.

2.2.3 Analysis Variable and Data Processing

We analyzed the effect of climate variables during both the growing and dry seasons, and the effect of LAI during the growing season on BC emissions during the dry season and BF. First, we averaged the BC, BF, air temperature and cloud cover during the dry season for each year and each large grid cell. We did not average precipitation during the dry season because its quantity was negligible. We used the normalized probability

density of annual BC emissions in the large grid cells to calculate the correlation coefficients between BC and each climate variable. Wildfire consumes its fuel load, and thus it rarely occurs every year in the same small grid cell (0.5° × 0.5°). As a result, the probability density of annual BC emissions in a single grid cell is unlikely to have a normal distribution. The distribution of the probability density of annual BC emissions averaged in each large grid cell (3.0° × 3.0°), however, is likely to be closer to a normal distribution. If an even larger grid size were employed, the probability density distributions of BC would become even closer to a normal distribution, but the heterogeneity of climate variables within a grid cell would be obscured. Therefore, we used trial and error to determine that a grid size of 3.0° × 3.0° gave the best balance in this trade-off.

We similarly averaged the climate variables, i.e. precipitation (Fig. 2.2), temperature and cloud cover, along with the LAI over the growing season of each year in each large grid cell. We did not average the BC emissions and BF during the growing season, when wildfires rarely occurred.

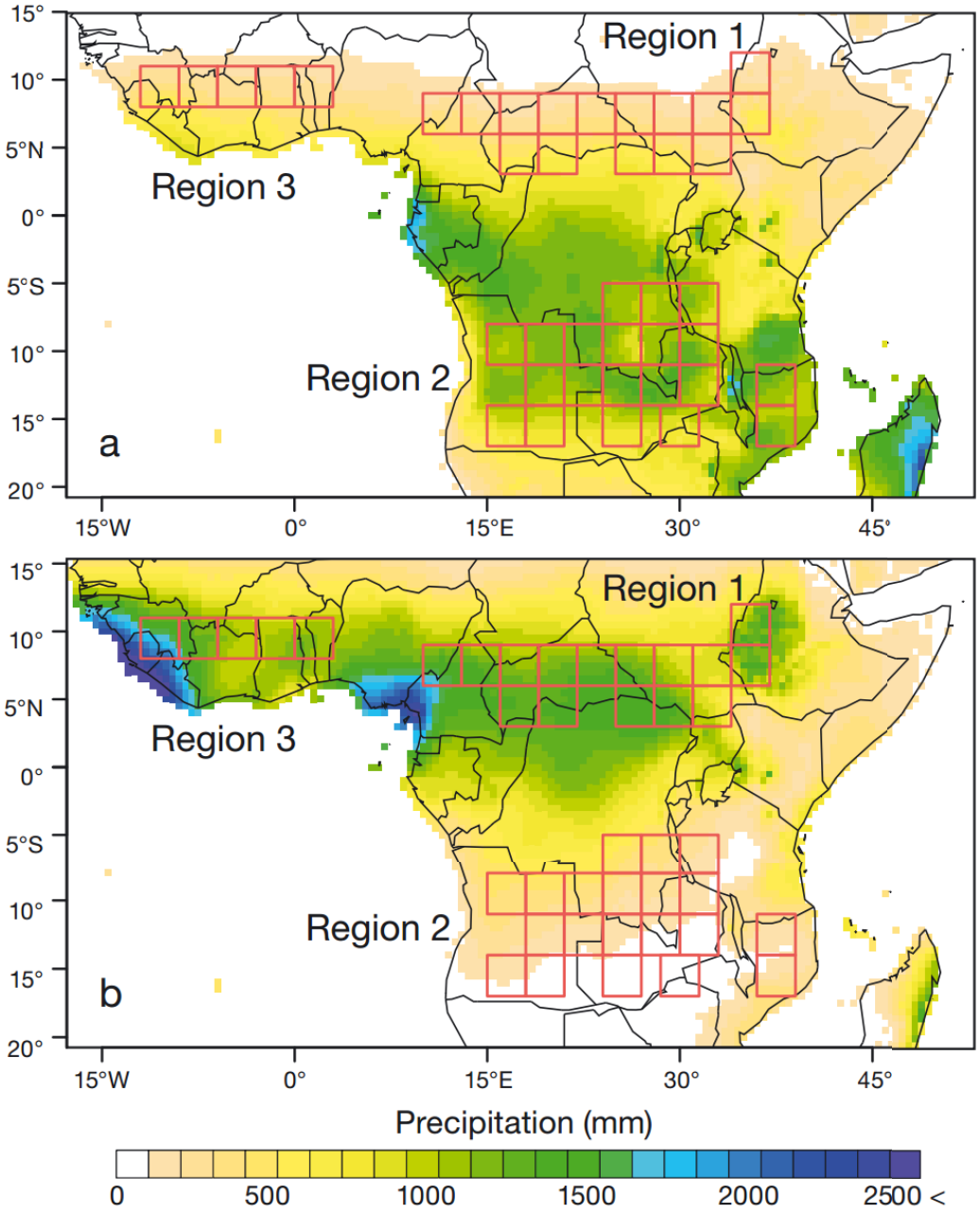

Fig. 2.2. Precipitation integrated over the 7 month vegetation growing season in the northern and southern hemispheres, averaged over 1997–2008: (a) April to October and (b) November to May.

Normally distributed variables can be represented by their normalized deviations, which allow comparisons to be performed among regions. We calculated the normalized deviation of variable A (A') as follows:

$$A'_j = \frac{A_j - \bar{A}_j}{\sigma_j}, \tag{2.1}$$

where A_j, $\bar{A}_j$, and σ_j show the values for both the dry and growing season variable A in grid cell j, the value of A_j averaged over the analysis period and the standard deviation of A_j, respectively; $j = 1, 2 \ldots n$, where n is the total number of large grid cells in each region. We used Eq. (2.1) to obtain the normalized deviations of air temperature and cloud cover data during the dry and growing seasons, precipitation and LAI during the growing season only, and BC and BF during the dry season only.

2.2.4 Principal Component Analysis

We used the normalized deviations of the variables to calculate the correlation coefficients between BC and climate variables during the dry season (i.e. temperature and cloud cover), and between BC and climate variables during the growing season (i.e. precipitation, temperature, cloud cover and LAI). In the same way, we also calculated the correlation coefficients between BF and the climate variables during each season. We then used these correlation coefficients to perform PCA, which is a technique for extracting informative orthogonal linear combinations of variables. By this analysis, we extracted 'fire factors' that expressed the geographical distribution pattern of BF in relation to precipitation, temperature, cloud cover and LAI, and other factors that expressed the geographical distribution pattern of BC emissions in relation to those variables. We then compared the BF and BC results.

For the PCA, we used data sets composed of the independent variables X_{j1} to X_{j6} in each large grid cell j, where X is the correlation coefficient between BC emissions (or BF) during the dry season and 1 of 6 variables (LAI [growing], precipitation [growing], temperature [growing], temperature [dry], cloud cover [growing], cloud cover [dry]) (Fig. 2.3).

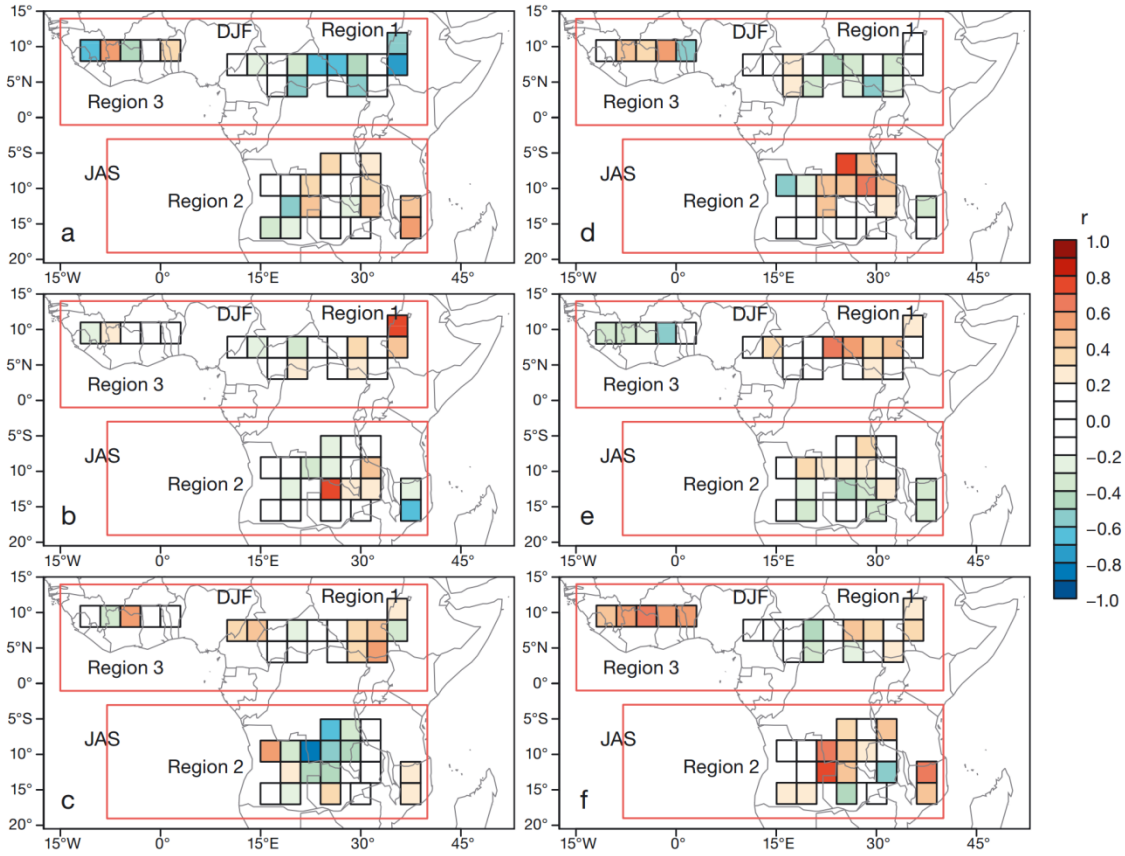

Fig. 2.3. Correlation coefficient (r) between black carbon (BC) and (a) dry season temperature, (b) dry season cloud cover, (c) growing season precipitation, (d) growing season temperature, (e) growing season cloud cover, (f) growing season leaf area index during 1997–2008. DJF: December to February; JAS: July to September.

The data matrix $\boldsymbol{X}$ was 40×6 in size. The sample size (i.e. the number of grid cells) was 40, and the number of independent variables (i.e. the correlation coefficient) was 6. In this way, we converted this multidimensional data set to low-dimensional factors with the least information loss. The p-dimensional data set $\boldsymbol{X_{jp}}$ could be reduced to k dimensions ($k \leq p$) by linear combination with

$$Z_{jk} = \sum_{p=1}^{6} W_{pk} X_{jp} , \tag{2.2}$$

where $\boldsymbol{W_{pk}}$ is a coefficient matrix (i.e. for the kth PC). In PCA, the linear combination of variables that explains the maximum variance of a multidimensional data set is called the first PC (PC1); the second PC (PC2) is the linear combination of the variables

oriented orthogonally to PC1 that explains the maximum residual variance. This procedure solves the equations $(\boldsymbol{V}-\lambda_k \boldsymbol{I})\boldsymbol{w_k}=0$ for λ_k (eigenvalues) and $\boldsymbol{w_k}$, where $\boldsymbol{V}$ is the covariance matrix for $\boldsymbol{X_{jp}}$ and $\boldsymbol{w_k}$ is the vector of coefficients on the kth PC for each variable. $\boldsymbol{I}$ is the unit matrix. The cross-covariance matrix ($\boldsymbol{V}$) of the correlation coefficient matrix of each region $\boldsymbol{X_{jp}}$ (the independent variable, i.e. the correlation coefficient, p = 1~6 in each grid cell j = 1~40) can be calculated as follows:

$$V=\begin{bmatrix} \frac{\sum_{j=1}^{40}(X_{j1}-\overline{X_1})^2}{40} & \frac{\sum_{j=1}^{40}(X_{j1}-\overline{X_1})(X_{j2}-\overline{X_2})}{40} & \cdots & \frac{\sum_{j=1}^{40}(X_{j1}-\overline{X_1})(X_{j6}-\overline{X_6})}{40} \\ \frac{\sum_{j=1}^{40}(X_{j2}-\overline{X_2})(X_{j1}-\overline{X_1})}{40} & \frac{\sum_{j=1}^{40}(X_{j2}-\overline{X_2})^2}{40} & & \vdots \\ \vdots & \vdots & \ddots & \vdots \\ \frac{\sum_{j=1}^{40}(X_{j6}-\overline{X_6})(X_{j1}-\overline{X_1})}{40} & \frac{\sum_{j=1}^{40}(X_{j6}-\overline{X_6})(X_{j2}-\overline{X_2})}{40} & \cdots & \frac{\sum_{j=1}^{40}(X_{j6}-\overline{X_6})^2}{40} \end{bmatrix}, \quad (2.3)$$

where $\overline{X_p}$ is the area-averaged value of X_p for all the grid cells. Eigenvalues λ_k are derived to diagonalise this cross-covariance matrix (i.e. $\boldsymbol{w_k}^T\boldsymbol{V}\boldsymbol{w_k}$, where $\boldsymbol{w_k}^T$ is transposed matrix of $\boldsymbol{w_k}$.). λ_k represents the variance explained by the kth PC, and its contribution ratio C_k is calculated as:

$$C_k=\frac{\lambda_k}{\lambda_1+\lambda_2+\lambda_3\cdots+\lambda_6}=\frac{\lambda_k}{\sum_{m=1}^{6}\lambda_m}, \quad (2.4)$$

where the total number for the kth PC is 6. The cumulative contribution of the k PC is defined as the integrated contribution from PC1 to the kth PC. Z_{jk} is the score of the kth PC, which is calculated using Eq. (2.2). This score is an expression of the spatial variations of the correlations between BC (or BF) and the climate variables, or between BC (or BF) and LAI.

2.3 Results

2.3.1 Contribution Ratios

The contribution ratios of PC1 to PC3 were 41.5, 18.7 and 13.6%, respectively, in the BF analysis, and 39.5, 18.0 and 14.1%, respectively, in the BC analysis. The cumulative contribution of PC1 to PC3 was 73.8% for BF and 71.6% for BC. Therefore, the first 3 PCs explained >70% of the observed variations of the correlations between BC (or BF) and the climate variables, or between BC (or BF) and LAI.

The correlation coefficient between a PC and each independent variable (i.e. X_{j1-6}) (Fig. 2.4), which is referred to as the factor loading on that PC, can help in the interpretation of each PC. We obtained similar factor loading patterns for both BF (Fig. 2.4a) and BC emissions (Fig. 2.4b). Here we focus on the BC results.

2.3.2 Factor Loadings

PC1 represents the most prominent geographical distribution variation pattern. The 3 factor loadings on PC1 with the largest absolute values were BC–temperature (growing) (0.52), BC–temperature (dry) (0.57), and BC–precipitation (growing) (−0.48). These factor loadings indicated that the BC–temperature (growing and dry) and BC–precipitation (growing) correlation coefficients differed considerably in sign and magnitude among large grid cells (Fig. 2.3a, c, d). Therefore, PC1 reflects a large-grid-cell-specific response of BC emissions to variations in temperature during the growing and dry seasons and precipitation during the growing season.

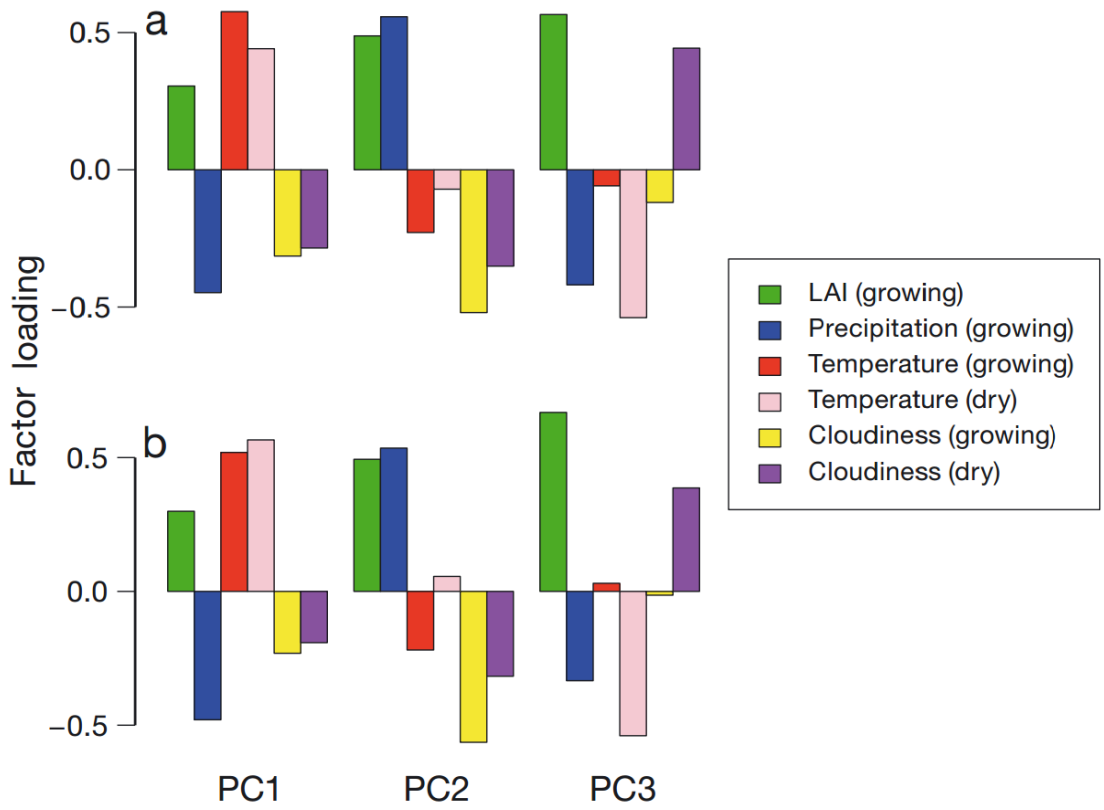

Fig. 2.4. Factor loadings on principal components (PCs) 1–3: (a) burned fraction (BF) and (b) black carbon (BC) emission. A large absolute value means that the factor strongly affects BF or BC. The sign of the factor loading corresponds to the sign of the correlation coefficient between BF (or BC) and the respective variable. LAI: leaf area index.

The 3 factor loadings on PC2 with the largest absolute values were BC–LAI (growing) (0.49), BC– precipitation (growing) (0.54) and BC–cloud cover (growing) (−0.56). These factor loadings showed that the correlation coefficients BC–precipitation (growing), BC–LAI (growing) and BC–cloud cover (growing) differed slightly in sign or magnitude among large grid cells (Fig. 2.3c, e, f). Therefore, PC2 reflects a large-grid-cell-specific response of BC emissions to variations in precipitation, cloud cover and LAI during the growing season.

The factor loadings on PC3 with the 3 largest absolute values were BC–LAI (growing) (0.67), BC–temperature (dry) (−0.54) and BC–cloud cover (dry) (0.39). These factor loadings showed that the correlation coefficients for BC–LAI (growing), BC–cloud cover (dry) and BC–temperature (dry) differed slightly in sign or magnitude among large grid cells (Fig. 2.3a, b, f). Therefore, PC3 reflects a large-grid-cell specific response of BC

emissions to variations in temperature and cloud cover during the dry season and LAI in the growing season.

2.3.3 Principal Component Scores

The PCs were normalized to unit variance. The spatial variations of the correlations between BC and the climate variables, or between BC and LAI, across the grid cells of PC2 and PC3 were small compared with those of PC1 because these variations became small in turn compared with PC1. There was a pattern of opposite correlations between BC and climate among the grid cells with different signs and large scores. The PC2 and PC3 scores can be interpreted in the same way. However, the geographical patterns of contrary correlations of BC with climate or the plant parameters of PC2 and PC3 were smaller than those of PC1. It is difficult to make meaningful comparisons with the patterns of variation in the geographical distribution of the correlation coefficients across the grid cells of PC3 because the characteristic geographical distribution pattern of the PC3 score is unclear. Therefore, we focused on PC1 and PC2.

The average PC1 score in Region 1 was −0.43, which indicates that the BC emission rate increased as temperature decreased and precipitation increased. In Regions 2 and 3, the average PC1 scores were 0.26 and 0.27, respectively, indicating that the BC emission rate increased with temperature and decreased with precipitation (Fig. 2.5a).

The average PC2 score in Region 3 was 0.36, indicating that the BC emission rate increased slightly with precipitation and LAI, and decreased with cloud cover. In contrast, in part of Region 1 (9°N−3°N, 16°E−25°E), the average PC2 score was −0.47, and it was −0.16 in part of Region 2 (8°S−15°S, 15°E−33°E). These scores indicate that the BC emission rate increased slightly as the precipitation and LAI de creased, and increased with cloud cover in these areas (Fig. 2.5b).

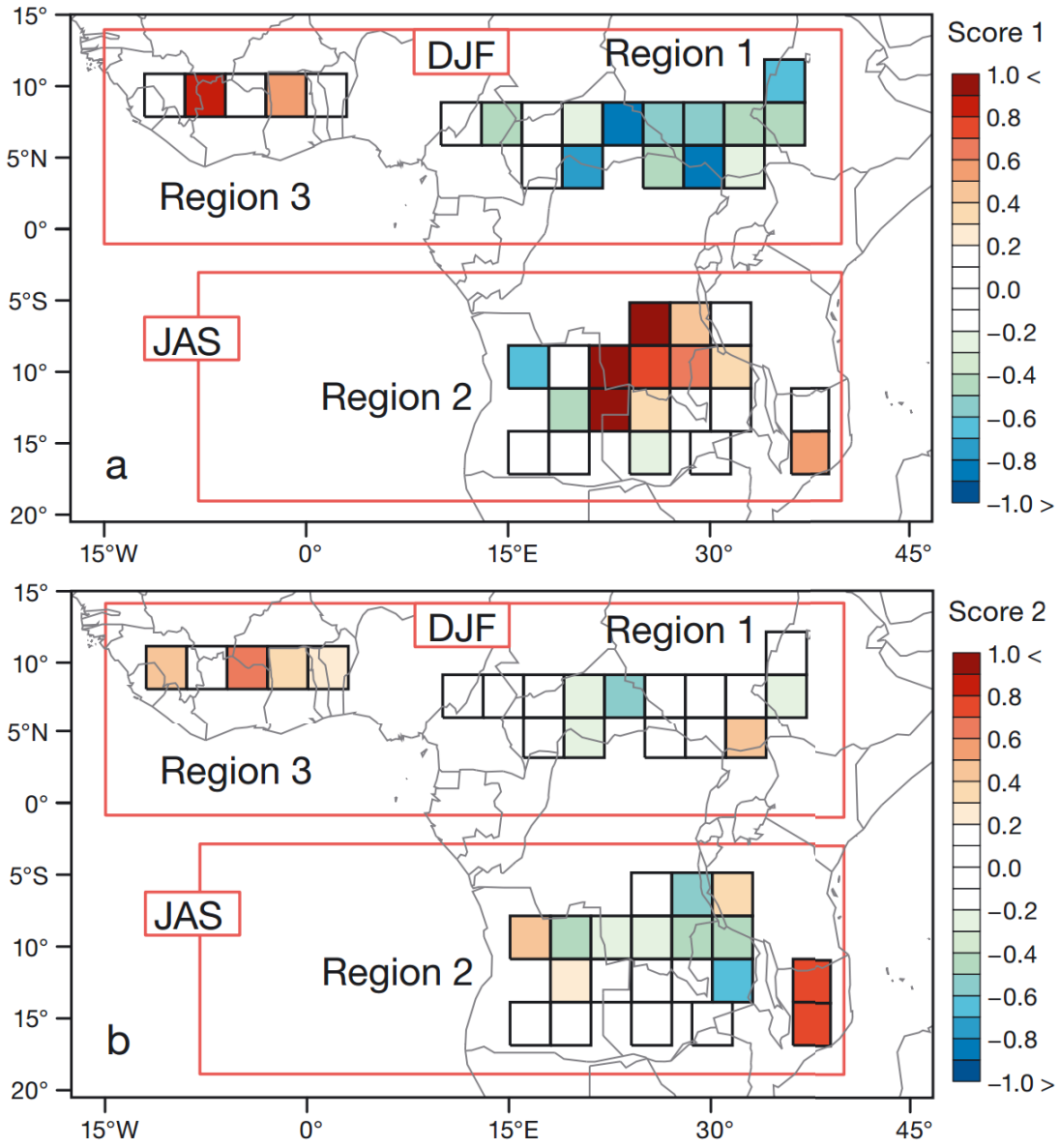

Fig. 2.5. Principal component (PC) scores in each large grid cell during the dry season obtained in the black carbon (BC) analysis: (a) PC1 and (b) PC2. Positive scores (warm colors) indicate the same tendency as the factor loadings on that PC, and negative scores (cool colors) indicate the opposite tendency to the factor loadings. DJF: December to February; JAS: July to September.

2.4 Discussion

2.4.1 Comparison with Black Carbon and Burned Fraction

The factor loadings on each PC and the PC scores were similar for BC emission and the BF (Fig. 2.4). In the Global Fire Emission Database (Table 1), BC emissions were estimated from 3 variables: the BC emission factor, the burned area and the dry matter mass (see the Appendix). The burned area and dry matter mass changed with time, but the BC emission factor did not. The inter-annual differences in BC emission should depend strongly on the burned area and the available dry matter mass. The BF is calculated from the burned area, so it is not surprising that in our results, the geographical distribution patterns were similar between BC emissions (i.e. the factor loadings and the PC scores) and the BF.

2.4.2 1st Principal Component

Higher vegetation productivity would result in a larger fuel load and a larger burned area, and hence more BC emission. However, temperature and precipitation during the growing season were negatively correlated in most large grid cells (Fig. 2.6). This means that the BC–precipitation and BC–temperature correlation coefficients had opposite signs in each large grid cell (Fig. 2.3c, d). Therefore, the factor loadings of BC–temperature (growing and dry) and BC–precipitation (growing) on PC1 had opposite signs. The correlation coefficient between growing and dry-season temperature was positive in nearly all large grid cells (Fig. 2.7) because the tendency of the growth season temperature carried over to the dry-season temperature. As a result, the factor loading of BC–temperature (dry) on PC1 was large.

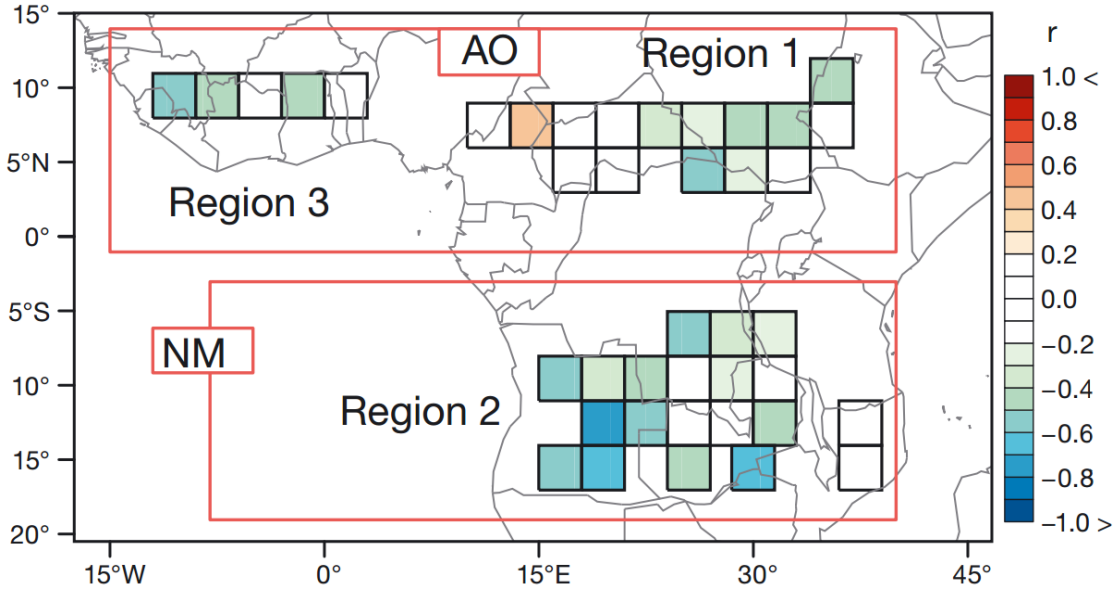

Fig. 2.6. Correlation coefficients between precipitation and temperature during the growing season during 1997–2008. AO: August to October; NM: November to May.

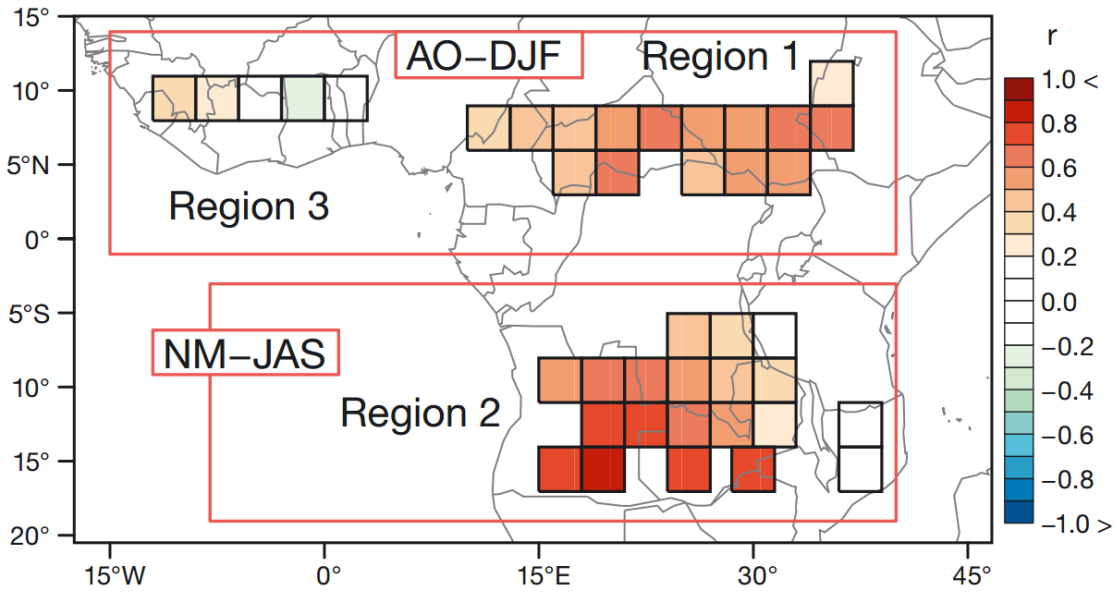

Fig. 2.7. Correlation coefficients for temperature between the growing and dry seasons during 1997–2008. AO: August to October; DJF: December to February; NM: November to May; JAS: July to September.

We interpreted PC1 as the response pattern of vegetation productivity to temperature and precipitation during the growing season. The geographical distribution pattern of PC1 depended greatly on the geographical distribution of biomes (Fig. 2.8).

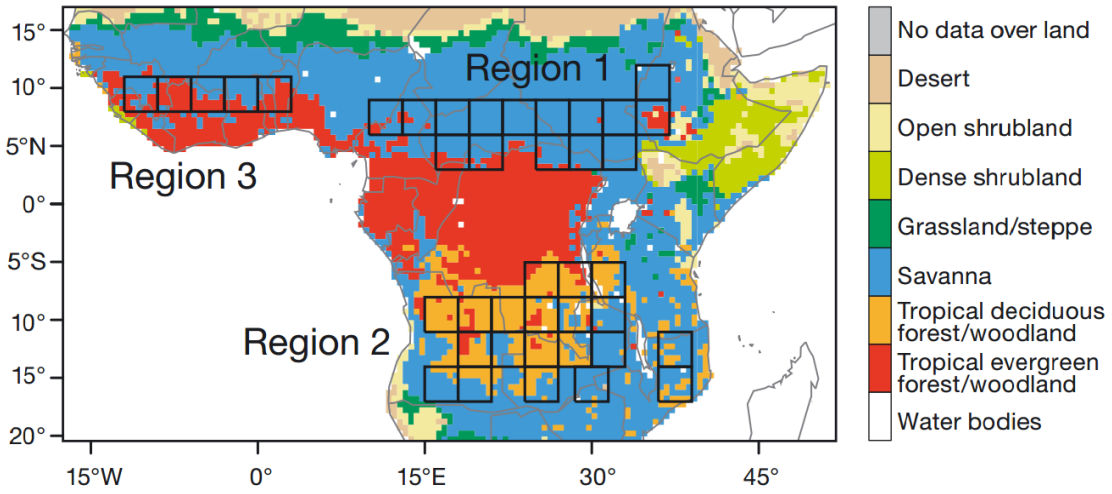

Fig. 2.8. Biome distributions in central Africa.

In Region 1, the dominant biome is savannah throughout. The northern part of Region 2 is dominated by tropical deciduous forest, and the southern part is dominated by savannah. Both tropical evergreen forest and savannah are also found in Region 3. The PC1 scores differed among these 3 biome types (Fig. 2.9). In the savannah, 68% of the large grid cells had negative PC1 scores, and 67% of the large grid cells in tropical deciduous and evergreen forest had positive PC1 scores. This indicates that the BC emission rate increased with the growing-season precipitation in the savannah and the growing-season temperature in tropical deciduous and evergreen forests. Hickler et al. (2005) and Anyamba and Tucker (2005) showed that in semi-arid regions with abundant herbaceous species, NDVI and LAI are sensitive to precipitation changes. In contrast, in forested regions, Allen et al. (2010) showed that vegetation productivity is more affected by temperature and solar radiation than by precipitation. These differing dependencies of vegetation production among the biomes would explain the differentiation in the sign of PC1.

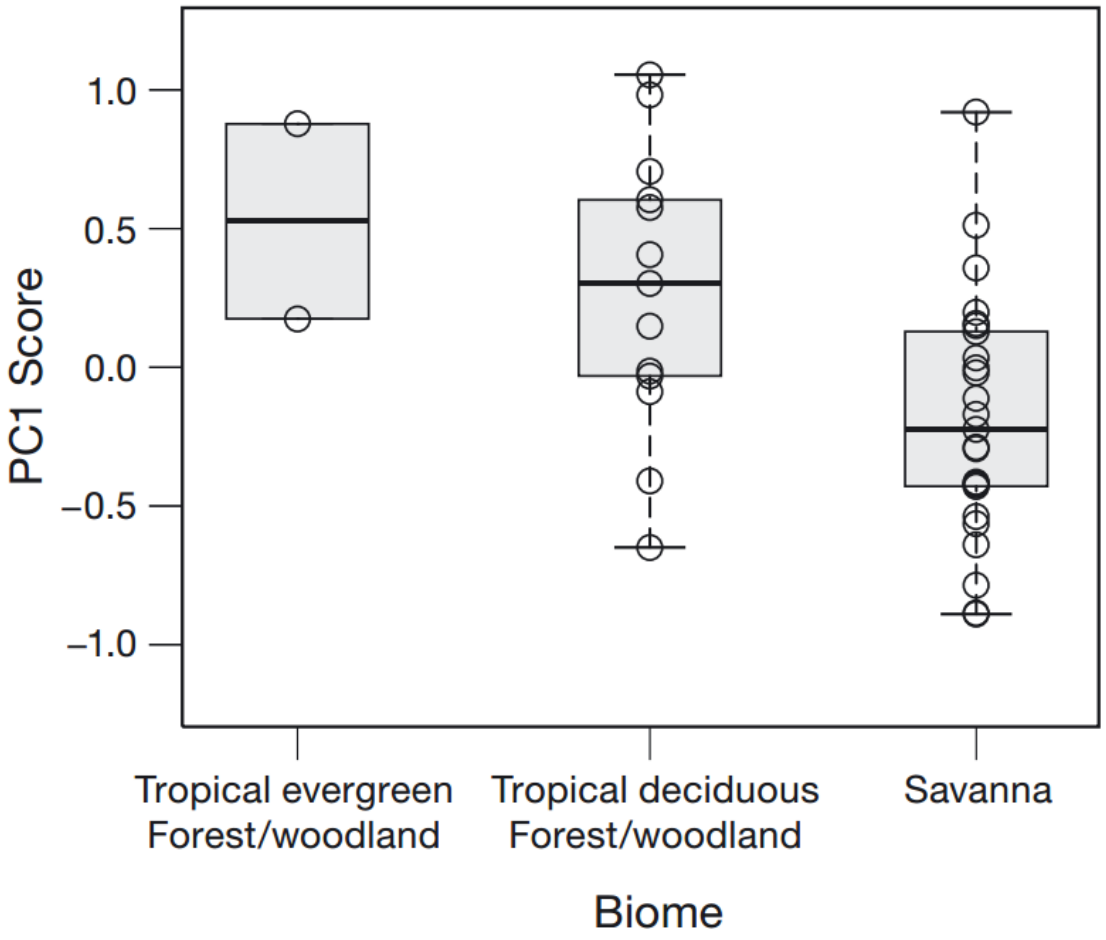

Fig. 2.9. Principal component 1 (PC1) scores averaged by biome type. Circles: PC1 score in each grid cell classified into a biome type; bottom and top of each box: lower and upper quartiles, respectively; bold horizontal line in the middle of the box: median value.

2.4.3 2nd Principal Component

PC2 can be more intuitively understood if the factor loading of BC−cloud cover (growing) on PC2 is compared with that of BC−Sd (growing), where Sd indicates the intensity of the downward shortwave radiation. Sd is inversely correlated with cloud cover, so the correlation coefficients for BC− cloud cover (growing) and BC−Sd (growing) should have opposite signs.

In large grid cells with positive PC2 scores, LAI increased in years with more precipitation, and Sd was higher during the growing season. This suggests that both the BC emission rate and the burned area increased during years of higher vegetation productivity. We therefore interpret positive PC2 scores as the response patterns of vegetation productivity (i.e. the fuel-loading response pattern) to precipitation and Sd

during the growing season.

In contrast, in large grid cells with negative PC2 scores, the BC emission rate either increased or showed no relation to decreases in precipitation, Sd and LAI during the growing season. Archibald et al. (2009) and Bond et al. (2003) explained the smaller burned areas in regions with higher tree cover as follows. Higher tree cover reduces the intensity of sunlight reaching the forest floor, thus hindering the growth of grass. Furthermore, the ignition frequency is reduced because grass and litter on the forest floor are prevented from drying out, and wildfires do not spread. Archibald et al. (2009) and Scholes (2003) suggested that wildfires rarely occur when the tree cover exceeds about 40%. We compared the PC2 scores for tree cover and LAI with PC2 scores in some subsets of large grid cells (Fig. 2.10). The mean ± SD tree cover was 42.4 ± 5.5%, and the average LAI was 2.2 ± 0.5 m^2m^{-2} in large grid cells with PC2 scores lower than −0.2. Therefore, in large grid cells with negative scores, lower precipitation and Sd reduced the tree cover and increased the burned area, increasing BC emissions.

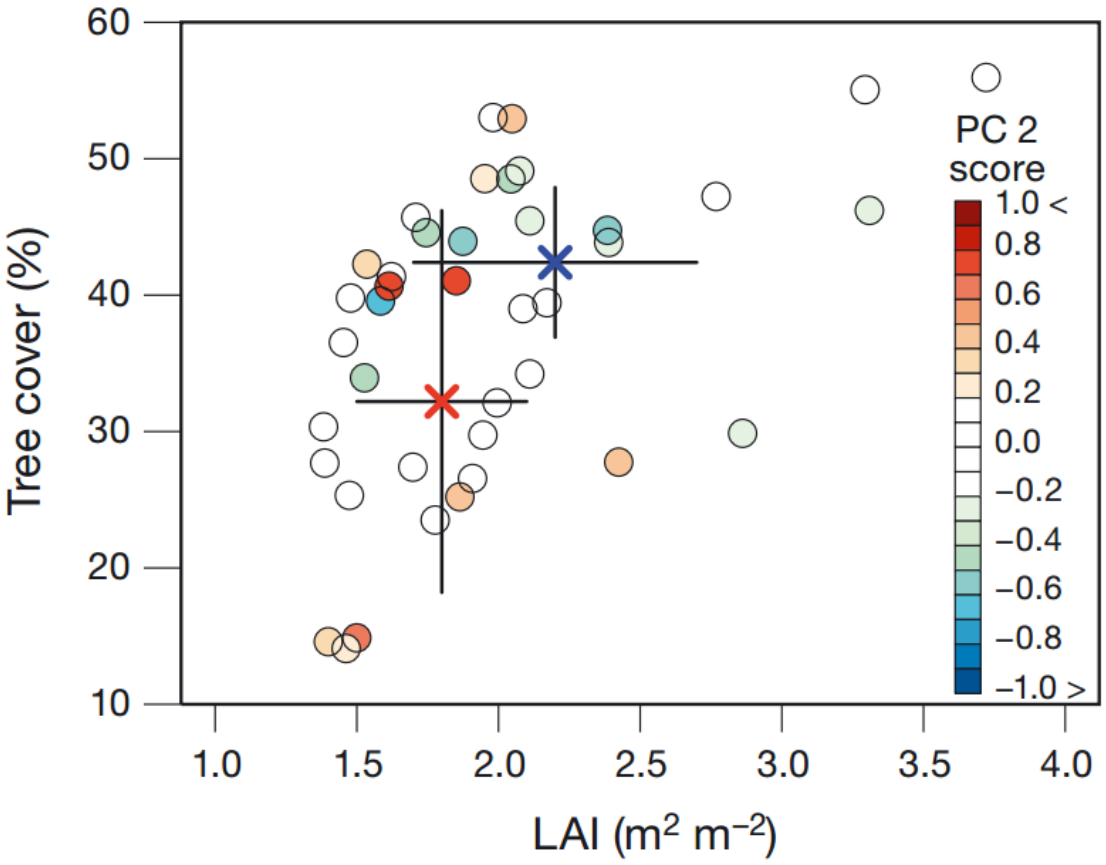

Fig. 2.10. Relationships among the principal component 2 (PC2) scores (color scale), tree cover and leaf area index (LAI). The average for grid cells with scores smaller than −0.2 is shown by a blue X, and the average for grid cells with scores larger than +0.2 is shown by a red X. The standard deviations of tree cover and LAI are respectively shown by the vertical and horizontal gray lines passing through each average.

2.5 Summary

We used PCA to extract factors accounting for the spatial variations of the correlations between BC and the climate variables, or between BC and LAI. We interpreted PC1 (contribution ratio, 39.5%) as mainly reflecting the response of vegetation productivity to temperature and precipitation during the growing season. This pattern is regulated primarily by biome type. We interpreted PC2 (contribution ratio, 18.0%) as a geographical distribution pattern primarily regulated by tree cover, which in turn regulates the abundance of herbaceous vegetation. The cumulative contribution ratio of the vegetation productivity response (57.5%; PC1 and PC2) was much higher than the contribution ratio of climate variables in the dry season (14.1%; PC3). From these findings, we concluded that the spatial variations of the correlations between BC and the climate variables, or between BC and LAI, primarily reflect biome type and tree cover, both of which differed considerably among the 3 regions studied.

The geographical distribution patterns of BC emissions may change if the distribution of vegetation types changes under future climate change in Africa. Therefore, future studies should examine the impact of predicted changes in vegetation and biome distributions on BC emission patterns and how, in turn, BC emission pattern changes are likely to affect future climate.

Chapter 3

The Relationship between Wildfire Carbon Emissions and Cyclic Variations in Precipitation and Temperature over Africa

3.1 Introduction

Precipitation primarily controls the spatio–temporal patterns of wildfires in terms of frequency and intensity through regulation of vegetation biomass, which functions as the fuel load (Bowman et al. 2009; Ishii et al. 2013). For example, an analysis of NOAA-AVHRR data revealed that the spatial distribution of annual precipitation and a marked dry season primarily control the spatial distribution of wildfire frequency (Koffi et al. 1995; Jennifer et al. 1999) and the amount of BC emissions from wildfires (Cooke et al. 1996). It has also been shown that wildfires in southern Africa occur more frequently in years with higher annual precipitation (Jennifer et al. 1999). However, the frequency of wildfires is reduced in areas with more than 1000 mm of annual precipitation because these climatic conditions allow forest ecosystems to develop, ensuring that land surfaces remain moist (Archibald et al. 2009). Using a dynamic global vegetation model (DGVM) and a fire model, Lehsten et al. (2009) revealed that the burned area and carbon emissions from wildfires were highest in regions with an annual precipitation of approximately 1000 mm.

Spatiotemporal patterns of carbon emission from wildfires in Africa are also

controlled by periodic climatic perturbations that regulate vegetation productivity (Patra et al. 2005; Riaño et al. 2007). One of the major causes of these periodic perturbations is the inter-annual variability of sea surface temperature (SST) (Lu and Delworth 2005), including the Atlantic multi-decadal oscillation (Zhang and Delworth 2006), the Indian Ocean dipole (Black et al. 2003), and the El Niño–Southern Oscillation (ENSO) (Hulme et al. 2001). The ENSO is strongly correlated with the normalized difference vegetation index (NDVI) in Africa. The NDVI is an index of vegetation greenness and therefore is associated with biomass production (Anyamba et al. 2003). However, the effects of such periodic perturbations of climate on the emission of carbon aerosols from wildfires have not been analyzed in a systematic way.

Here, we quantitatively evaluated the effect of the periodic inter-annual variability in annual precipitation and annual mean temperature on carbon emissions from wildfires over the African continent. We used the spatially explicit individual-based dynamic global vegetation model (SEIB-DGVM) (Sato et al. 2007). The SEIB-DGVM reconstructs the geographical distributions of observed vegetation indices including biome, net primary production, and fire frequency (Sato et al. 2007). Additionally, the SEIB-DGVM explicitly considers the size-dependent mortality of trees when a fire occurs. In Africa, this size-dependency has been shown to be a necessary prerequisite for maintaining savanna by permitting the coexistence of trees and grasses (Hanan et al. 2008; Higgins et al. 2000; Sankaran et al. 2004), particularly in areas where the mean annual precipitation exceeds 650 mm (Sankaran et al. 2005).

3.2 Methods

3.2.1 Overview of the Modified Model

We evaluated how cyclical variation in precipitation and temperature influenced carbon emissions from wildfires over the African continent using a dynamic global vegetation model, namely SEIB-DGVM (Sato et al. 2007). In the study, we used a version of the model that was modified for the African continent (Sato and Ise 2012). Here, we provide only a brief description of the major processes and the fire sub-model of the SEIB-DGVM. Each grid cell is represented by a 100 × 100-m spatially explicit virtual forest, where individual trees become established, compete, and die. A grass layer can establish under the tree canopy layer. Simulations begin from bare ground with several plant functional types (PFTs) that are favored by the environmental conditions of each grid cell (1 × 1 m). Two woody PFTs (evergreen and rain-green) and two grass PFTs (C_3 and C_4) are assigned for Africa in the model. A woody PFT and a grass PFTs usually coexist in the model.

In the modification of the model for the African continent, Sato and Ise (2012) replaced the fire sub-model of the SEIB-DGVM with a sub-model of the adaptive dynamic global vegetation model (aDGVM) (Scheiter and Higgins 2009), which is well trained and validated for Africa. This is a semi-empirical sub-model that is based on field observations made in the savanna of southern Africa. In the sub-model, fire can only occur when the potential intensity of the fire energy exceeds a site threshold. This intensity of potential energy is estimated as a function of the fuel load, fuel moisture, and wind speed. The probability of fire (F_{prob}) diminishes with an increase in the proportion of tree canopy coverage in the stand (TC: 0–100 %).

$$F_{prob}(T_c) = 0.015(0.1 - 8.33 \times 10^{-6} \times \mathrm{TC})\,. \tag{3.1}$$

The F_{prob} is reduced by 80% when TC is 40–65% and by 100% when TC is 65–100% (Archibald et al. 2009). This sharp deceleration in F_{prob} occurs because higher TC reduces the amount of sunlight on the forest floor, resulting in greater retention of moisture in the fuel load. Lower levels of sunlight arriving at the forest floor also decrease the grass biomass, which is a major source of fuel load. Refer to Appendix B for a more detailed description of the fire model.

3.2.2 Climate Data for Simulation

We simulated wildfires in the African continent using 0.5° × 0.5° grid cells. For climatic data to drive the spin-up and the control runs, we used the Climate Research Unit (CRU) observation-based climatic data [CRU-TS 3.0 (0.5 Degree) 1982–2009 monthly climate time series (Mitchell and Jones 2005)] (Fig. 3.1). The time interval of these data is monthly, and hence we supplemented the daily climatic variability within each month using NCEP/NCAR daily climate data (Kalnay et al. 1996) during the corresponding period. Refer to Appendix C for the detailed procedures used to process these data sets.

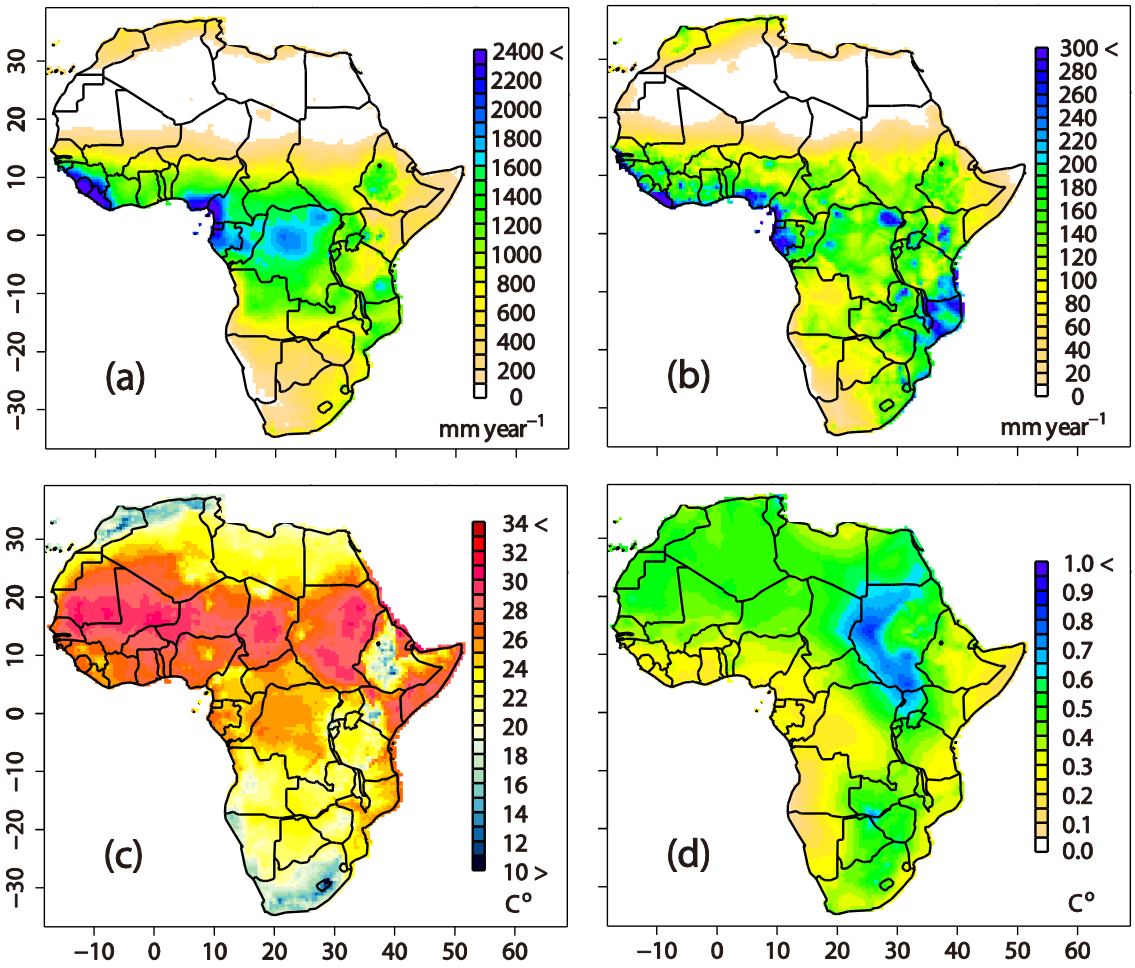

Fig. 3.1. Distribution of precipitation and air temperature over the African continent from CRU data during the period of 1982–2009. (a) average and (b) standard deviation of annual precipitation, and (c) average and (d) standard deviation of annual mean temperature.

To evaluate the influences of inter-annual cyclic variability on the amount of carbon

emitted from wildfires, we conducted no-cycle experiments and cycle experiments. To force each of the no-cycle and cycle experiments, we produced a 20-year climate dataset using the standard climate data. The no-cycle experiment was forced by climate data containing negligible inter-annual variability in either annual air temperature or annual precipitation. The cycle experiment was forced by climate data containing a 20-, 10-, or 6-year cycle of fluctuation for either annual precipitation or annual mean temperature, with either an increasing or decreasing inter-annual trend in the initial phase. We referred to this difference in the phase as phase (±) in this study. Therefore, the no-cycle experiment used two different sets of climate data, whereas the cycle experiment used 12 different climate datasets. Note that the climate data with a 6-year cycle of fluctuation covered only 18 years, so the average annual precipitation or annual mean temperature for this dataset was the same as those for the climate datasets with 20- and 10-year cycles of fluctuation. Refer to Appendix D for the detailed procedures used to process these data sets.

3.2.3 Simulation Procedure

A 2000-year spin-up run from bare ground was conducted by repeatedly inputting climate data and an annual time-series of atmospheric CO_2 during the period 1982–2009. A spin-up of 2000 years is required for soil carbon pools to reach equilibrium. Wildfires occasionally occur during the spin-up run, delivering stochastic variability in the state after a spin-up run. To reduce this effect on the simulations, we prepared five initial states by appending simulations of 5 years after the spin-up of 2000 years by inputting climate and CO_2 data for the periods of 1982–1986, 1987–1991, 1992–1996, 1997–2001, or 2002–2006. In the control run, an annual time series of atmospheric CO_2 during the period 1982–2009 was used. The cycle and no-cycle experiments used an atmospheric CO_2 value of 362.9 ppm, which was the global mean over the period from 1982 to 2009.

3.3 Results

3.3.1 Control Experiment

The spatial distribution of carbon emissions was almost the same as that produced by the Global Fire Emissions Database (GFED) version 3 (Giglio et al. 2010) ($r = 0.40$ ($P < 0.001$), $SDR = 1.18$, $SS = 0.68$) for Africa (30°S–15°N, 17°E–41°E) (Fig. 3.2). Here, r is the spatial correlation between simulation and observation, SDR is the spatial standard deviation ratio of simulation to observation, and SS is a skill score representing a comprehensive evaluation the indices of both spatial correlation and spatial standard deviation. SS approaches 1.0 when the simulation is consistent with observation (See Appendix E for a detailed description).

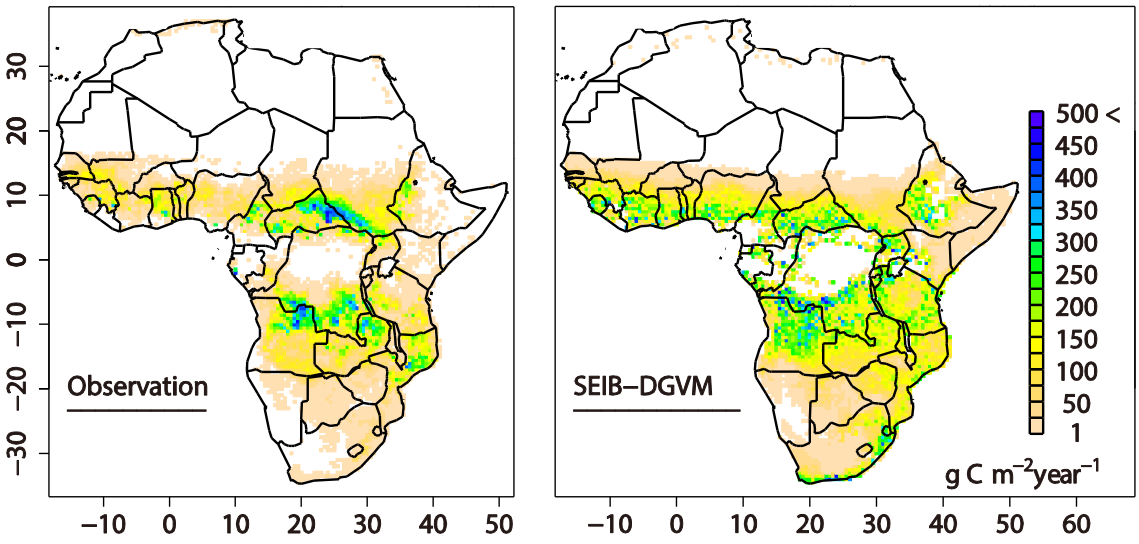

Fig. 3.2. Time-averaged annual carbon emissions from fires during the period of 1997–2009 over the African continent: average of 10 simulations for SEIB-DGVM (right) and GFED (left).

The average (± standard deviation) carbon emission (g C m^{-2} $year^{-1}$) from the simulation was 81.4 ± 2.7 in the northern hemisphere (0°S–15°N, 17°W–41°E) and 101.3 ± 2.6 in the southern hemisphere (30°S–0°N, 5°E–41°E), whereas the observed value was 53.4 in the northern hemisphere and 58.3 in the southern hemisphere. The carbon emission of the simulation was 1.5 and 1.7 times higher than the observed values in the northern and the southern hemisphere, respectively.

The distribution of simulated proportion of tree canopy coverage in the stand (TC%) was coincident with that of the AVHRR Continuous Fields Tree Cover Product (DeFries et al. 2000) for Africa (30°S–15°N, 17°E–41°E) ($r = 0.76$ ($P < 0.001$), $SDR = 1.33$, $SS = 0.81$) (Fig. 3.3).

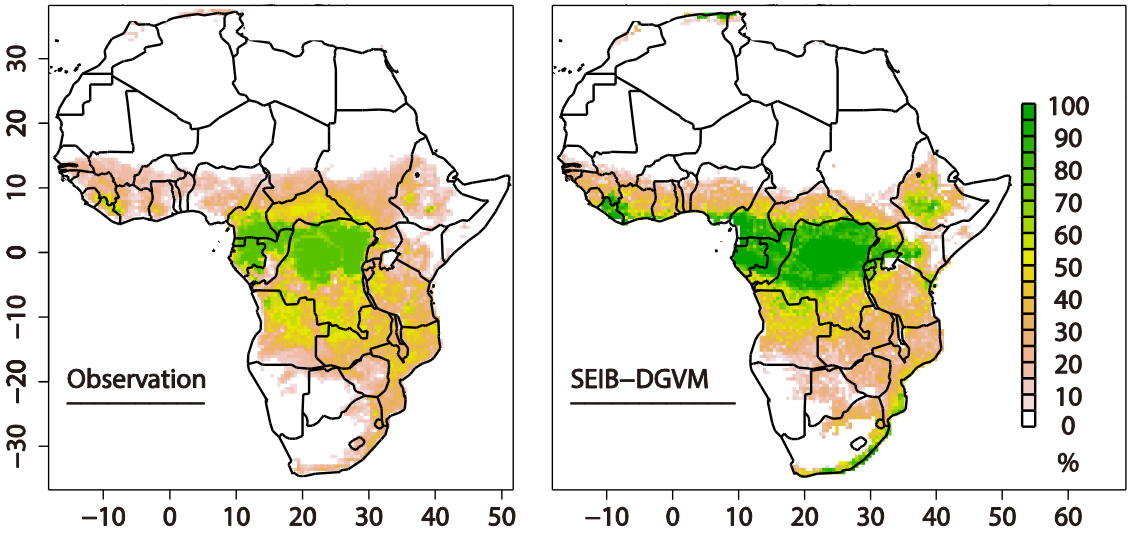

Fig. 3.3. Annual mean tree cover over the African continent: (right) average of 10 simulations using SEIB-DGVM during 1997–2009 and (left) AVHRR Continuous Fields Tree Cover Product (DeFries et al. 2000).

The simulated results of the segmented 0–10, 10–25, 25–40, 40–65, and 65–100% TC in the southern or northern hemispheres agreed with observed values (Fig. 3.4). However, the simulation was 9.6% and 7.9% higher than satellite observations for the 65–100% TC segment of the southern and northern hemispheres, respectively. This tendency to overestimate was particularly strong in central Africa (5°S–5°N, 10°E–30°E).

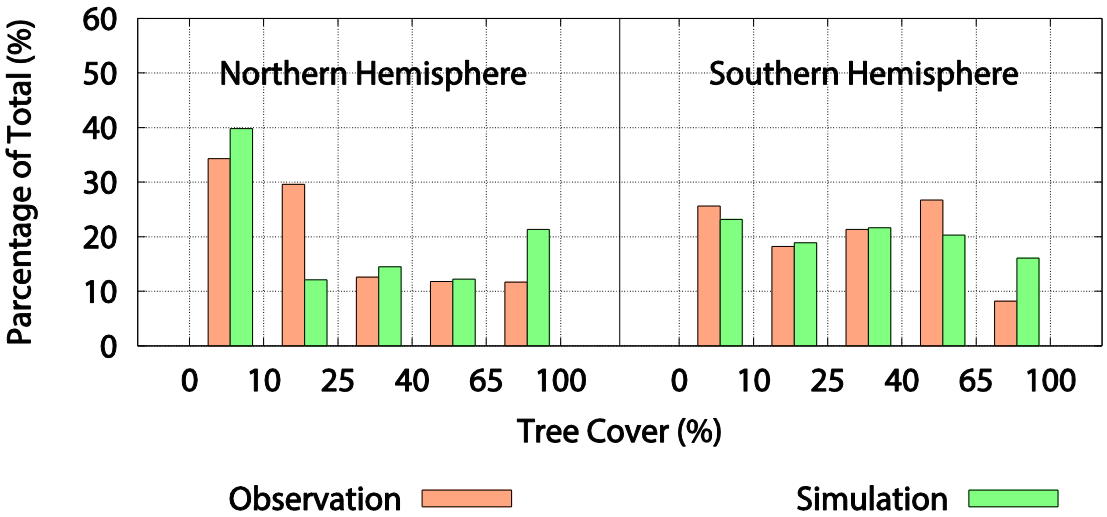

Fig. 3.4. The percentage of the total number of grid cells of each tree cover segment (0–10, 10–25, 25–40, 40–65, and 65–100%) in the northern hemisphere and the southern hemisphere. Green: SEIB-DGVM, orange: VHRR Continuous Fields Tree Cover Product.

The simulated fire intervals for each virtual forest in the savanna region (8°N–13°N, 10°E–35°W and 20°S–10°S, 15°E–35°W) ranged from 2 to 16 years. These values were consistent with the observed fire intervals of 1 to 12 years (Thonicke et al. 2001). The simulated spatial distribution of biomass was approximately the same as the observed biomass distribution estimated by Kindermann et al. (2008) in Africa (30°S–15°N, 17°E–41°E) ($r = 0.69$ ($P < 0.001$), $SDR = 1.76$, $SS = 0.62$). On the other hand, the simulation overestimated total biomass; the simulated and observed total biomasses in Africa (30°S–15°N, 17°E–41°E) were 4.8 and 2.7 kg C m^{-2}, respectively. The total biomass of the simulation was 1.8 times larger than the observed value in Africa.

3.3.2 Precipitation and Temperature No-cycle Experiments

Precipitation and temperature no-cycle experiments shared a similar spatial distribution in the deviation of annual carbon emissions from those observed in the control experiment (Fig. 3.5). This deviation (no-cycle − control) manifested as negative values for the central tropical region (8°S–5°N, 10°E–32°E) and the coast of the Gulf of Guinea (4°N–8°N, 10°W–10°E) and as positive values for the area south of Angola (17°S–15°S, 12°E–20°E) and Tanzania (10°S–0°S, 35°E–40°E). On average, deviations in the northern hemisphere were −15.4 ± 1.4% and −15.1 ± 2.0% for precipitation and temperature in the no-cycle experiments, respectively. In contrast, the southern hemisphere showed negligible deviation in either the precipitation or temperature no-cycle experiments.

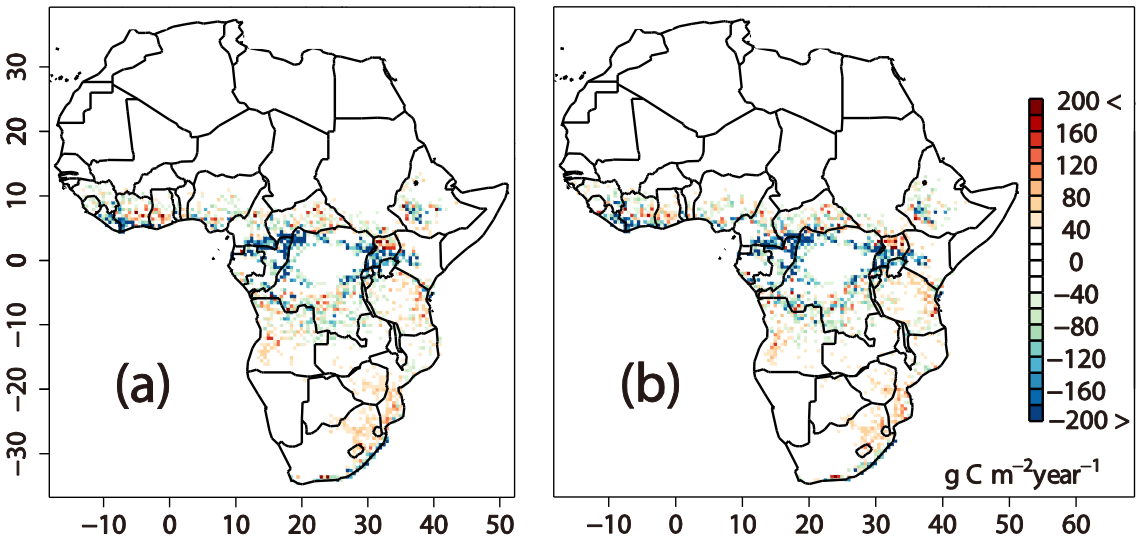

Fig. 3.5. The spatial distribution pattern of the difference in annual carbon emission between no-cycle experiments and control experiments (no-cycle − control): (a) precipitation no-cycle experiments and (b) temperature no-cycle experiments. This annual carbon emission is the average value of 10 simulations over 20 years.

In the precipitation no-cycle experiment, total biomass increased by 9.7 ± 1.4% and 8.3 ± 1.1% in the northern and southern hemispheres, respectively, and in the temperature no-cycle experiment, total biomass increased by 9.4 ± 1.7% and 7.8 ± 1.1% for the northern and southern hemispheres, respectively. Changes in the precipitation and temperature no-cycle experiments showed a similar spatial pattern. Additionally, in both the precipitation and temperature no-cycle experiments, the frequency of fires in central parts of the African continent (5°S–5°N, 10°E–30°E) decreased, by 25.8% and 22.7%, respectively.

For both the precipitation and temperature experiments, the annual carbon emission found for each grid cell in the no-cycle experiments for the 65–100% TC segment was relatively low compared with those in the control experiment in the northern and southern hemispheres (Fig. 3.6). In the southern hemisphere, the carbon emissions in the no-cycle experiments increased compared with that in the control experiments in the 0–40% TC segment. At this time, the percentage of total tree cover in the 40–100% TC segment in the no-cycle experiments was relatively low compared with that in the control experiment in the northern and southern hemisphere.

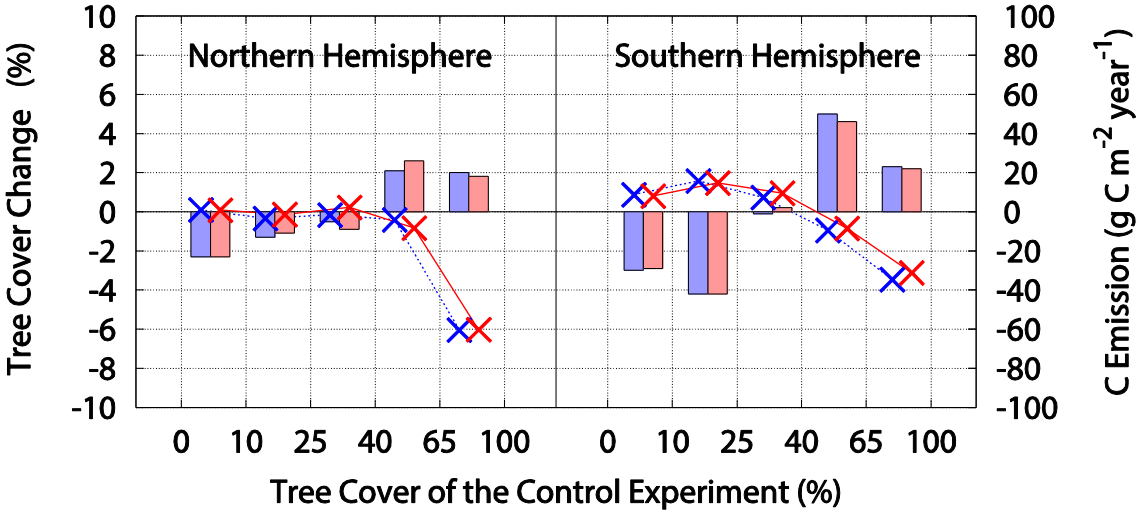

Fig. 3.6. The dependence of the differences in the percentage tree cover on the TC segment and the change in carbon emissions on the TC segment. Bars indicate changes in tree cover (no cycle − control) on the left ordinate. Cross marks indicate changes in carbon emission on the right ordinate (no cycle − control). Blue: precipitation experiment, red: temperature experiment. The abscissa is the TC segment (0–10, 10–25, 25–40, 40–65, and 65–100%). For carbon emissions, the TC segment was defined by the control experiment.

3.3.3 Precipitation and Temperature Cycle Experiments

Carbon emissions were dependent on changes in the precipitation cycle but did not significantly depend on the temperature cycle (Fig. 3.7). In the precipitation cycle experiment, the average carbon emission among the phases increased under a shorter precipitation cycle in the northern hemisphere. These carbon emissions were 2.3%, 3.0%, and 5.2% higher in the precipitation cycle experiment than in the no-cycle experiment for 20-, 10-, and 6-year cycles, respectively. However, these carbon emissions did not differ much in the southern hemisphere and were 1.8%, 2.3%, and 1.9% higher in the temperature cycle experiment than in the no-cycle experiment for the 20-, 10-, and 6-year cycles, respectively. The average carbon emission in all temperature cycle experiments was 1.9%.

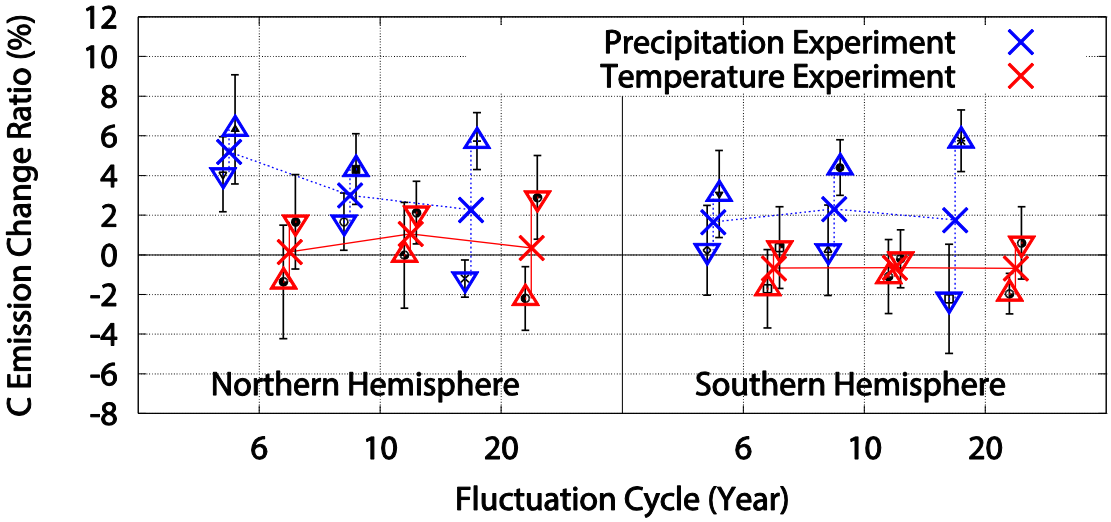

Fig. 3.7. The rate of change in carbon emissions in each cycle experiment compared with the no-cycle experiment. Blue: precipitation experiment, red: temperature experiment. The abscissa is the cycle of annual precipitation fluctuation or annual mean temperature fluctuation. The triangle / inverted triangle indicates the carbon emission of the phase (+) / (–) cycle experiment. In phase (+) / (–), annual precipitation and annual mean temperature increase / decrease in the first half of the cycle, and those variables then decrease / increase in the second half of the cycle. The black bar is the standard deviation across 10 simulations. The cross (X) is the average value of phase (+) and phase (–).

The precipitation phase (+) cycle experiment estimated larger carbon emission than the precipitation phase (–) cycle experiment did, whereas the temperature phase (+) cycle experiment estimated lower carbon emission than the temperature phase (–) cycle experiment did. The 20-year cycle experiment produced the largest difference in carbon emissions among the phases. In the northern hemisphere, the differences in the change ratio between the 20-year cycle experiment and the precipitation and temperature no-cycle experiments were 6.9% and 5.1%, respectively. In the southern hemisphere, the corresponding differences were 8.0% and 2.6%, respectively. In both hemispheres, these values were smaller when the cycle of precipitation or temperature fluctuation was shorter.

For the precipitation experiments, the difference between the cycle experiments and no-cycle experiment in each TC range was assessed. With shorter cycles of precipitation fluctuation, in the northern hemisphere the difference increased in the 0–10% TC range and decreased in the ranges with >40% TC (Fig. 3.8). In the southern hemisphere, the corresponding differences increased in the 0–25% TC range and decreased in the ranges

with >25% TC. However, for the temperature cycle experiment, each TC range varied slightly with the cycle of temperature fluctuation (Fig. 3.8). The difference in the spatial distribution of TC between the 6-year cycle experiment and the no-cycle experiment indicated that TC tended to decline in the precipitation experiment (Fig. 3.9a). However, the difference in TC in the temperature experiment was much smaller because the grid cells where TC increased or decreased were indiscriminately intermixed (Fig. 3.9b).

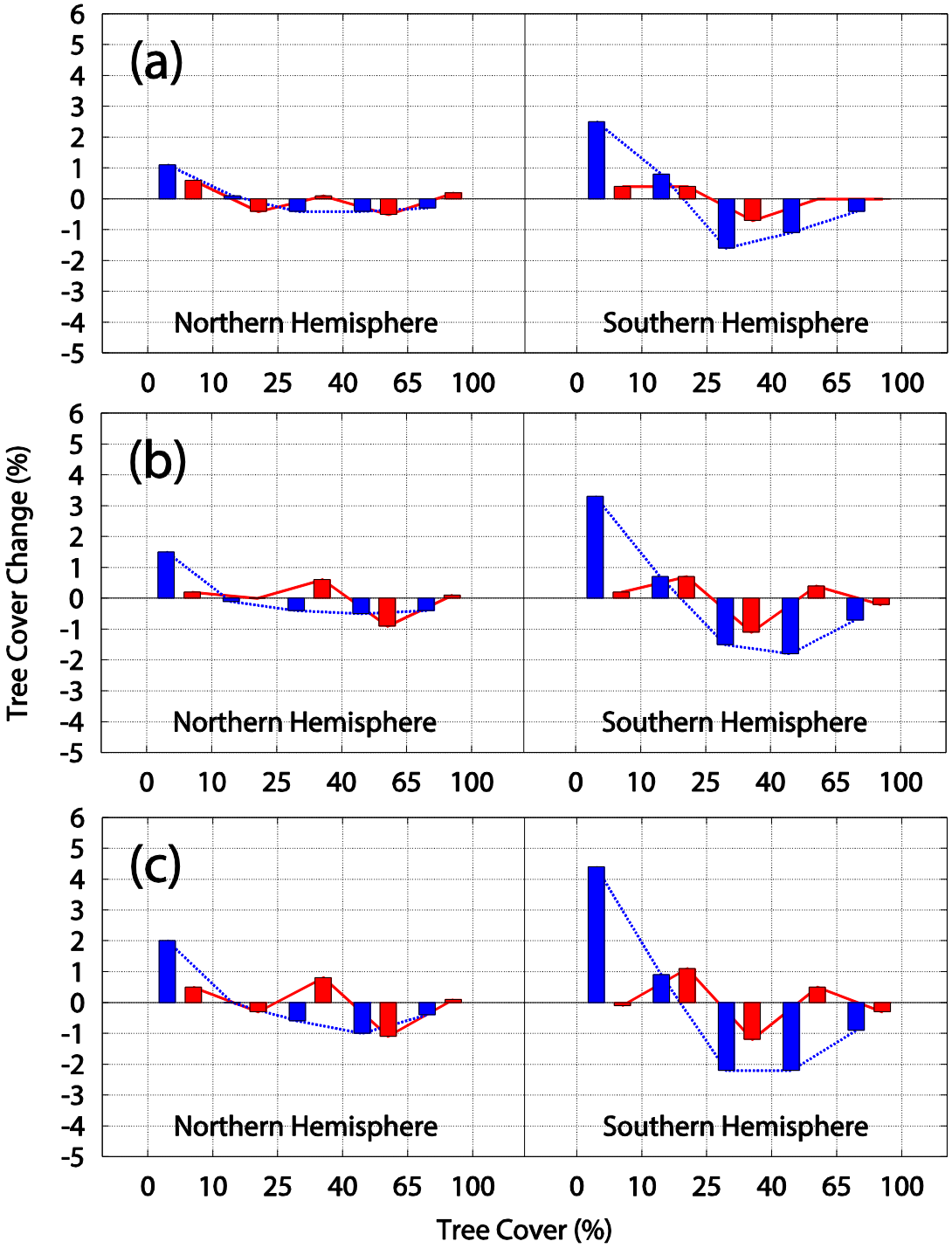

Fig. 3.8. The differences in percentage tree cover in grid cells in each hemisphere between no-cycle experiments and control experiments (cycle – no-control). (a) 20-year cycle experiment, (b) 10-year cycle experiment, and (c) 6-year cycle experiment. The value is the average of phase (+) and phase (–) cycle experiments. Blue: precipitation cycle experiment, red: temperature cycle experiment. The abscissa is the segment of TC (0–10, 10–25, 25–40, 40–65, and 65–100%).

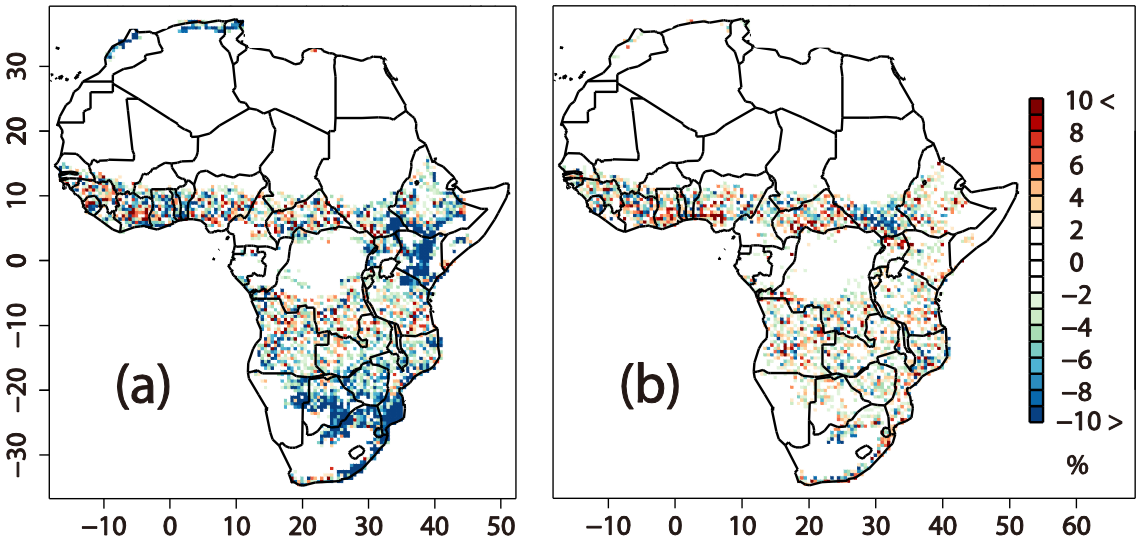

Fig. 3.9. The phase-averaged difference in tree cover between the 6-year cycle experiment and the no-cycle experiment (6-year cycle – no-cycle). (a) precipitation experiment and (b) temperature experiment.

In the grid cells with >40% TC in the precipitation no-cycle experiment, the average carbon emission among the phases increased as the cycle of precipitation fluctuation grew shorter in both hemispheres (Fig. 3.10). In the grid cells with a range of 40–65% TC in the precipitation no-cycle experiment, the change ratio of the 6-year cycle experiment to the 20-year cycle experiment for the average carbon emission among the phases was +87% and +25% for the northern and southern hemispheres, respectively. In the grid cells with >65% TC in the precipitation no-cycle experiment, this change ratio was +27% and +21% in the northern and southern hemispheres, respectively. In the grid cells with 0–40% TC in the precipitation no-cycle experiment, the carbon emissions displayed almost no variation in the northern hemisphere, whereas the carbon emissions decreased in the southern hemisphere. For the temperature cycle experiment, in the grid cells of each TC range, the average carbon emission among the phases was not sensitive to changes in the cycle of temperature fluctuation.

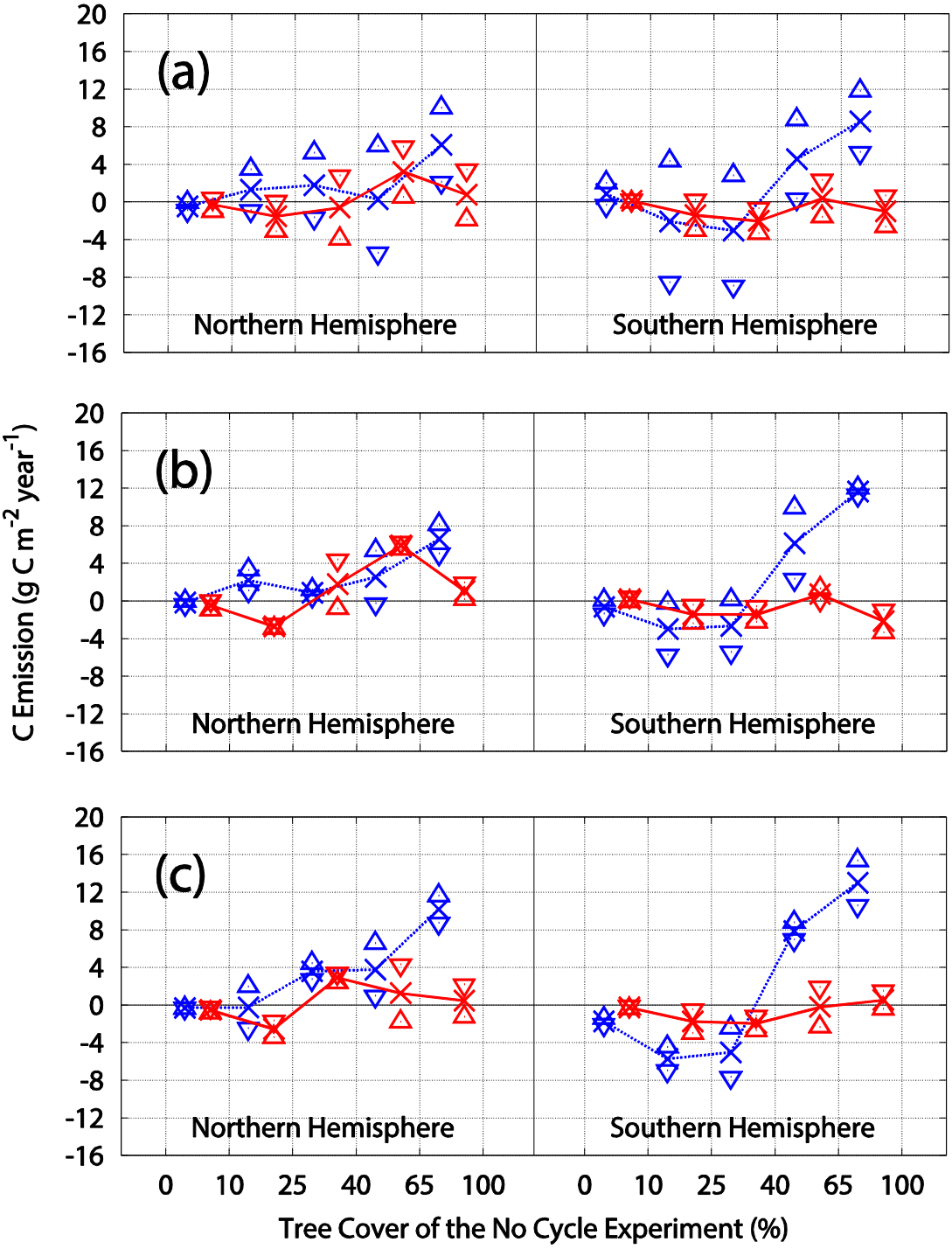

Fig. 3.10. The differences in carbon emissions between cycle experiments and no-cycle experiments in each TC segment defined by no-cycle experiments. (a) 20-year cycle experiment, (b) 10-year cycle experiment, and (c) 6-year cycle experiment. The abscissa is the segment of TC (0–10, 10–25, 25–40, 40–65, and 65–100%). Blue: precipitation cycle-experiment, red: temperature cycle-experiment.

3.4 Discussions

3.4.1 Control Experiment

Values of simulated carbon emission, biomass, and TC in the control run were larger than the observed values. This overestimation was most conspicuous for the coast of the Gulf of Guinea (5N–10°N, 15°W–10°E) and Tanzania (10°S–0°S, 35°E–40°E). We suspect that the overestimation for these two regions was the result of deforestation due to logging and slash-and-burn agriculture before 1997 because deforestation reduces vegetation biomass, resulting in a reduction in the fuel load for wildfires. If this explanation is correct, then carbon emissions, biomass, and TC would have been more similar to the control run before these land-use changes occurred than the present day observations in these regions are. The ratio of carbon emissions from the coast of the Gulf of Guinea to emissions from the eastern part of the same latitude zone (5°N–10°N, 15°E–40°E) was 1.3 during the late 1970s according to FAO observation-based data (Hao and Liu 1994). This ratio was also 1.3 in the control run, but it was 0.5 when using satellite observed carbon-emissions made during 1997–2009, as reported in the GFED (Giglio et al. 2010). Likewise, the ratio of carbon emissions in Tanzania to emissions from the western part of the same latitude zone (5°S–10°S, 10°E–30°E) was 0.9 according to Hao and Liu (1994), 0.7 in the control run, and 0.2 using GFED. Therefore, the spatial distribution of carbon emissions during the 1970s was much closer to that predicted from the control run than were present-day observations in both the coast of the Gulf of Guinea and Tanzania.

The average annual precipitation and air temperature during 1982–2009 over the coast of the Gulf of Guinea were 1681 mm and 26.7°C, respectively. The corresponding values over Tanzania were 955 mm and 23.2°C, respectively. These climatic conditions correspond to tropical monsoon and tropical savanna climates, respectively, in the classification provided by Kottek et al. (2006). The control run resulted in the formation of forest ecosystems in both the coast of the Gulf of Guinea and Tanzania, with 40.2% and 33.0% TC, respectively. In Liberia, the annual deforestation rate due to slash-and-burn agriculture was 1.9% before the civil war in December 1989 (Kofron and Chapman 1995; Poore et al. 1989). Côte d'Ivoire has experienced the highest rate of deforestation in Africa since 1975 (Watson 1991), with an annual deforestation rate of 1.1–2.9% during the period 1990–1997 due to the expansion of cropland. A high deforestation rate was also observed from NOAA-AVHRR satellite data in Nigeria

during the period 1990–1997 (Achard et al. 2002). Tanzania lost 25% of its forest area during the period 1955–2000, as confirmed by data from the Landsat Multispectral Scanner System (MSS) and Enhanced Thematic Mapper (ETM) (Ahrends et al. 2009; Hall et al. 2009).

3.4.2 Precipitation and Temperature No-cycle Experiments

Marked differences in simulated annual carbon emissions were found between the precipitation cycle and no-cycle experiments (Fig. 3.9), whereas there were no distinct differences between the temperature cycle and no-cycle experiments. Precipitation no-cycle experiments indicated lower carbon emissions from wildfires compared with the control run. We suggest that this difference is because the geographical distribution of vegetation in the African continent is more strongly correlated with precipitation than with temperature. Stable annual precipitation in the precipitation no-cycle experiment would result in a cascade reaction resulting in a lower frequency of drought events, lower tree mortality, and higher TC, as shown in Fig. 3.9, which would result in a lower frequency of wildfire. Drought is likely to be the primary determinant of tree mortality in Africa. For example, remote-sensing studies of the Sahel area have suggested that inter-annual perturbations in indices of vegetation greenness such as NDVI and LAI (leaf area index) are primarily controlled by precipitation (Anyamba and Tucker 2005, Hickler et al. 2005). The results of field studies generally suggest that precipitation primarily determines production and plant-species composition in African vegetation (Lwanga 2003; Gonzalez 2001; MacGregor and O'Connor 2002).

In the southern hemisphere, the negligible effect of the no-cycle climate is because the effect of a decrease in fire probability near the equator (i.e., decreased carbon emissions) is offset by the effect of an increase in biomass (i.e., increased carbon emissions). In the southern part of Angola (17°S–11°S, 11°E–17°E), Tanzania (10°S–0°N, 30°E–40°E), and the southeastern part of Africa (29°S–20°S, 25°E–35°E), the second effect was stronger than the first. In these three regions, the carbon emissions from the no-cycle experiment were larger than were those of the cycle experiment. In the control experiment, the averaged TC of the three regions was 28.7%. In the precipitation no-cycle experiment, the average TC of the three regions increased (by 6.6%), and the probability of fire slightly decreased (by 8.2×10^{-5}%) compared with the control experiment. However, biomass significantly increased (by 11.3%) compared with the control experiment. Therefore, we assumed that carbon emissions increased because the increase in biomass provided a fuel load for fires.

3.4.3 Precipitation and Temperature Cycle Experiments

Although the temperature cycle experiment did not indicate clear changes in carbon emissions from wildfires, it did show higher carbon emissions from wildfires. The underlying reason for the higher carbon emissions in the precipitation cycle experiment is tree mortality due to drought stress induced by fluctuations in precipitation. While higher mortality results in lower biomass and therefore a reduced fuel load, it also results in lower TC, which can increase the frequency of fires. The number of grid cells with 40–100% TC in the no-cycle experiment was larger than that in all of the cycle experiments (Fig. 3.8).

In the northern hemisphere, carbon emissions increased when the cycle of precipitation fluctuation was shorter (Fig. 3.7). This was because the number of grid cells with more than 40% TC decreased because the frequency of tree mortality increased when the cycle of precipitation fluctuation was shorter (i.e., the frequency of extreme droughts increased) (Fig. 3.8). The carbon emissions in grid cells with less than 40% TC was higher than that in grid cells with more than 40% TC because the probability of fire in the former was higher than the in latter. The rate of increase in carbon emissions in the cycle experiments was higher in grid cells with more than 40% TC in the no-cycle experiment (Fig. 3.10). However, in the southern hemisphere, carbon emissions were not significantly affected by the cyclic variation in precipitation. Near the equator, carbon emissions increased due to the operation of this mechanism in grid cells with intrinsically high TC. However, unlike the northern hemisphere, there was a mechanism operating that decreased carbon emissions in the southern hemisphere. The biomass significantly decreased in many grid cells during the cycle experiments (Fig. 3.11), with an accompanying decrease in carbon emissions. Therefore, carbon emissions did not vary with cyclic variation in precipitation.

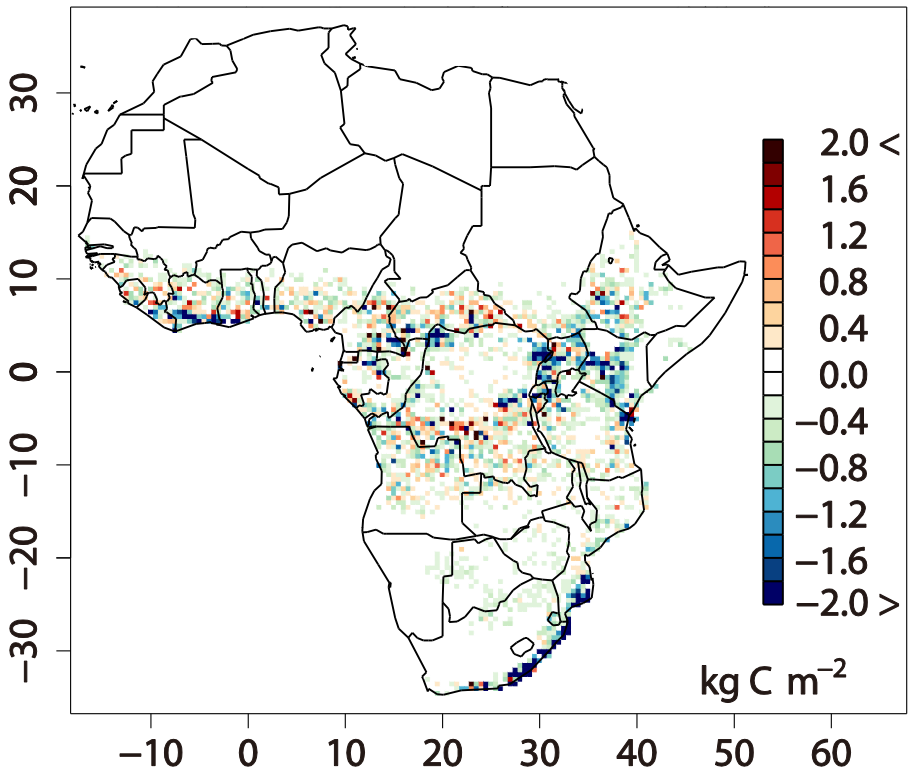

Fig. 3.11. The phase-averaged difference in biomass between the 6-year precipitation cycle experiment and precipitation no-cycle experiment (6-year cycle – no-cycle).

There was a significant difference in carbon emissions between phase (+) and phase (–) of the cyclic variation in precipitation. A pattern arose whereby precipitation increased in the first half of the cycle (i.e., phase (+)), and the average carbon emission was output as a high value (Fig. 3.7). Although this tendency was found in all of the cycles of precipitation fluctuation, the most significant difference in carbon emissions was recorded among the different phases in the 20-year precipitation cycle experiment.

The reason for the difference in carbon emissions among phases was as follows. In phase (+), the increase in the vegetation biomass was large during the first half of the cycle because precipitation increased in locations where exuberant vegetation was present after the spin-up. This increased biomass burned during the second half of the cycle, emitting a large amount of carbon.

However, because the biomass accumulated during the spin-up burned during the early half of cycle, when it was dry due to the limited precipitation. Therefore, the biomass could not increase significantly during the second half of the cycle. Therefore,

carbon emissions in phase (+) were larger than in phase (–) of the precipitation experiment. The 20-year precipitation cycle experiment produced the greatest difference in carbon emissions among the phases. In situations where the precipitation increased in the early half of the cycle, the average difference in biomass between the 10-year period when precipitation increased and the last 28 years of the spin-up was 0.40 kg C m^{-2} for all of the African continent (30°S–15°N, 17°E–41°E). However, in situations where precipitation decreased in the first half of the cycle, the average difference in the biomass between the 10-year period when precipitation increased and the 10-year period when precipitation decreased was 0.29 kg C m^{-2} for the entire African continent. The latter value was lower than the former, supporting our explanation.

In the temperature phase experiment, the carbon emission of phase (+), when temperatures increased in the first half of cycle, was low compared with the carbon emission of phase (–), when there was a decline in temperature in the first half of the cycle. The main mechanism underlying this difference is as follows. In all of the temperature phase experiments, annual precipitation was suppressed, so inter-annual variability was small. Therefore, the biomass increased during the period of simulation. However, the probability of a fire's occurring became higher in the high-temperature period. Because the probability of fire was higher before the enormous increase in biomass in the phase (+) experiment, the amount of biomass burning in the phase (+) experiment was lower than that in the phase (–) experiment, in which temperature increased in the second half of the cycle. In the 20-year temperature cycle experiments, the ratios of carbon emission, amount of biomass, and the probability of fire between phase (+) and phase (–) in a high-temperature period were 0.94, 0.90, and 1.02, respectively.

3.5 Summary

We simulated carbon emissions from wildfires over the African continent using a dynamic global vegetation model (SEIB-DGVM) under the following climatic forcing conditions: (1) a control condition using observation-based climatic data; (2) negligible inter-annual variation in annual precipitation or annual mean air temperature; and (3) cyclic inter-annual variability in precipitation or air temperature at a frequency of 20, 10, and 6 years. The control experiment, reconstructed a reasonable spatial distribution of the observed carbon emissions from wildfires in Africa. In the experiment with negligible inter-annual variation in annual precipitation and temperature, carbon emissions in the northern hemisphere decreased by 15.4% and 15.1%, respectively, compared with the control experiment, whereas there was no clear difference for the southern hemisphere. In the experiment with negligible inter-annual variation in annual precipitation, drought-induced tree mortality decreased, and hence both biomass and TC increased. The increase in biomass resulted in greater carbon emissions from fire due to the provision of a greater fuel load, while the increase in TC decreased carbon emissions from fires because the soil surface remained moist. In the northern hemisphere, carbon emissions decreased because the effect of a greater fuel load exceeded the effect of moist soil. However, in the southern hemisphere, the change in carbon emissions was much smaller because these two effects offset each other.

Carbon emissions were higher for the precipitation cycle experiment than for the precipitation no-cycle experiment at all of the cyclic intervals tested. There was no clear difference in the carbon emissions between the temperature cycle experiment and the temperature no-cycle experiment. The higher frequency of fire, as a result of higher tree mortality and lower TC, is a possible cause of the higher carbon emissions in the precipitation cycle experiment.

In accordance with this explanation, carbon emissions increased under the shorter precipitation cycle in the northern hemisphere. The reason for this is that the number of grid cells with more than 40% TC decreased due to the increased frequency of tree mortality when the cycle of precipitation fluctuation became shorter, resulting in higher fire frequency. However, there was little difference in the southern hemisphere. This was due to the offsetting of the reduced probability of fire (carbon increasing) due to the reduction in TC (i.e., 40–100%) by the effect of increased biomass (carbon decreasing).

There were differences in carbon emissions between the phase (+) and phase (–) cycle experiments because the biomass production rate of phase (+) was higher than that of phase (–).

Our study indicates that the pattern of inter-annual variability in precipitation changes the amount of carbon emitted from wildfires. Therefore, to improve climate predictions over the African continent, there is a need to estimate not only the effect of carbonaceous aerosol from wildfires on mean precipitation but also the effect of carbonaceous aerosol from wildfires on the pattern of inter-annual variation in annual precipitation, such as the presence or absence of cyclic variations, cycles of fluctuation, and phases.

Chapter 4

Projection of Future Black Carbon Emission from Wildfire in Africa

4.1 Introduction

The distriution of vegetation at continental geographic scale is basically under control of climatic conditions (Holdridge 1947; Whittaker 1979). While, major determinants of vegetation growth (temperature, precipitation, and atmospheric CO_2 concentration) have been changed significantly since the preindustrial time, and such changes are forecasted to be accelalated during 21st century (IPCC 2007). Indeed, a multimodel comparison of climatic predictions under the Special Report on Emission Scenarios (SRES) A1B carbon emission scenario (Solomon et al. 2007) over the African continent at the end of the 21st century showed the increment in annual mean surface temperature throughout the African continent, the increment in annual precipitation around the eastern part, and the decrease in precipitation around the southern part from June to November.

Climatic conditions and atmospheric CO_2 concentration significantly affect the water and nutrient use efficiency of vegetation (Drake et al. 1997; Ehleringer et al. 1997). For example, paleo-ecological studeies showd that increasing atmospheric CO_2 concentration resulted in increasing abundance of tree species in savanna ecosystem (Bond et al. 2003), which is characterized by co-occurance of C_3 trees and C_4 grasses

(Sarmiento 1984). This is suggested to be caused by the fact that higher atmospheric CO_2 enhances photosynthesis efficiency for of C_3 plants but not for C_4 grass.

In the African continent, wildfire substantially affects the structure, dynamics, and distribution of vegetation (Higgins et al. 2000, 2007; Sankaran et al. 2004, 2005; Bond et al. 2005a), which results in significant discrepancies between potential and actual biomasses (Bond et al. 2005b; Sankaran et al. 2005; Higgins et al. 2007). Fire induced mortality for trees in Africna savanna is known to have size-dependency; when fire occurs, small trees (<2 m height) are often completely die, while large trees (>2 m height) escape with a high probability (Higgins et al. 2000). Therefore, for adequate reconstruction of the fire related plant-dynamics in the African continent, it is necessary to employ an individual-based dynamic global vegetation model.

A study projects that the African biomass will be doubled during the 21st century under the IPCC SRES A1B scenario (Scheiter and Higgins 2009; Higgins and Scheiter 2012). Their study employed the individual-based adaptive dynamic global vegetation model (aDGVM) which contain the above mentioned size-dependent mortality bu fire. Sato and Ise (2012) also projected African biomass increase by 42.5% during 21st century under the IPCC SRES A1B scenario using the spatially explicit individual-based dynamic global vegetation model (SEIB-DGVM) (Sato et al. 2007). These study indicate that biomass in African vegetation arose in association with the increment in atmospheric CO_2 concentration.

Spatial distributions of BC emission from wildfire over the African continent are basically under control of precipitation, because precipitation primarily controls the spatio–temporal patterns of wildfires in terms of frequency and intensity through regulation of vegetation biomass, which functions as the fuel load (Bowman et al. 2009; Ishii et al. 2013). in fact, an analysis of satellite observed data showed that spatial distributions of annual precipitation and BC emission have tight correlation in the African continent (Koffi et al. 1995; Cooke et al. 1996). An analysis of NOAA-AVHRR data revealed that wildfires in southern Africa occur more frequently in years with higher annual precipitation because vegetation biomass can supply sufficiency fuel (Jennifer et al. 1999). While, we should keep in mind that the increase in tree cover can reduced wildfire frequency, because closed canopy of forests keep land surface moist (Archibald et al. 2009). In savanna region of Africa, simulation study showed that a warmer climate condition have a stimulating effect on frequency of wildfire by drying

out fuel (Hoffmann et al. 2002).

The previous study (i.e., Scheiter and Higgins 2009; Higgins and Scheiter 2012; Sato and Ise 2012) suggested that BC emission from wildfire may increase during the 21st century due to the increase in biomass. However, the change in BC emission from wildfire and frequency of wildfire has yet to be adequately evaluated quantitatively. Thus, we evaluated the change of BC emission from wildfire during 21st century under the IPCC SRES A1B scenario in the African continent using the SEIB-DGVM (Sato et al. 2007). Here we conducted two kinds of experiments. One is the future experiment: annual time-series of global mean atmospheric-CO_2 of the SRES A1B emissions scenario during 2001 to 2100 was employed for the 21st century. The other is the suppressed CO_2 increment experiment: annual time-series of global mean atmospheric CO_2 concentration was employed during 2001 to 2010, and then global mean atmospheric CO_2 concentration in 2010 was employed after 2010.

4.2 Methods

4.2.1 Overview of the Modified Model

We simulated how BC emission from wildfire changes under the forecasted climatic condition during 21st century over the African continent (37°S–34°N, 17°W–59°E). For all simulations, we employed the SEIB-DGVM (Sato et al. 2007) with modifications to the African continent (Sato and Ise 2012). Refer to the subsection 3.2.1 for brief SEIB-DGVM description.

4.2.2 Fire Sub-model

In the modification for the African continent, Sato and Ise (2012) introduced the fire sub-model of the aDGVM (Scheiter and Higgins 2009), which is well trained and validated for Africa. Refer to the subsection 3.2.1 and Appendix B for detailed fire sub-model description.

4.2.3 Soil Moisture Content

To control photosynthetic rate and stomatal conductance as a function of soil moisture content, SEIB-DGVM defines the physiological status of water availability ($stat_{water}$) as follows.

$$stat_{water} = \frac{pool_w - W_{wilt}}{W_{fi} - W_{wilt}}, \tag{4.1}$$

where $pool_w$, W_{fi}, and W_{wilt} indicate the fraction of volumetric soil water content within the rooting depth (500 mm), the soil moisture at field capacity, and the soil moisture at wilting point, respectively. The non-water stressed photosynthesis rate of each PFT is multiplied by

$$2 \times stat_{water} - stat_{water}{}^2 . \tag{4.2}$$

This function reconstructs a generally observed phenomenon in which the ratio of actual evaporation to potential evapotranspiration has high sensitivity to soil water content near the wilting point, while sensitivity is reduced near field capacity (Dunne

and Leopold 1978).

4.2.4 Stomatal Conductance

The single-leaf photosynthetic rate under light saturation (p_{sat} in μ mol CO_2 m^{-2} s^{-1}), is calculated by multiplying its potential maximum of photosynthetic rate ($PMAX$) by the coefficients of temperature (ce_{tmp}), CO_2 level (ce_{co2}), and soil water effects (ce_{water}).

$$p_{sat} = PMAX \times ce_{tmp} \times ce_{co2} \times ce_{water}\,, \tag{4.3}$$

where ce_{tmp} is a bell-shaped curve that reaches the maximum (1.0) at the optimum temperature. ce_{co2} depend on atmosphric CO_2 consentration. ce_{water} is the water availability effect coefficient as follows:

$$ce_{water} = \sqrt{stat_{water}}\,. \tag{4.4}$$

Refer to Appendix F for a detailed Stomatal Conductance description.

4.2.5 Climate Data for Simulation

We simulated the African continent with 0.5°×0.5° grid cells. In simulations for the first 10 years of the 21st century, we used observation-based climatic data of the Climate Research Unit (CRU) [CRU-TS3.2 0.5 degree 2001–2010 monthly climate time series (Mitchell and Jones 2005)]. In simulations for the rest of 21st century, we used MIROC-AGCM output (Emori et al. 2005; K-1 Model Developers 2004) simulated with the SRES A1B CO_2 emission scenario. Because spatial resolution of the MIROC data was provided at the spatial resolution of 126×64 global grids, this data was linearly interpolated to 0.5° grid mesh for our simulations. In order to achieve consistency between the data sets of MIROC and CRU for the period of 2001~2010, MIROC data were converted using the CRU data of the period of 2001~2010. For each climatic item in each month in each grid cell, averages of MIROC results during the period of 2001~2010 were subtracted from the MIROC 21st century projections, and then averages for 2001~2010 of the CRU were added. Because both the CRU and MIROC data sets are provided as monthly data, diurnal variability within each month was supplemented using NCEP/NCAR reanalysis daily climatic data (Kalnay et al. 1996). See Appendix A8 of Sato and Ise (2012) for detailed procedures for processing these data

sets.

Figure 4.1 shows the annual precipitation and annual mean surface temperature during 2001-2010, and their changes during 2001-2010 to 2081-2100. Annual precipitation increased for the eastern part and the Sahel, but decreased for the western, southern, and northern parts during the 21st century. An increase in annual mean surface temperature occurred in all regions of the African continent during the 21st century. Ranges of temperature increment are higher for dried subtropical regions than for moist tropics. Those future change patterns are qualitatively consistent with the average projection of the 21 GCMs used for the Fourth Assessment Report of the IPCC (Solomon et al. 2007), although the patterns of a projected annual precipitation in the Sahel differs among those GCMs.

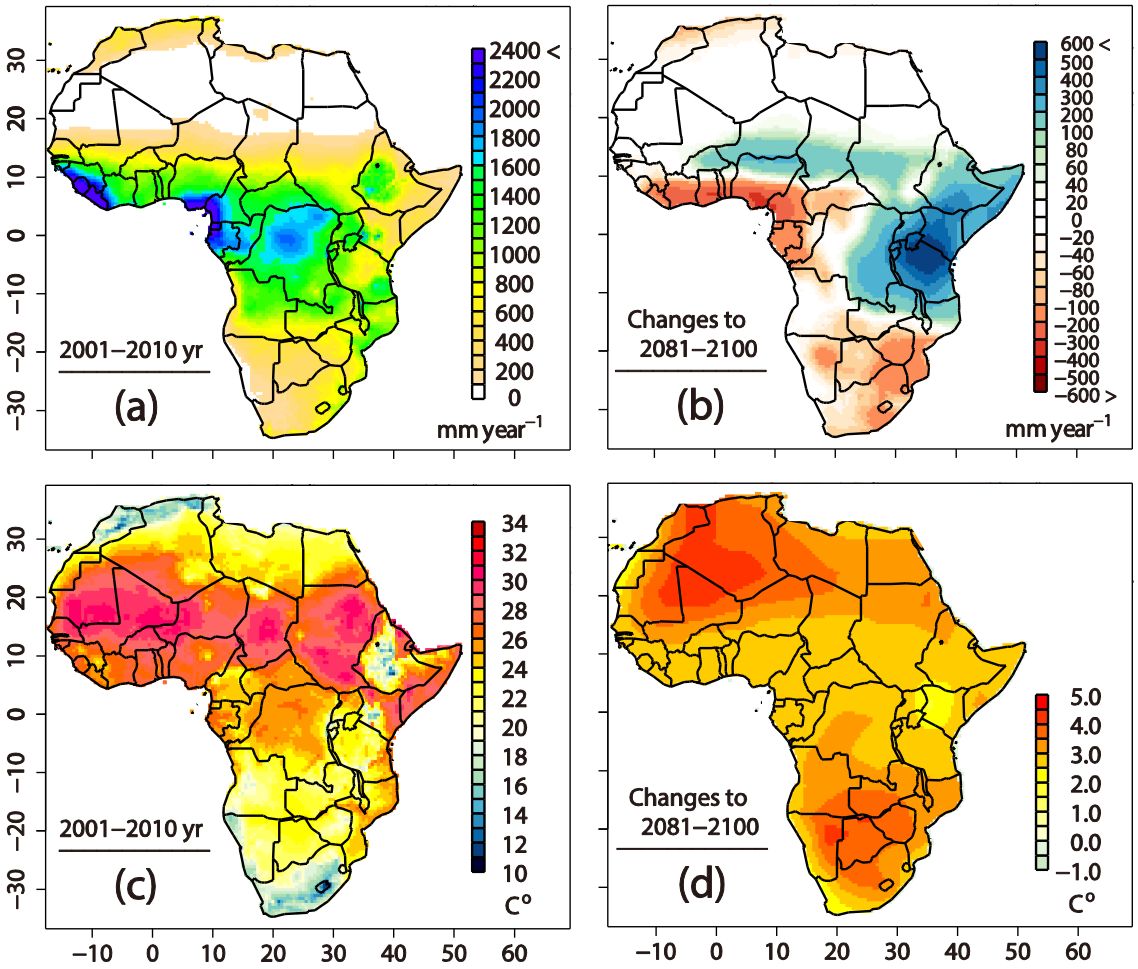

Fig. 4.1. Present climate data from CRU and its future change predected by MIROC-AGCM. (a) Annual precipitation and (c) annual mean surface temparature during 2001 -2010, and the changes of (b) annual precipitation and (d) annual mean surface temperature during 2001-2010 to 2081-2100.

4.2.6 Simulation Procedure

A 2000-years spin-up run from bare ground was conducted by repeatedly inputting the modified MIROC climate data and annual time-series of atmospheric CO_2 during the period 2001-2010. Wildfire occasionally occurs during the spin-up run, resulting in stochastic variability within the state after a spin-up run. For reducing this effect on the simulations, we prepared 10 initial states by appending 10 years simulations after the 1990-years spin-up by inputting climate and CO_2 data during 2001 to 2010. After the spin-up run, simulations for the 21st centuries from 10 initial states were conducted under each CO_2 concentration. In the future experiment, annual time-series of global mean atmospheric CO_2 of the SRES A1B emissions scenario during the period

2001-2100 was employed for the 21st century. In the suppressed CO_2 increment experiment, annual time-series of atmospheric CO_2 was employed during the period 2001-2010, and then the 362.9 ppm of atmospheric CO_2 which is the global mean in 2010 was employed after 2010. Here, the climatic variables (for example, precipitation, temperature, and so on) same as the future experiment were used for the suppressed CO_2 increment experiment.

4.2.7 Conversion from Carbon emission to Black Carbon emission

As the spatial resolution of original climate data of MIROC 3.2 was coarse (128×64 global points, which corresponds to approximately 2.8°×2.8° grid resolution), analysis at the resolution of the simulation (0.5°×0.5°) should contain much "noise". Thu, to extract meaningful trends, BC emissions from the SEIB-DGVM were converted to the spatial resolution of 5.0° × 5.0° by simply averaging over each grid cell domain.

Because SEIB-DGVM cannot output BC emission directly, we converted the carbon emissions into BC emission by using a ratio between BC and carbon emission (α) of Global Fire Emissions Data (GFED) version 3 (Giglio et al. 2010). Future BC emission during 2081-2100 in the African continent was calculated as following equation,

$$BC_{(2100-2081)} = BC_{GFED(2001-2010)} + \alpha\left(C_{SEIB(2081-2100)} - C_{SEIB(2001-2010)}\right). \quad (4.5)$$

where α is 1.00×10^{-3}, which is the aveage of 71 grid cells where the coverage of the land area in each grid cell domain (5.0° × 5.0°) is more than a quarter. The standard deviation of α was 0.04×10^{-3}. In order to reduce the influence of a difference of carbon emission between simulation and observation, we converted the difference of carbon emission between 2081-2100 and 2001-2010 into BC emission from wildfire.

4.3 Results

4.3.1 Control Experiment

First, we validated the results of the simulations under current climatic condition during 2001 to 2010. The model faily reconstructs the spatial distribution of BC emissions over the African continent (Fig. 4.2, r=0.83, P<0.001). The average BC emission of simulation was 5.4×10^{-2} g BC m^{-2} $year^{-1}$, while that of observation was 6.3×10^{-2} g BC m^{-2} $year^{-1}$ in the African continent; The Simulated BC emission was 1.16 times higher than the observed values.

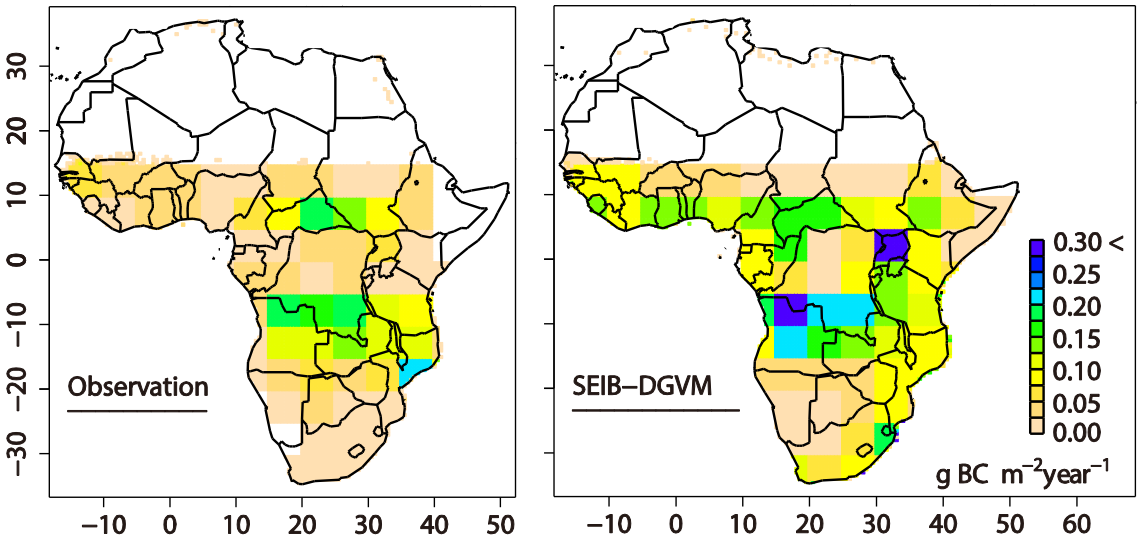

Fig. 4.2. Time average of annual BC emission from wildfire during 2001-2010: (right) average of 10 simulations by SEIB-DGVM and (left) GFED.

The average of 10 simulation of fire intervals for each virtual forest (spatial resolution: 0.5°×0.5°) during 2001 to 2010 in savanna region (8°N–13°N, 10°E–35°W and 20°S–10°S, 15°E–35°W) ranged from 2 to 16 years (Fig. 4.3). This range was consistent with the observed fire intervals of 1 to 12 years (Thonicke et al. 2001). The simulation was able to reproduce the low probability of fire in African central part (5°S–5°N, 10°E–30°E), which was consistent with satellite observation. Sato and Ise (2012) validated that the SEIB-DGVM fairly reproduces spatial distribution of biomass and net primary production (NPP) over the African continent under current climatic condition.

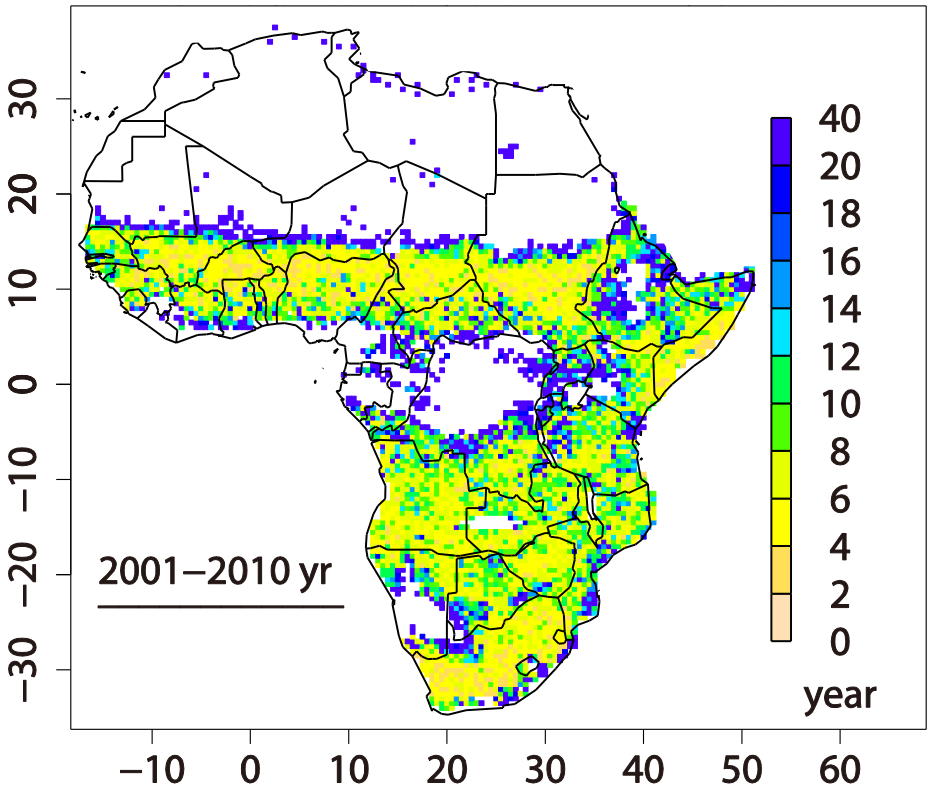

Fig. 4.3. Simulated time average of fire intervals for each virtual forest during 2001-2010.

4.3.2 Future Experiment

Figure 4.4 shows the change in BC emission, and figure 4.5 shows changes in biomass, NPP, tree coverage, and fire frequency over the African continent during the 21st century (i.e., averages value during 2081-2100 was subtracted by the average value of 2001-2010). Table 4.1 summarizes these changes.

The change of annual BC emissions was +30.5% over the African continent. This increase of BC emission was more apparent for the northern hemisphere than for the southern hemisphere; they were +40.4% and +16.7%, respectively. Biomass increased by 33.6±1.3% (± standard deviation) over the African continent. In correspondence with the changes in BC emission, this increment was more apparent for the northern hemisphere (+39.8±1.4%) than for the southern hemisphere (+26.0±1.9%). The changes of NPP and fire frequency was +8.3±0.3% and −7.4±0.7%, respectively, over the African continent.

As was seen before, there was apparent spatial-heterogeneity for these changes.

Therefore, for enabling region specific analysis, we defined following four regions, where intensive changes of BC emissions occurred: (1) the western Africa (5°N–10°N, 15°W–0°W); (2) the central Africa and the western coast of Africa (5°S–10°N, 0°W–20°E); (3) the eastern Africa (10°S–10°N, 20°E–50°E); and (4) the southern Africa (25°S–15°S, 20°E–35°E). The BC emission increased in the regions 1, 2, and 3, while it decreased in the region 4.

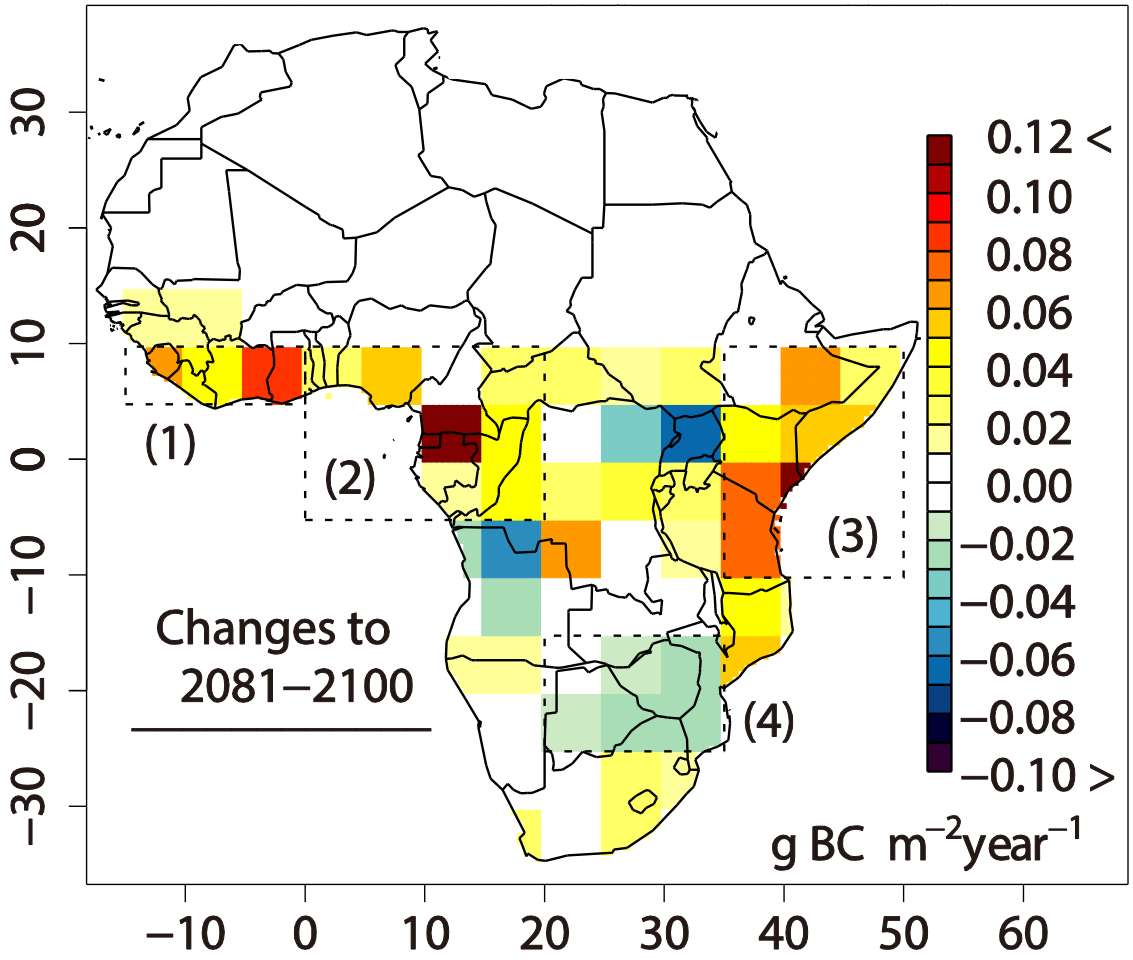

Fig. 4.4. Change of annual BC emission of wildfire from 2001-2010 to 2081-2100. Four regions where there was a characteristic change of BC emission are indicated by broken line squares.

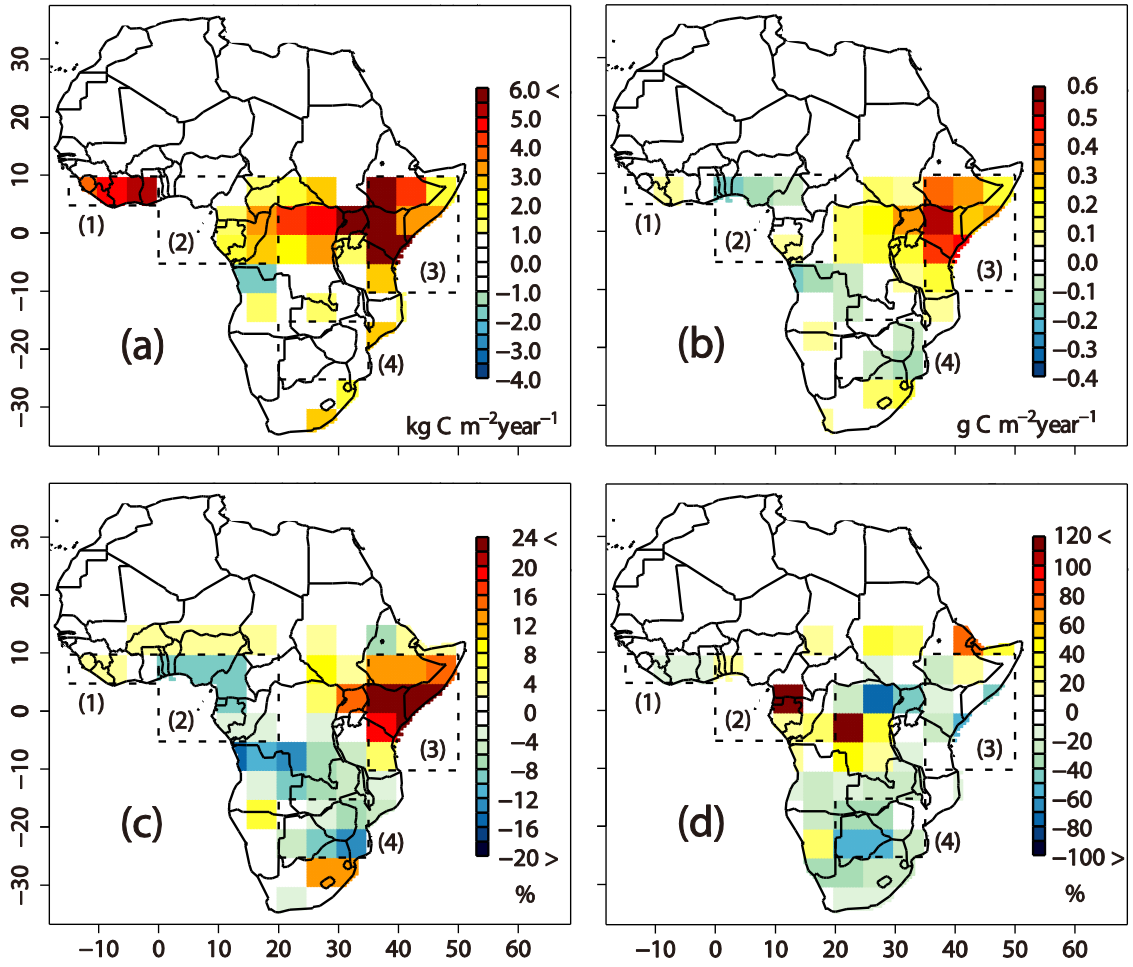

Fig. 4.5. The difference of (a) biomass, (b) NPP, and (c) tree coverage in 2081-2100 from 2001-2010 years. (b) The change ratio of fire frequency in 2081-2100 from that in 2001-2010.

Table 4.1. Changes in BC, biomass, NPP, tree coverage, and fire frequency of each region in the future experiment during the 21st century. Numbers for regions refer to the Fig. 4.4, 4.5.

Area	BC (g BC m^{-2} yr^{-1})	Biomass (kg C m^{-2} yr^{-1})	NPP (g C m^{-2} yr^{-1})	Tree Coverage (% yr^{-1})	Fire Frequency (% yr^{-1})
African continent	+0.014	+1.6	+0.05	+0.3	−7.4
Northern Hemisphere	+0.017	+2.1	+0.06	+2.8	+2.1
Southern Hemisphere	+0.011	+1.2	+0.04	−2.0	−17.0
Region 1	+0.057	+4.3	+0.01	+1.6	−8.6
Region 2	+0.019	+0.7	−0.01	−1.3	+12.5
Region 3	+0.047	+4.6	+0.32	+16.1	−13.1
Region 4	−0.015	+0.6	−0.06	−6.8	−34.2

4.3.3 Suppressed CO_2 increment Experiment

Figure 4.6 shows the changes in BC emission, and figure 4.7 shows changes in biomass, NPP, tree coverage, and fire frequency over the African continent during the 21st century. Table 4.2 summarizes these changes.

The change of annual BC emissions was +32.5% over the African continent. This increase of BC emissions was −29.9% in the northern hemisphere and −35.1% in the southern hemisphere. Biomass increased by 2.6±1.5% over the African continent. This change ratio of biomass was +1.7±1.3% in the northern hemisphere and −7.2±2.0% in the southern hemisphere. The range of increase in biomass under the suppressed CO_2 increment experiment was very small compared to that of the future experiment (Fig. 4.8). The changes of NPP, fire frequency, and tree coverage were −17.4±0.2%, −7.8±0.7%, and −14.1±0.6%, respectively, over the African continent.

There was apparent spatial-heterogeneity for these changes. We defined following

three regions, where intensive changes of BC emissions occurred: (5) the near-equatorial Africa (10°S–10°N, 15°W–25°E); (6) the northeastern Africa (5°S–10°N, 35°E–50°E); and (7) the southern Africa (35°S–10°S, 10°E–40°E). The annual BC emission increased very little in the regions 5 and 6, while it decreased in the region 7. In the region 7, in correspondence with the decrease in BC emission, biomass decreased by −4.2±3.7%.

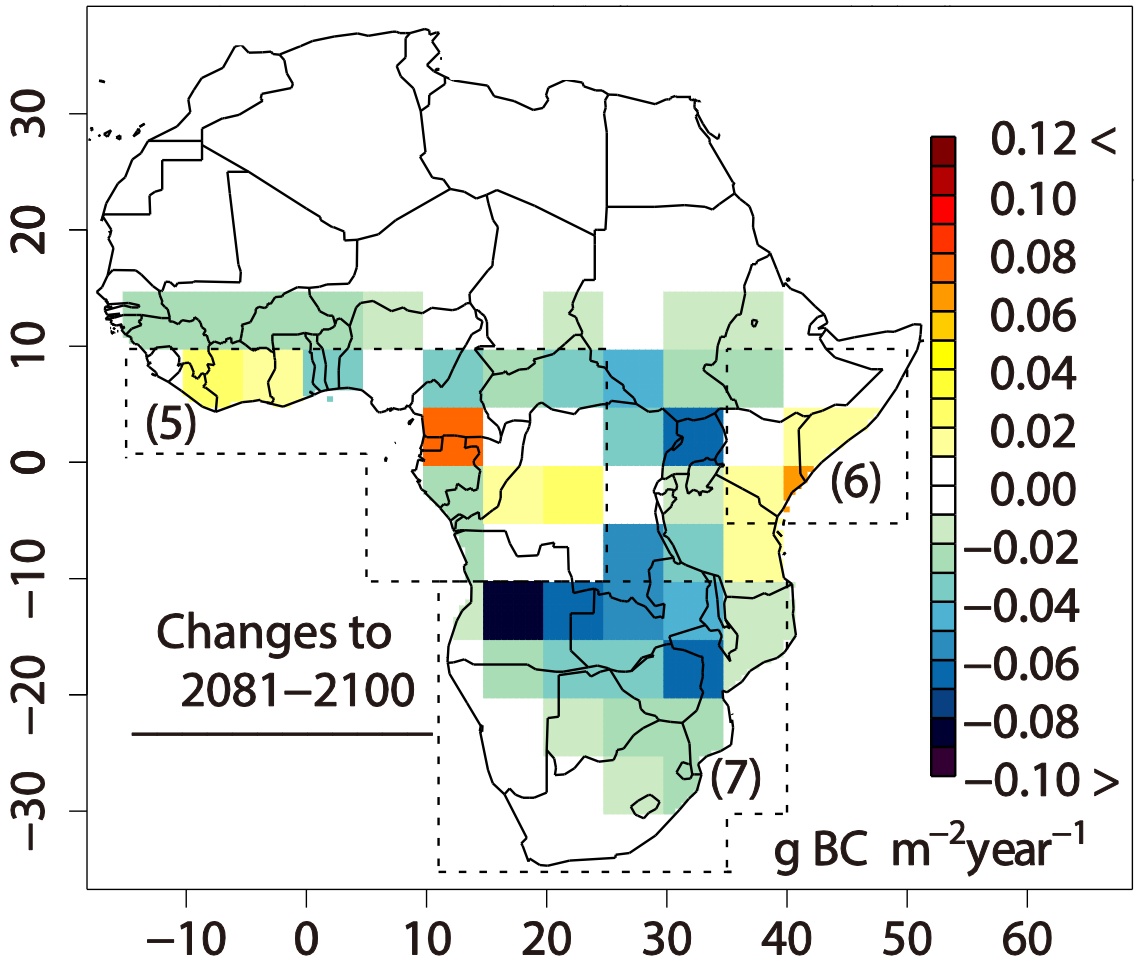

Fig. 4.6. Change of annual BC emission from 2001-2010 to 2081-2100 in the suppressed CO_2 increment experiment. Three regions where there was a characteristic change of BC emission are surrounded with broken lines.

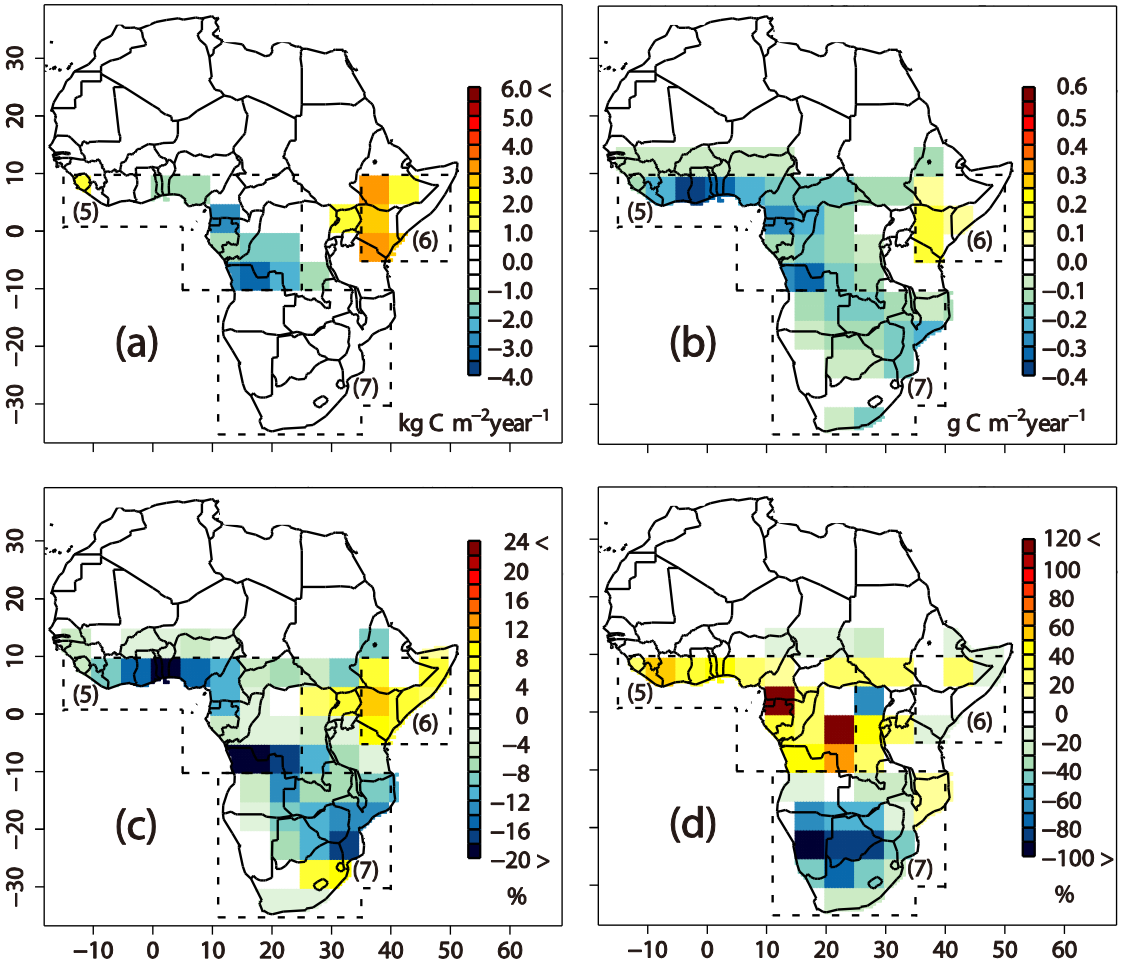

Fig. 4.7. Same as Fig. 4.5 but by the suppressed CO_2 increment experiment.

Table 4.2. Changes in BC, biomass, NPP, tree coverage, and fire frequency of each region in the future experiment during the 21st century under suppressed CO_2 increment. Numbers for regions refer to the Fig. 6.

Area	BC (g BC m^{-2} yr^{-1})	Biomass (kg C m^{-2} yr^{-1})	NPP (g C m^{-2} yr^{-1})	Tree Coverage (% yr^{-1})	Fire Frequency (% yr^{-1})
African continent	−0.018	−0.1	−0.10	−4.8	−7.8
Northern Hemisphere	−0.012	+0.1	−0.10	−3.5	+4.5
Southern Hemisphere	−0.023	−0.3	−0.09	−6.1	−20.2
Region 5	−0.008	−1.0	−0.21	−9.3	+30.8
Region 6	+0.003	+1.9	+0.08	+6.1	−1.5
Region 7	−0.026	−0.1	−0.10	−6.0	−33.3

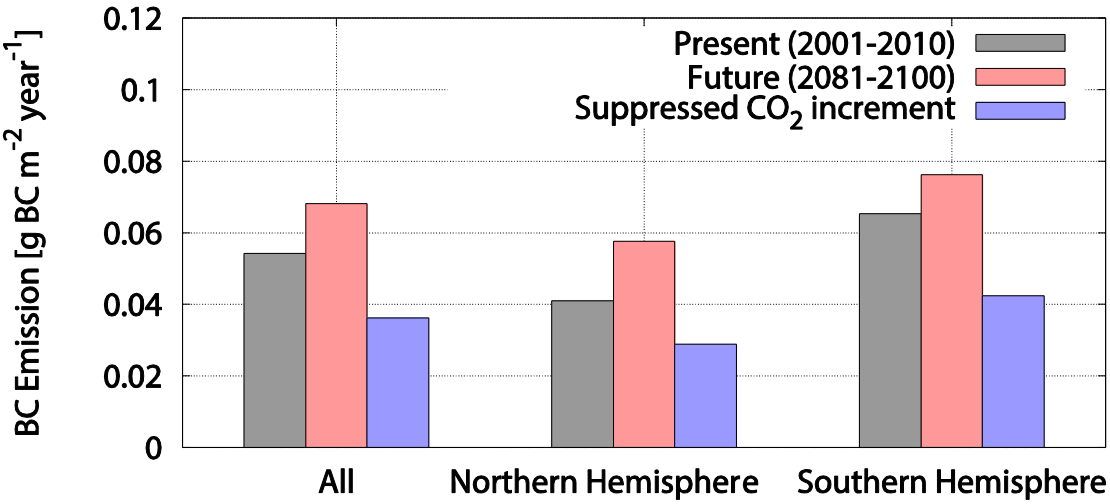

Fig. 4.8. Annual BC emission from wildfire. Gray: present (2001-2010), vermilion: future (2081-2100) and blue: future by suppressed CO_2 increment experiment. All indicate the African continent.

4.4 Discussions

4.4.1 Control Experiment

Simulated BC emission under current climatic condition (i.e., years of 2001 to 2010) was a little larger than those of observation. We consider this overestimation was caused by the overestimation of vegetation biomass, which would be caused by the fact that the SEIB-DGVM does not consider human land-usage such as deforestation. The overestimation of biomass was also occurred in the previous study with the SEIB-DGVM in the African continent (Sato and Ise 2012).

This overestimation of BC is conspicuous in Angola (15°S–5°S, 10°E–25°E), east Sahel of Africa (5°S–15°N, 30°E–45°E), Tanzania (10°S–0°S, 35°E–40°E), and the coast of gulf of Guinea (5°N–10°N, 15°W–10°E). All of these regions are significantly deforested through logging and slash-and-burn agriculture before 2005.

In Angola, the deforestation rate was 11.0%, and bare soil and farmland increased by 6.9% during 1990-2005 due to decrease in a savanna-woodland and grassland (Cabral et al. 2010). In east Sahel of Africa (Ethiopia, Kenya, Somalia, Sudan, Uganda, and Djibouti), Barbier (2001) showed forest area decreased by 9 % and this was found by FAO data (FAO 1993). FAO (2005) showed forest area decreased by 27.1% during 1990-2005 in Uganda (0°N–5°N, 30°E–35°E). Refer to the subsection 3.4.1 for the situation of the coast of gulf of Guinea and Tanzania.

4.4.2 NPP and Biomass of the Future Experiments

The annual NPP and biomass showed an increase trends in the future experiment. However, it showed a decrease trend under the suppressed CO_2 increment experiment during 21st century. Those results indicate that the enhanced annual NPP and biomass were primary caused by increase of atmospheric CO_2 concentration. This result would be associated with the fact that higher atmospheric CO_2 increase photosynthesis efficiency by fertilization effect and higher water-use efficiency (Larcher 1995). This tendency of carbon storage is consistent with previous studies. Scheiter and Higgins (2009) showed amount of African biomass was projected to nearly double during the 21st century under the IPCC (2007) SRES A1B scenario. As well, Joos et al. (2001)

found an increase in terrestrial carbon storage of Africa during the 21st under the A1B scenario, but the carbon storage decrease when CO_2 fertilization was suppressed.

4.4.3 BC emission of the Future Experiments

In the future experiment, the increased BC emission in the African continent associated with the increased biomass as fuel load due to the enhanced atmospheric CO_2 concentration. On the other hand, the spatial distribution of change in BC emission pattern was very sensitive to change in annual precipitation pattern rather than annual mean temperature pattern. We converted the spatial resolution of NPP, biomass, annual precipitation, and annual mean temperature to a 5.0°×5.0° grid resolution by simple averaging over each grid cell domain, and calculated the change in those values from 2001-2010 to 2081-2100. Those values were normalized, and then the spatial correlations coefficients of NPP-precipitation, NPP-temperature, biomass-precipitation, and biomass-temperature were calculated. Result of this analysis showed that the changes in NPP and biomass were under strong control of annual precipitation; the spatial correlation coefficients of NPP-precipitation and biomass-precipitation were 0.69 ($P < 0.001$) and 0.40 ($P < 0.001$), respectively. On the other hand, the spatial correlation coefficients of NPP-temperature and biomass- temperature were negative and weaker; they were −0.21 ($P < 0.05$) and −0.30 ($P < 0.01$), respectively. Because BC emission was affected significantly by change in biomass and NPP, the spatial distribution of change in BC emission pattern was also controlled by change in precipitation pattern. Actually, remote-sensing studies of the Sahel area showed that inter-annual variations in indices of vegetation greenness such as NDVI (Normalized Difference Vegetation Index) and LAI (leaf area index) are primarily controlled by precipitation (Anyamba and Tucker 2005; Hickler et al. 2005). The results of field studies have suggested that precipitation primarily determines production and plant-species composition in African vegetation (Lwanga 2003; Gonzalez 2001; MacGregor and O'Connor 2002).

In the future experiment, there is an increasing trend in the amount of BC emission in both hemispheres. However, the causes of this change in BC emission would be different among regions and hemispheres. We categorized the causes into three types. First, in the eastern Africa (1) and southern Africa (3), the BC emission was increased due to the increase in biomass as fuel load for wildfire (Fig. 4.5a). This increase in biomass was caused by an increment of atmospheric CO_2 concentration in the eastern Africa (1), and it caused by an atmospheric CO_2 concentration and annual precipitation

in southern Africa (3) (Fig. 4.5a, Fig. 4.7a). Second, in the central and western coast of Africa (2), the BC emission was increased due to the increase in biomass and fire frequency (Fig. 4.5a, d). The increase in biomass as carbon storage also was caused by an increment of atmospheric CO_2 concentration. On the other hand, the fire frequency increased due to the decrease in annual precipitation which dry out fuel load (Fig. 4.1b) and the decrease in tree cover (i.e., the proportion of tree canopy coverage in the stand) (Fig. 4.5c). Tree cover decreased because the reduction of annual precipitation leads to higher tree mortality due to water stress. Third, in the southern Africa (4), annual NPP increased due to the increment of CO_2 concentration, but an increase rate of NPP was low because annual precipitation decreased, so that there is little change in biomass. This low production rate of fuel load was hard to satisfy the required conditions of occurrence of wildfire. Consequently, the fire frequency decreased (Fig. 4.5d) and BC emission slightly decreased (Fig. 4.4).

4.5 Summary

We simulated how BC emission from wildfire changes during the 21st century in the African continent (37°S–34°N, 17°W–59°E) with a dynamic vegetation model SEIB-DGVM employing forecasted climatic condition under the SRES A1B CO_2 emission scenario with an AGCM MIROC3.2. Simulations were conducted under two conditions. First one is the future experiment: both climate and atmospheric CO_2 concentration develops during the 21st century. Second one is the suppressed CO_2 increment experiment: only climatic condition develops, while atmospheric CO_2 concentration stays at the same level of the year of 2010.

Simulation under current climatic condition fairly reconstructed the observed geographical-distribution of annual BC emission. In the future experiment, the average annual BC emission, biomass, and fire frequency over the Africa changed by +30.5%, +33.6%, and −7.4%, respectively, during the 21st century. For both increments of BC emission and biomass, the northern hemisphere were more responsible than for the southern hemisphere. On the other hand, in the suppressed CO_2 increment experiment, the average annual BC emission, biomass, and fire frequency changed by −32.5%, −2.6%, and −7.8%, respectively. These results indicated that BC emission would be caused by the increased biomass, which functions as fuel load. As the increment of atmospheric CO_2 concentration is responsible for the biomass increment, CO_2 emission scenario would largely control the amount of BC emission over the African continent in future.

As well, for forecasting geographical distribution of BC emission over the African continent, precise forecasting for annual precipitation is important. This is because, geographical destribution of changes in NPP and biomass are more tightly correlated with changes in annual precipitation than with changes in annual mean temperature. This study assumed that changes in BC emission does not affect climate, although previous studies showed that the atmospheric BC caused a decreasing trend of precipitation over tropical Africa during the 20th century. In the future studies, such feedback of BC emission to the climatic conditions would be also studied for more precise forecast of BC emission.

Chapter 5

Conclusions

First, we studied the factors contributing to the variance of geographical distribution patterns of BC emissions. The response pattern of vegetation productivity to climate variables explained 57.5% of the regional variability in BC emissions during the growing season. This vegetation productivity was more closely correlated with the geographical distribution patterns of BC emission than climate variables such as temperature during the dry season. The response pattern of vegetation productivity to climate during the vegetation growing season was roughly determined by vegetation parameters such as biome type and tree cover, which are heterogeneously distributed in Africa. Therefore, regional BC emission patterns would differ even if climate change occurred uniformly throughout semi-arid Africa.

Second, we studied the relationship between wildfire carbon emissions and cyclic variations in precipitation and temperature over Africa. We simulated carbon emissions from wildfires over the African continent using a SEIB-DGVM under the following climatic forcing conditions: (1) a control condition using observation-based climatic data (i.e., the control experiment); (2) negligible inter-annual variation in annual precipitation or annual mean air temperature (i.e., the no-cycle experiment); and (3) cyclic inter-annual variability in precipitation or air temperature at a frequency of 20, 10, and 6 years (i.e., the cycle experiment). In the no-cycle experiment for precipitation and temperature, carbon emissions in the northern hemisphere decreased by 15.4% and 15.1%, respectively, compared with emissions in the control experiment, whereas there was little difference in the southern hemisphere. In the cycle experiment for precipitation, carbonaceous aerosol emissions increased in the northern hemisphere when the cycle of precipitation exhibited less fluctuation. However, in the cycle

experiment for temperature, carbonaceous aerosol emissions did not significantly vary with fluctuations in the cycle. Therefore, our simulation revealed the importance of the pattern of inter-annual variability in precipitation to regulating carbonaceous aerosol emissions in the African continent.

Finally, we estimated BC emission from wildfire in the future with a dynamic vegetation model SEIB-DGVM employing forecasted climatic condition under the SRES A1B CO_2 emission scenario with an AGCM MIROC3.2, and then analyzed the cause of changes in the spatial distribution of BC emission. The average annual BC emission over the Africa changed by +30.5% during the 21st century. Range of the increment of BC emission was higher for northern hemisphere (40.4%) than for southern hemisphere (16.7 %) of the African continent. Biomass increased by 33.6% over the African continent. In correspondence with the changes in BC emission, this increment was more apparent for the northern hemisphere (+39.8%) than for the southern hemisphere (+26.0%). Those results of the increased BC emission and biomass suggest that simulated increment of BC emission is caused by the increment of biomass as fuel load for fire, which is a result of higher atmospheric CO_2 concentration under future environment. It is also shown that the change of geographical distribution of BC emissions is caused by the change of annual precipitation pattern because the spatial destribution of change in NPP and biomass pattern were very sensitive to change in annual precipitation pattern.

In the future, BC emission increased and it was sensitive to an atmospheric CO_2 concentration in the African continent. The spatial distribution of change in future BC emission pattern was controlled according to the change in future annual precipitation pattern. In addition, the spatial distribution of BC change was also affected by not only the pattern of inter-annual variability in precipitation, but also spatial distribution patterns of biome type and tree cover which correlate with vegetation productivity and fire probability. Furthermore, it is necessary to estimete the influence of this increment of atomosphric BC on climate system (for example, radiation forcing) because it caused a decreasing trend of precipitation in tropical Africa during the twentieth century.

6. Appendixes

A. Satellite Observation of BC Emission

In the Global Fire Emissions Database (GFED) version 3, BC emissions were estimated by computing three variables: burnt area, dry matter, and the BC emission factor, which depends on the biome type. First, the burnt area $A(i,t)$ in each 0.5° × 0.5° grid cell was estimated using a non-linear function of the number of active fires in a month, $N_f(i,t)$, as

$$A(i,t) = \alpha(i)\, N_f(i,t)^{\beta(i)}\,, \tag{A1}$$

where i is the grid cell, t is the month, and $\alpha(i) \geq 0$, $\beta(i) \geq 0$ (Giglio et al. 2010). The parameters α and β were estimated independently in each grid cell. Second, the dry matter mass was estimated from the living biomass pool size by use of the allocation scheme (Hui and Jakson 2006), which was derived from the net primary productivity (NPP). The NPP was derived from satellite remote sensing data by

$$\mathrm{NPP}(i,t) = \mathrm{fAPAR}(i,t) \times \mathrm{PAR}(i,t) \times \varepsilon(T,P)\,, \tag{A2}$$

where $\mathrm{PAR}(i,t)$ is the photosynthetically active radiation, $\mathrm{fAPAR}(i,t)$ is the fraction of available photosynthetically active radiation absorbed by vegetation, $\varepsilon(T,P)$ is the maximum light use efficiency, T is temperature, and P is moisture. Third, the BC emission was computed by multiplying the dry matter mass burned, which was derived from Eq. (A1) and the dry matter, by its emission factor (g BC / kg dry matter mass burned), which depends on the biome (van der Werf et al. 2010). The results of a Monte Carlo simulation indicated that globally, uncertainties were around 20% (1σ) for annual BC estimates during 2001–2009. The uncertainties for Africa (both northern and southern hemisphere regions) were of the same magnitude (van der Werf et al. 2010).

B. Fire Sub-model

The fire sub-model in aDGVM (Scheiter and Higgins 2009) was introduced into SEIB-DGVM. This fire model is a semi-empirical model based on a study of the savanna in southern Africa. Fire only occurs when the stand average potential energy intensity ($ifire$ in J s^{-1} m^{-1}) exceeds a threshold value, which is estimated as a function of the fuel load ($fuel$), fuel moisture (θ), and wind speed ($wind$).

$$ifire(fuel, \theta, wind) = 16890 \times \left(fuel \frac{fuel}{fuel + 119.7}\right) \times \left(\frac{301 \times \arctan(wind)}{2.6 \times 10^3 \times \theta + 1.61 \times 10^5 (1 - \theta)}\right), \quad \text{(B1)}$$

where 16890 (in J g^{-1}) is the heat yield when fuel is consumed, 119.7 and 301 are constants, 2.6×10^3 J g^{-1} is the pre-ignition heat of moisture, and 1.61×10^5 J g^{-1} is the pre-ignition heat of fuel. The term in the first set of brackets is the weight of fuel consumed (in g DM m^{-2}), and the term in the second set of brackets is the rate of fire spread (m s^{-1}). Fire can occur when the stand average of $ifire$ exceeds a minimum intensity of 300 kJ s^{-1} m^{-1} (van Wilgen and Scholes 1997).

Fuel load ($fuel$) is calculated using the total amount of living (moist) fuel ($fuel_{living}$) and dead (dry) fuel ($fuel_{dead}$). The value of $fuel_{living}$ is estimated from the aboveground grass biomass ($gmass_{leaf}$) and one-half of the standing dead mass of grass ($fuel_{SDG}$), as shown in equation (B2). $fuel_{dead}$ is estimated from the lying dead mass ($fuel_{living}$), and one-half of $fuel_{SDG}$ as shown in equation (B3).

$$fuel_{living} = gmass_{leaf} + 0.5 \times fuel_{SDG}. \quad \text{(B2)}$$

$$fuel_{dead} = fuel_{lying} + 0.5 \times fuel_{SDG}. \quad \text{(B3)}$$

The moisture content of the living fuel is assumed to be equal to the relative air humidity (rh). The moisture content of dead fuel decreases by an exponential function and is assumed to tend toward 0% (Higgins et al. 2000). The average fuel moisture (θ) is estimated as follows:

$$\theta = rh \times \frac{fuel_{living}}{fuel_{living} + fuel_{dead}}. \quad \text{(B4)}$$

If the stand average of the $fuel$ exceeds 300 kJ s^{-1} m^{-1}, the daily probability of fire (F_{prob}) is 0.0015% when the fraction of the tree canopy coverage of the stand (TC: 0–100%) is 0.0 (Scheiter and Higgins 2009), and F_{prob} decreases as TC increases. Additionally, when TC is 40–65% or >65%, F_{prob} is reduced by 80% or 100%, respectively (Archibald et al. 2009).

Because the burning rate is diminished at high altitudes where atmospheric pressure is low (Wieser et al. 1996), F_{prob} is reduced as altitude increases by the use of terms for fire frequency (Along Track Scanning Radiometer (ASTR-2) during 1997–2009) and altitude (Global Soil Wetness Project (GSWP-2)) (Dirmeyer et al. 2002). The number of fire occurrences (in N $year^{-1}$) was calculated for each grid cell (0.5° × 0.5°), and then the 10% of grid cells with the most frequent occurrence of fire over Ethiopia (4°N–15°N, 33°E–42°E) and the 5% of grid cells with the most frequent occurrence of fire over Africa (except Ethiopia) were selected. We applied a regression analysis with a quadratic function to the fire frequency (ff) as the dependent variable and altitude (ALT) as the independent variable in each selected grid cell. The regression formula for Ethiopia was $ff = 4.9 + 4.2 \times 10^{-2} \times ALT - 1.9 \times 10^{-5} \times ALT^2$ and for other regions was $ff = 9.9 + 1.6 \times 10^{-2} \times ALT - 9.8 \times 10^{-6} \times ALT^2$. We set the value to 1.0 if ff was larger than 1.0 and 0.0 if ff was smaller than 0.0 (i.e., ff cannot have a minus value). For the grid cells with a higher altitude than the altitude of the maximum value of ff (i.e., 1102 m for Ethiopia and 807 m for other regions), F_{prob} was reduced by multiplication with the changed fire frequency formula (ff_c). This conversion was applied to the grid cells at a TC range of 0–40%. For the grid cells at a TC range of 40–65%, we used a minimum value of F_{prob} that was reduced by 80% (i.e., F_{prob} = 0.0003) and set using a quadratic function of altitude (i.e., $F_{prob} = 0.015(0.1 - 0.0833 \times T_c) \times ff_c$).

All of the aboveground biomass of grass, standing dead mass of grass and tree leaves, lying dead mass, and half of the trunk litter is consumed when fire occurs. Grass species become dormant, and trees are burned when fire occurs. This burned tree mortality due to wildfire is an empirically derived function of tree $height$ (m) and $ifire$ (Higgins et al. 2000).

$$mort_{fire}(height, ifire) = \frac{\exp\left[d_1 - d_2 \ln(height) + d_3\sqrt{ifire}\right]}{1 + \exp\left[d_1 - d_2 \ln(height) + d_3\sqrt{ifire}\right]}, \quad \text{(B6)}$$

here, the coefficients d_1, d_2, and d_3 are 4.3, 5.003, and 0.004408, respectively.

C. Climate Data for Simulation

The African continent was divided into 0.5° × 0.5° grid cells in this simulation. SEIB-DGVM needs daily climatic variables: air temperature, soil temperature (at depths of 0–10 cm, 10–200 cm, and 300 cm), precipitation, total cloudiness, wind velocity, and specific humidity. We used the National Centers for Environmental Prediction/National Center for Atmospheric Research (NCEP/NCAR) daily climate data for the period of 1982–2009 (Kalnay et al. 1996). Because the spatial resolution of the NCEP/NCAR data was 192 × 94 global points, these data were linearly interpolated to a 0.5° grid mesh, which corresponds to the spatial resolution in our simulation. We corrected this interpolated NCEP/NCAR data using the Climate Research Unit (CRU) observation-based climatic data [CRU-TS 3.0 (0.5 Degree) 1901–2009 Monthly Climate Time Series (Mitchell and Jones, 2005)] as follows. The air temperature was linearly scaled by adding a constant (month and location specific) so that the monthly mean was the same as the value for the corresponding month and location in the CRU data. The soil temperature was linearly scaled by adding a constant (year and location specific) so that the annual mean was the same as the air temperature for the corresponding year and location of the CRU data. We then substituted air temperature for soil temperature because the CRU data do not contain soil temperature. The daily precipitation and specific humidity were linearly scaled by multiplying a constant (month and location specific) so that the monthly means were the same as the values for the corresponding month of the CRU data. The interpolated NCEP/NCAR daily wind and cloudiness data were used for simulations. The annual global mean atmospheric concentrations of CO_2 from 1982 to 2009 were used in the simulations.

D. Climate Data for the Cycle Experiments

For the no-cycle experiments, we created new climate data sets to estimate the effects of carbon emissions from wildfires on the small inter-annual variation in annual precipitation and annual mean air temperature over the 20-year period. The new climate data sets were close to the average observed annual precipitation or annual mean temperature for 28 years (1982–2009), and inter-annual variation was adjusted to be below one-tenth of the standard deviation of the average values over 28 years (1982–2009). We created 10 members of these climate data sets for the 20-year period by adjusting precipitation (P_{new20}) or temperature (T_{new20}). First, daily corrected NCEP/NCAR reanalysis data were separated into 24 groups by half-monthly intervals (e.g., the first group was 1–15 January for each year from 1982 to 2009, and the second group was 16–31 January for each year from 1982 to 2009). Each group contained from 392 days (i.e., 28 (years) × 14 (days)) to 448 days (i.e., 28 (years) × 16 (days)) of climate data. There was no way of obtaining day and year within each group of daily data. Next, for each group, classified climate data were selected at random to form the days of half a month, and then the selected climate data were combined with other selected climate data. In this way, we obtained the climate data for half-month periods. A new climate dataset (D_{new}) for one year was obtained by placing all of the groups of half-monthly climate data in order of bimonthly time. Subsequently, we determined whether to adopt this D_{new}. The decision criterion to adopt the D_{new} was that annual precipitation (P_{new}) should fall within the range $\bar{P} - 0.1\sigma_P \le P_{\mathrm{new}} \le \bar{P} + 0.1\sigma_P$ or the annual mean temperature (T_{new}) should fall within the range $\bar{T} - 0.1\sigma_T \le T_{\mathrm{new}} \le \bar{T} + 0.1\sigma_T$. Here, $\bar{P}$ and σ_P are the average and standard deviation of annual precipitation (Fig. 3.1a, b) and $\bar{T}$ and σ_T are the average and standard deviation of annual mean air temperature (Fig. 3.1c, d) of the CRU data from 1982 to 2009. We conducted the same step described above repeatedly and got 20 D_{new} datasets. Climate datasets for 20 years of P_{new20} and T_{new20} were obtained by concatenating those 20 D_{new} datasets at random, which satisfied the decision criterion for precipitation and temperature, respectively. The 10 climate data sets were created by repeating the above process.

The climate datasets for the precipitation cycle experiments ($P_{cycle20}$) and temperature cycle experiments ($T_{cycle20}$), in which only annual precipitation or only annual mean temperature changed periodically through the 20-year period and a maximum amplitude of $2.0\sigma_{P\ \mathrm{or}\ T}$, were created using the following equation:

$$P_{cycle20} = P_{new20} \frac{\bar{P} \pm 2\sigma_P \sin\left(\frac{2\pi}{l}x\right)}{\bar{P}}, \quad \text{(D1)}$$

$$T_{cycle20} = T_{new20} \pm 2\sigma_T \sin\left(\frac{2\pi}{l}x\right), \quad \text{(D2)}$$

where, l is 20, 10, and 6 which correspond to 20, 10, and 6 year cycle, respectively. x indicates simulation year (=1, 2, 3, …, 20). The maximum amplitude was adjusted 2.0 $\sigma_{P \text{ or } T}$ to include heavy rain and drought in climate data. On the other hand, the climate data sets of 6-year cycle-experiment were created for 18 years, in order to adjust the same time average of annual precipitation or annual mean temperature for whole experimental period as that of other cycle-experiments. A positive / negative sign in equations (D1) and (D2) indicate annual precipitation and annual mean temperature increase / decrease in early half of cycle, and then those variable decrease / increase in latter half of cycle. We described this different of phase as phase (±) in this study. The 10 climate data sets for 20 years were created for each phase and each cycle (i.e., 20, 10, and 6-year cycle). For precipitation, the daily climate data set for 20 years which annual precipitation change periodically was created by multiply a daily precipitation of P_{new20} by the ratio of annual precipitation data that change periodically ($P_{cycle20}$) to small inter-annual variation in annual precipitation (P_{new20}) for each year ($P_{cycle20}/P_{new20}$). However, the climate data does not change except daily precipitation. For temperature, the daily climate data set for 20 years which annual mean temperature change periodically was created by adding the difference between annual mean temperature data that change periodically ($T_{cycle20}$) and little inter-annual variation in annual mean temperature (T_{new20}) for each year ($T_{cycle20} - T_{new20}$) to a daily mean temperature of T_{new20}. However, the climate data does not change except daily temperature.

where l is 20, 10, or 6, corresponding to the 20-, 10-, and 6-year cycles, respectively, and x is the year of simulation (= 1, 2, 3, …, 20). The maximum amplitude was adjusted to 2.0 $\sigma_{P \text{ or } T}$ to include heavy rain and drought in the climate data. However, the climate data sets of the 6-year cycle experiment were created for an 18-year period in order to adjust the average annual precipitation or annual mean temperature for the whole experimental period to the same time period as the other cycle experiments. A positive / negative sign in equations (D1) and (D2) indicates an increase / decrease in the annual precipitation and annual mean temperature in the first half of the cycle, and those variables then decrease / increase in the second half of the cycle. We referred to this

difference in the phase as phase (±) in this study. The 10 climate data sets for the 20 years were created for each phase and each cycle (i.e., 20-, 10-, and 6-year cycles). For precipitation, the daily climate data set for 20 years in which annual precipitation changed periodically was created by multiplying the daily precipitation of P_{new20} by the ratio of the annual precipitation data that changed periodically ($P_{cycle20}$) to the small inter-annual variation in annual precipitation (P_{new20}) for each year ($P_{cycle20}/P_{new20}$). However, the climate data did not change, with the exception of daily precipitation. For temperature, a daily climate dataset for 20 years, in which the annual mean temperature changed periodically, was created by adding the difference between annual mean temperature data that changed periodically ($T_{cycle20}$) and the small inter-annual variation in annual mean temperature (T_{new20}) for each year ($T_{cycle20} - T_{new20}$), to the daily mean temperature of T_{new20}. However, the climate data did not change, with the exception of daily temperature.

E. Skill Score

To validate the spatial distribution of carbon emissions, biomass, and tree cover for simulations, we introduced the skill score (SS) proposed by Taylor (2001). This index has been widely used to evaluate the spatial distribution patterns produced by climate models. SS is defined as follows:

$$SS = \frac{4(1+R)}{(SDR + 1/SDR)^2(1+R_0)}. \quad \text{(E1)}$$

Here, R is the spatial correlation coefficient between observations and the simulation. SDR is the spatial standard deviation of the simulation divided by that of the observation. R_0 means the maximum correlation attainable, and we assumed $R_0 = 1$. SS can be used to evaluate both the spatial correlation coefficient and the spatial standard deviation. The spatial distribution pattern of simulation results is completely in accord with that of the observation when the SS approaches 1.0.

F. Stomatal Conductance

The daily averages of photosynthetic rates (p_{ave} in μ mol CO_2 m^{-2} s^{-1}) was calculated for each plant functional type (PFT) was calculated for each PFT of each scale of one of to ten relative PAR intensity (10%, 20 %, …, 100% relative PAR to top pf the forest canopy of day), using Eq. (F1)

$$p_{ave} = \frac{p_{sat} \times lue \times \chi}{p_{sat} + lue \times \chi}, \tag{F1}$$

where p_{sat} (μ mol CO_2 m^{-2} s^{-1}) is single-leaf photosynthetic rate under light saturation. χ (μ mol photon m^{-2} s^{-1}) is the daily average of PAR receiving for grass layer (for grass PFTs) of for foliage of each tree (for woody PFTs). lue is the light-use efficiency of photosynthesis (mol CO_2 mol $photon^{-1}$), which is formulated to conform to the data in Osmond et al. (1980) as follows:

$$lue = LUE \times \frac{52 - tmp_{air}}{3.5 + 0.75(52 - tmp_{air})} \times \frac{co2_{cell}}{90 + 0.6 \times co2_{cell}} \quad \text{(for } C_3 \text{ PFTs)}, \tag{F2}$$

$$lue = LUE \quad \text{(for } C_4 \text{ PFTs)}, \tag{F3}$$

where LUE is the potential maximum value. $co2_{cell}$ is the intercellular CO_2 concentration (in μ mol mol^{-1}). The single-leaf photosynthetic rate, p_{sat}, under light saturation (in μ mol CO_2 m^{-2} s^{-1}), is calculated by multiplying its potential maximum of photosynthetic rate ($PMAX$) by the coefficients of temperature, CO_2 level, and soil water effects (ce_{tmp}, ce_{co2}, and ce_{water}, respectively).

$$p_{sat} = PMAX \times ce_{tmp} \times ce_{co2} \times ce_{water}, \tag{F4}$$

ce_{tmp}, the temperature-dependent function of p_{sat}, is a bell-shaped curve that reaches the maximum (1.0) at the optimum temperature and tapers off in warmer or cooler temperatures (Raich et al. 1991):

$$ce_{tmp} = \frac{(tmp_{air} - T_{max})(tmp_{air} - T_{min})}{(tmp_{air} - T_{max})(tmp_{air} - T_{min}) + (tmp_{air} - t_{opt})^2}, \tag{F5}$$

where tmp_{max}, T_{min}, t_{opt} (℃) and are the PFT-specific maximum, minimum, and optimum temperature for photosynthesis, respectively. t_{opt} increases with the intercellular CO_2 concentration because of photorespiration:

$$t_{opt} = T_{opt0} + 0.01\, co2_{cell}\,, \tag{F6}$$

where is the minimum value of at a very low $co2_{cell}$. For grass PFTs, topt is assumed to be a 20-year running mean of air temperature in the growth phase (maximum range $10℃ - 30℃$ for temperate-herbaceous and $10℃ - 30℃$ for tropical-herbaceous), because grass PFTs includes a varieties of species adapted to a wide range of climatic zones. The $ce2_{co2}$, the CO_2-dependent function of p_{sat}, is expressed by a Michaelis-type function:

$$ce_{co2} = 0.30 + 0.70 \times \frac{co2_{cell} - co2_{cmp}}{KM + co2_{cell}} \quad (\text{for } C_3 \text{ PFTs})\,, \tag{F7}$$

$$ce_{co2} = 0.50 + 0.50 \times \frac{co2_{cell} - co2_{cmp}}{KM + co2_{cell}} \quad (\text{for } C_4 \text{ PFTs})\,, \tag{F8}$$

where KM is the coefficient of CO_2 concentration sensitivity; $co2_{cmp}$ is the CO_2 compensation point, which is adjusted by temperature for C_3 species (Brooks and Farquhar 1985).

$$ce2_{cmp} = CO2_{cmp}[1 + 0.0451(tmp_{air} - 20) + 0.000347(tmp_{air} - 20)] \text{ (for } C_3 \text{ PFTs)}\,, \tag{F9}$$

$$ce2_{cmp} = CO2_{cmp} \quad (\text{for } C_4 \text{ PFTs})\,, \tag{F10}$$

where $CO2_{cmp}$ is the control value of $ce2_{cmp}$ at 20 ℃; ce_{water}, the water availability effect coefficient of p_{sat}, is calculated as follows:

$$ce_{water} = \sqrt{stat_{water}}\,. \tag{F11}$$

The mean daytime crown stomatal conductance of H_2O gs_{ave} (mol H_2O m^{-2} s^{-1}) is obtained as follows:

$$gs_{ave} = GS_{b1} + \frac{GS_{b2} \times p_{ave}}{(co2_{atm} - co2_{cmp})(1 + vpd/GS_{b3})}, \quad \text{(F12)}$$

where vpd is the vapor pressure deficit between saturated and actual vapor pressures. GS_{b1}, GS_{b2}, and GS_{b3} are PFT-specific parameters; gs_{ave}affects the intercellular CO_2 concentration ($co2_{cell}$ in μ mol mol^{-1}) following Leuning (1995):

$$co2_{cell} = co2_{atm} - \frac{p_{ave}}{gs_{ave}/1.56}, \quad \text{(F13)}$$

where 1.56 is a factor to convert gs into CO_2 conductance. Using Eq (F1) through (F13), we calculated p_{ave}, lue, and gs_{ave} of each PFT every simulation day.

Bibliography

Achard F, Eva HD, Stibig H-J, Mayaux P, Gallego J, Richards T, Malingreau J-P (2002) Determination of Deforestation Rates of the World's Humid Tropical Forests. Science 297:999–1002.

Ahrends A, Burgess ND, Milledge SAH, Bulling MT, Fisher B, Smart JCR, Clarke GP, Mhoro BE, Lewis SL (2010) Predictable waves of sequential forest degradation and biodiversity loss spreading from an African city. Proc. Natl Acad. Sci. USA 107:14556–14561.

Allen CD, Macalady AK, Chenchouni H, Bachelet D and others (2010) A global overview of drought and heat-induced tree mortality reveals emerging climate change risks for forests. For Ecol Manag 259: 660–684.

Anyamba A, Justice CO, Tucker CJ, Mahoney R (2003) Seasonal to interannual variability of vegetation and fires at SAFARI 2000 sites inferred from advanced very high resolution radiometer time series data. J Geophys Res 108:8507.

Anyamba A, Tucker C (2005) Analysis of Sahelian vegetation dynamics using NOAA-AVHRR NDVI data from 1981–2003. J Arid Environ 63: 596–614.

Archibald S, Roy DP, van Wilgen BW, Scholes RJ (2009) What limits fire? An examination of drivers of burnt area in Southern Africa. Glob Change Biol 15: 613–630.

Barbier EB (2001) The Economics of Tropical Deforestation and Land Use: An Introduction to the Special Issue. Land Econ 77 (2): 155-171.

Black E, Slingo J, Sperber KR (2003) An Observational Study of the Relationship between Excessively Strong Short Rains in Coastal East Africa and Indian Ocean SST. Mon Wea Rev 31:74-94.

Bond TC, Streets DG, Yarber KF, Nelson SM, Woo JH, Klimont Z (2004) A technology-based global inventory of black and organic carbon emissions from combustion. J Geophys Res 109: D14203, doi: 10.1029/2003JD003697.

Bond WJ, Midgley GF, Woodward FI (2003) The importance of low atmospheric CO2 and fire in promoting the spread of grasslands and savannas. Glob Change Biol 9: 973–982.

Bond WJ, Keeley JE (2005b) Fire as a global 'herbivore': the ecology and evolution of flammable ecosystems. Trend Ecol Evol 20: 387–393.

Bond WJ, Woodward FI, Midgley GF (2005a) The global distribution of ecosystems in a world without fire. New Phyt 165: 525–537.

Bond TC, Zarzycki C, Flanner MG, Koch DM (2011) Quantifying immediate radiative forcing by black carbon and organic matter with the Specific Forcing Pulse. Atmos Chem Phys 11:1505–1525.

Bowman DM, Balch JK, Artaxo P, Bond WJ, Carlson JM, Cochrane MA, D'Antonio CM, Defries RS, Doyle JC, Harrison SP, Johnston FH, Keeley JE, Krawchuk MA, Kull CA, Marston JB, Moritz MA, Prentice IC, Roos CI, Scott AC, Swetnam TW, van der Werf GR, Pyne SJ (2009) *Fire in the Earth system.* Science 324:481–4.

Brooks A, Farquhar GD (1985) Effect of temperature on the CO_2/O_2 specificity of ribulose 1, 5-bisphosphate carboxylase/oxygenase and the rate of respiration in the light Estimates from gas-exchange measurements on spinach. Planta 165:397–406.

Cabral AIR, Vasconcelos MJ, Oom D, Sardinha R (2010) Spatial dynamics and quantification of deforestation in the central-plateau woodlands of Angola (1990–2009). Appl Geogr 31: 1185-1193.

Cooke WF, Koffi B, Gregoire JM (1996) Seasonality of vegetation fires in Africa from remote sensing data and application to a global chemistry model. Geophys Res Lett 101: 21051–21065.

Chung CE, Ramanathan V (2006) Weakening of North Indian SST Gradients and the

Monsoon Rainfall in India and the Sahel. J Clim 19:2036-2045.

DeFries R, Hansen M, Townshend JRG, Janetos AC, Loveland TR (2000) A new global 1-km data set of percent tree cover derived from remote sensing. Glob Change Biol 6: 247–254.

Drake BG, Gonzàlez-Meler MA, Long SP (1997) More efficient plants: a consequence of rising atmospheric CO_2? Annu Rev Plant Phys 48: 609–639.

Dunne T, Leopold LB (1978) Water use by vegetation. Water in Environmental Planning. pp. 126–159. W. H. Freeman, San Francisco, Calif.

Dwyer E, Pinnock S, Grègoire JM, Pereira JMC (2000) Global spatial and temporal distribution of vegetation fire as determined from satellite observations. Int J Remote Sens 21: 1289–1302.

Emori S, Hasegawa A, Suzuki T, Dairaku K (2005) Validation, parameterization dependence, and future projection of daily precipitation simulated with a high-resolution atmospheric GCM. Geophys Res Lett 32:L06708.

Ehleringer JR, Cerling TE, Helliker BR (1997) C_4 photosynthesis, atmospheric CO_2 and climate. Oecologia 112: 285–299.

FAO (1993) Forest Resources Assessment 1990: Tropical Countries. FAO Forestry Paper No. 112. Rome.

FAO (2005) Forest Harvesting Case Study No. 22. Pit-sawn Timber Production in Natural Forests of Uganda by G.G.O Adokonyero. FAO, Rome.

Giglio L, Randerson J, van der Werf G, Kasibhatla P, Collatz G, Morton D, DeFries R (2010) Assessing variability and long-term trends in burned area by merging multiple satellite fire products. Biogeosciences 7: 1171–1186.

Gonzalez P (2001) Desertification and a shift of forest species in the West African Sahel. Clim Res 17: 217–228.

Hall J, Burgess ND, Lovett J, Mbilinyi B, Gereau RE (2009) Conservation implications of deforestation across an elevational gradient in the Eastern Arc Mountains, Tanzania. Biol Conserv 142:2510-2521.

Hao WM, Liu M-H (1994) Spatial and temporal distribution of tropical biomass burning. Global Biogeochem Cycles 8:495-503.

Hickler T, Eklundh L, Seaquist J, Smith B and others (2005) Precipitation controls Sahel greening trend. Geophys Res Lett 32: L21415, doi: 10.1029/2005GL024370.

Higgins SI, Bond WJ, Trollope WSW (2000) Fire, resprouting and variability: a recipe for grass-tree coexistence in savanna. J Ecol 88: 213–229.

Higgins SI, Bond WJ, February EC, Bronn A, Euston-Brown DI, Enslin B, Govender N, Rademan L, O'Regan S, Potgieter AL, Scheiter S, Sowry R, Trollope L, Trollope WS (2007) Effects of four decades of fire manipulation on woody vegetation structure in savanna. Ecology 88:1119–1125.

Higgins SI, Scheiter S (2012) Atmospheric CO_2 forces abrupt vegetation shifts locally, but not globally. Nature 488: 209-212.

Hoffmann WA, Schroeder W, Jackson RB (2002) Positive feedbacks of fire, climate, and vegetation and the conversion of tropical savanna. Geophys Res Lett 29:2052.

Holdridge LR (1947) Determination of world plant formations from simple climatic data. Science 105(2727): 367–368.

Hulme M, Doherty R, Ngara T, New M, Lister D (2001) African climate change: 1900–2100. Clim Res 17:145-168.

Hui D, Jackson RB (2006) Geographical and inter-annual variability in biomass partitioning in grassland ecosystems: a synthesis of field data. New Phyt 169: 85–93.

IPCC (2007) Climate Change 2007: The Physical Science Basis. Contribution of Working Group I to the Fourth Assessment Report of the Intergovernmental Panel on Climate Change. Cambridge University Press, Cambridge, UK and New York, NY,

USA.

Ishii S, Sato H, Yamazaki T (2013) Geographical variability of relations among black carbon from wildfires, climate, and vegetation in Africa. Clim Res 57:221-231.

Jennifer R, Olson BA, Baum DR, Cahoon JH, Crawford (1999) Frequency and distribution of forest, savanna, and crop fires over tropical regions during PEM-Tropics A. J Geophys Res 104:5865-5876.

Joos F, Prentice IC, Sitch S, Meyer R, Hooss G, Plattner G, Gerber S, Hasselmann K (2001) Global warming feedbacks on terrestrial carbon uptake under the Intergovernmental panel on climate change (IPCC) emission scenarios. Global Biogeochem Cycles 15:891–907.

Kalnay E, Kanamitsu M, Cistler R, Collins W, Deaven D, Gandin L, Iredell M, Saha S, White G, Woollen J, Zhu Y, Chelliah M, Ebisuzaki W, Higgins W, Janowiak J, Mo KC, Ropelewski C, Wang J, Leetma A, Reynolds R, Jenne R, Joseph D (1996) The NCEP/NCAR 40-year reanalysis project, Bull. Am Meteorol Soc 77(3):437–471.

Kawase H, Takemura T, Nozawa T (2011) Impact of carbonaceous aerosols on precipitation in tropical Africa during the austral summer in the twentieth century. Geophys Res Lett 116: D18116, doi: 10.1029/2011JD015933

Keeley JE, Fotheringham CJ, Morais M (1999) Reexamining fire suppression impacts on brushland fire regimes. Science 284: 1829−1832.

Kindermann GE, McAllum I, Fritz S, Obersteiner M (2008) A global forest growing stock, biomass and carbon map based on FAO statistics, Silva Fennica 42(3):387–396.

Koffi B, Grégoire JM, Mahé G, Lacaux JP (1995) Remote sensing of bush fire dynamics in Central Africa from 1984 to 1988: analysis in relation to regional vegetation and pluviometric patterns. Atmos Res 39:179-200.

Kofron CP, Chapman A (1995) Deforestation and bird species composition in Liberia, West Africa. Trop Zool 8:239-256.

Kottek M, Grieser J, Beck C, Rudolf B, Rubel F (2006) World Map of the Köppen-Geiger climate classification updated. Meteorol Z 15:259-263.

K-1 model developers (2004) K-1 coupled GCM (MIROC) description. (Hasumi H and Emori S, eds.) K-1 Technical Report, 1, 34pp. (available from the Center for Climate System Research, University of Tokyo)

Larcher W (1995) Ecophysiology and stress physiology of functional groups. In: Physical Plant Ecology. Springer, Berlin, p. 506.

Leuning R (1995) A critical appraisal of a combined stomatal-photosynthesis model for C_3 plants. Plant Cell Environ 18:339–355.

Lehsten V, Tansey K, Balzter H, Thonicke K and others (2009) Estimating carbon emissions from African wildfires. Biogeosciences 6: 349–360.

Lu J, Delworth TL (2005) Oceanic forcing of late 20th century Sahel drought. Geophys Res Lett 32:L22706.

Lwanga JS (2003) Localized tree mortality following the drought of 1999 at Ngogo, Kibale National Park, Uganda. Afr J Ecol 41: 194–196.

MacGregor SD, O'Connor TG (2002) Patch dieback of *Colophospermum mopane* in a dysfunctional semi-arid African savanna. Austral Ecol 27: 385–395.

Mitchell TD, Jones PD (2005) An improved method of constructing a database of monthly climate observations and associated high-resolution grids. Int J Climatol 25: 693–712.

Osmond CB, Björkman O, Anderson DJ (1980) Photosynthesis Physiological Processes in Plant Ecology. Springer-Verlag, Berlin. pp. 291–377.

Patra PK, Ishizawa M, Maksyutov S, Nakazawa T, Inoue G (2005) Role of biomass burning and climate anomalies for land-atmosphere carbon fluxes based on inverse modeling of atmospheric CO_2. Global Biogeochem Cycles 19:GB3005.

Poore D, Burgess P, Palmer J, Rietbergen S, Synnott T (1989) No timber without trees: sustainability in the tropical forest. London: Eartbscan 252 pp.

Raich JW, Rastetter EB, Melillo JM, Kicklighter DW, Steudler PA, Peterson BJ, Grace AL, Moore III B, Vörösmarty CJ (1991) Potential net primary productivity in South America: application of a global model. Ecol Appl 1:399–429.

Ramanathan V, Carmichael G (2008) Global and regional climate changes due to black carbon. Nat Geosci 1: 221−227.

Riaño D, Moreno Ruiz JA, Barón Martínez J, Ustin SL (2007) Burned area forecasting using past burned area records and Southern Oscillation Index for tropical Africa (1981–1999). Remote Sens Environ 107:571-581.

Russell-Smith J, Yates CP, Whitehead PJ, Smith R and others (2007) Bushfires 'down under': patterns and implications of contemporary Australian landscape burning. Int J Wildland Fire 16: 361−377.

Sankaran M, Ratnam J, Hanan NP (2004) Tree-grass coexistence in savannas revisited—insights from an examination of assumptions and mechanisms invoked in existing models. Ecol Lett 7: 480−490.

Sankaran M, Hanan NP, Scholes RJ, Ratnam J, Augustine DJ, Cade BS, Gignoux J, Higgins SI, Le Roux X, Ludwig F, Ardo J, Banyikwa F, Bronn A, Bucini G, Caylor KK, Coughenour MB, Diouf A, Ekaya W, Feral CJ, February EC, Frost PGH, Hiernaux P, Hrabar H, Metzger KL, Prins HHT, Ringrose S, Sea W, Tews J, Worden J, Zambatis N (2005) Determinants of woody cover in African savannas. Nature 438:846–849.

Sarmiento G (1984) The Ecology of Neotropical Savannas. Harvard University Press, Cambridge, MA.

Sato H, Itoh A, Kohyama T (2007) SEIB–DGVM: A new Dynamic Global Vegetation Model using a spatially explicit individual-based approach. Ecological Modelling 200:279-307.

Sato H, Ise T (2012) Effect of plant dynamic processes on African vegetation responses

to climate change: Analysis using the spatially explicit individual-based dynamic global vegetation model (SEIB-DGVM). J Geophys Res 117:G03017.

Scheiter S, Higgins SI (2009) Impacts of climate change on the vegetation of Africa: an adaptive dynamic vegetation modelling approach. Global Change Biol 15:2224-2246.

Schmidt MWI, Skjemstad JO, Czimczik CI, Glaser B, Prentice KM, Gelinas Y, Kuhlbusch TK (2001) Comparative analysis of black carbon in soils. Global Biogeochem Cycles 15: 163–167.

Scholes RJ (2003) Convex relationships in ecosystems containing mixtures of trees and grass. Environ Resour Econ 26: 559–574.

Solomon S., et al. (2007) Climate Change 2007: The Physical Science Basis. Contribution of Working Group I to the Fourth Assessment Report of the Intergovernmental Panel on Climate Change, Cambridge Univ. Press, Cambridge, U. K.

Taylor KE (2001) Summarizing multiple aspects of model performance in a single diagram. J Geophys Res 33:L06703.

Thonicke K, Venevsky S, Sitch S, Cramer W (2001) The role of fire disturbance for global vegetation dynamics: coupling fire into a Dynamic Global Vegetation Model. Global Ecol Biogeogr 10:661-677.

Turner DP, WD Ritts, M Gregory (2006) BigFoot NPP surfaces for North and South American sites, 2002–2004. Oak Ridge National Laboratory Distributed Active Archive Center, Oak Ridge, TN. http://daac.ornl.gov/ cgi- bin/dsviewer.pl?ds_id=750, doi: 10.3334/ORNLDAAC/ 750

Zhang R, Delworth TL (2006) Impact of Atlantic multidecadal oscillations on India/Sahel rainfall and Atlantic hurricanes. Geophys Res Lett 33:L17712.

van der Ent RJ, Savenije HHG, Schaefli B, Steele-Dunne SC (2010) Origin and fate of atmospheric moisture over continents. Water Resour Res 46: W09525, doi: 10. 1029/ 2010WR 009127

van der Werf GR, Randerson JT, Giglio L, Collatz GJ and others (2010) Global fire emissions and the contribution of deforestation, savanna, forest, agricultural, and peat fires (1997–2009). Atmos Chem Phys 10: 11707–11735

Watson N. (Edit.) 1991. African rainforest threatened. EDF Letter. 22(2):8 New York: Environmental Defense Fund.

Whittaker RH (1974) Communities and Ecosystems, 6th printing, 161 pp., Macmillan, London.